UNIVERSITY OF SÃO PAULO
SÃO CARLOS SCHOOL OF ENGINEERING

Victor Tamassia Noppeney

Transparency-inspired tools for wearable robots

São Carlos, SP, Brazil

2021

Victor Tamassia Noppeney

Transparency-inspired tools for wearable robots

Dissertation presented to the São Carlos School of Engineering of the University of São Paulo, for obtaining the title of Master of Science - Graduate Program in Mechanical Engineering.

Area of concentration: Dynamics and Mechatronics

Advisor: Thiago Boaventura Cunha

This research is supported by the grant # 2019/10773-3, São Paulo Research Foundation (FAPESP). The opinions, assumptions, conclusions, or recommendations expressed in this material are those of the author and do not necessarily reflect the views of FAPESP.

CORRECTED VERSION

São Carlos, SP, Brazil

2021

N821t

Noppeney, Victor Tamassia
Transparency-inspired tools for wearable robots / Victor Tamassia Noppeney; advisor Thiago Boaventura Cunha. São Carlos, SP, Brazil, 2021.
185 p. : il. ; 30 cm.

Dissertation (Master's) - Graduate Program in Mechanical Engineering and Area of Concentration in Dynamics and Mechatronics – São Carlos School of Engineering, University of São Paulo, 2021.

1. Transparency control. 2. Kinematic compatibility. 3. Motion prediction. 4. Robotics. 5. Exoskeleton robots. I. Title.

FOLHA DE JULGAMENTO

Candidato: Engenheiro **VICTOR TAMASSIA NOPPENEY.**

Título da dissertação: "Ferramentas para controle de transparência de robôs vestíveis".

Data da defesa: 01/07/2021.

Comissão Julgadora	**Resultado**
Prof. Dr. **Thiago Boaventura Cunha** **(Orientador)** (Escola de Engenharia de São Carlos – EESC/USP)	**Aprovado**
Prof. Dr. **Roberto Santos Inoue** (Universidade Federal de São Carlos/UFSCar)	**Aprovado**
Prof. Associado **Arturo Forner-Cordero** (Escola Politécnica/EP-USP)	**Aprovado**

Coordenador do Programa de Pós-Graduação em Engenharia Mecânica:
Prof. Associado **Adriano Almeida Gonçalves Siqueira**

Presidente da Comissão de Pós-Graduação:
Prof. Titular **Murilo Araujo Romero**

This work is dedicated to my father Victor and my mom Valeria,
to whom I will be grateful forever.

ACKNOWLEDGEMENTS

I would like to express my special thanks to:

My advisor and friend, Professor Thiago Boaventura, for the constant support regarding the research and also my personal development.

My colleague and fellow researcher, Bruno Pisi Garcia, for sharing the knowlege on gait motion prediction algorithms from his Scientific Initiation work, which were of great value for this dissertation.

Professors Adriano Siqueira and Glauco Caurin. Apart from teaching me several concepts during my bachelor and graduation courses, they gave invaluable contributions to this work during my Qualifying exam.

Professors Arturo Forner-Cordero and Roberto Santos Inoue, for integrating the judging commission of my Master's exam and sharing relevant knowledge about this research topic.

Jair Diego, technician of the EESC-USP Dynamics Laboratory, who helped with the manufacturing of several items that compose some research prototypes.

The São Paulo Research Foundation (FAPESP), for believing in this research and providing financial aid for it.

The University of São Paulo (USP) and the São Carlos School of Engineering (EESC), for providing me with a high level of education during my Mechatronics Engineering bachelor and the Mechanical Engineering graduation.

All shops and businesses that have accepted to serve me and helped with the bureaucratic aspects regarding purchases of equipment for the research.

"A person can never be broken.
Our built environment, our technologies are broken and disabled.
We the people need not accept our limitations,
but can transcend disability through technological innovation."
Hugh Herr

ABSTRACT

NOPPENEY, V. T. **Transparency-inspired tools for wearable robots**. 2021. 185p. Dissertation (Master's) - São Carlos School of Engineering, University of São Paulo, São Carlos, SP, Brazil, 2021.

Exoskeleton robots are characterized by their anthropomorphism and operation in intrinsic contact with a human being, i.e., the user. Most of their applications include expanding the physical limits of human beings, whether in the rehabilitation of people with locomotion limitations, in the reduction of metabolic rate during the execution of a given task, in the carrying of loads with high mass, or in the amplification of the user's force. However, such applications are only possible if the exoskeleton moves in harmony and synchrony with its user, so that the user does not feel discomfort nor need to expend additional effort while using the wearable robot. This concept is called *transparency*, and is achievable through the combination of sensing, estimation, control, and actuation systems. This work will study the proposals that seek such transparency in the State of the Art and propose new ways to pursue this goal, focusing mainly on kinematically compatible mechanical design and human motion prediction for anticipatory behavior. Regarding mechanical design, different concepts focused on biomimetics and ergonomics are discussed and put into practice through the design of ankle and knee joints. After that, a universal human motion prediction algorithm, based on artificial neural networks, is proposed and evaluated.

Keywords: Transparency control. Kinematic compatibility. Motion prediction. Robotics. Exoskeleton robots.

RESUMO

NOPPENEY, V. T. **Ferramentas inspiradas em transparência para robôs vestíveis**. 2021. 185p. Dissertação (Mestrado) - Escola de Engenharia de São Carlos, Universidade de São Paulo, São Carlos, SP, Brazil, 2021.

Robôs exoesqueleto são caracterizados por seu antropomorfismo e operação em contato intrínseco com um ser humano, ou seja, seu usuário. Grande parte de suas aplicações inclui expandir os limites físicos de seres humanos, seja na reabilitação de pessoas com problemas de locomoção, na redução da taxa metabólica durante execução de determinada tarefa, no carregamento de cargas com massas elevadas ou na amplificação de força do usuário. Entretanto, tais aplicações são possíveis apenas se o exoesqueleto mover-se com harmonia e sincronia relativamente a seu usuário, para que este não sinta desconforto ou precise despender esforços adicionais enquanto utiliza o robô vestível. A este conceito dá-se o nome de *transparência*, sendo atingível a partir da combinação de sistemas de sensoriamento, estimação, controle e atuação. O presente trabalho irá estudar as propostas que buscam tal transparência no Estado da Arte e propor novas formas de buscar este objetivo, focando principalmente em projeto mecânico cinematicamente compatível e predição de movimento humano para comportamento antecipatório. Tratando do projeto mecânico, diferentes conceitos focados em biomimética e ergonomia são discutidos e colocados em prática através do projeto de juntas de tornozelo e joelho. Em seguida, propõe-se e avalia-se um algoritmo universal de previsão de movimento humano, baseado em redes neurais artificiais.

Palavras-chave: Controle de transparência. Compatibilidade cinemática. Predição de movimentos. Robótica. Robôs exoesqueleto.

LIST OF FIGURES

LIST OF TABLES

LIST OF ABBREVIATIONS AND ACRONYMS

1D	One-dimensional
2D	Two-dimensional
3D	Three-dimensional
ABS	Acrylonitrile Butadiene Styrene
ACCAD	Advanced Computing Center for the Arts and Design
Adam	Adaptive Moment Estimation
AI	Artificial Intelligence
ALEX	Active Leg Exoskeleton
AMASS	Archive of Motion Capture as Surface Shapes
BLEEX	Berkeley Lower Extremity Exoskeleton
BML	BioMotionLab
BoS	Base of Support
CAD	Computer Aided Design
CMU	Carnegie Mellon University
CNN	Convolutional Neural Network
CoM	Center of Mass
CoP	Center of Pressure
CPU	Central Processing Unit
CUDA	Compute Unified Device Architecture
DFaust	Dynamic Fine Alignment Using Scan Texture
DIP	Deep Inertial Poser
DMPL	Dynamic SMPL
DoF	Degree of Freedom
Dota	Defense of the Ancients

ECN	Ensemble of Candidate Neighbors
ELU	Exponential Linear Unit
EMG	Electromyography
GB	Gigabyte
GELU	Gaussian Error Linear Unit
GPU	Graphical Processing Unit
GRU	Gated Recurrent Unit
GSN	Gait Sensitivity Norm
HAL	Hybrid Assistive Leg
HuMAn	Human Motion Anticipation
Hz	Hertz
ICR	Instantaneous Center of Rotation
IMU	Inertial Measurement Unit
km	Kilometer
KIT	Karlsruhe Institute of Technology
KNN	K-Nearest Neighbors
kPa	Kilopascal
LED	Light-Emitting Diode
LIPM	Linear Inverted Pendulum Model
LoS	Limit of Stability
LSTM	Long Short-Term Memory
mm	Millimeter
mmHg	Millimeter of Mercury
MPI	Max Plack Institute
ms	Millisecond
NNGI	Nearest Neighbor Gait Index

PCA	Principal Components Analysis
POF	Polymer Optical Fiber
rad	Radians
RAM	Random Access Memory
ReLU	Rectified Linear Unit
ResNet	Residual Network
RLC	Reference Limit Cycle
RMS	Root Mean Squared
RNN	Recurrent Neural Network
s	Second
s-EMG	Surface Electromyography
SELU	Scaled Exponential Linear Unit
seq2seq	Sequence-to-Sequence
SFU	Simon Fraser University
SGD	Stochastic Gradient Descent
SMPL	Skinned Multi-Person Linear Model
SMPL+H	SMPL with articulated Hands
SMPL-X	SMPL eXpressive
SPL	Structured Prediction Layer
SSM	Synchronized Scans and Markers
STAR	Sparse Trained Articulated Human Body Regressor
SWA	Stochastic Weight Averaging
TCD	TotalCapture Dataset
TFRecords	TensorFlow Records
TtC	Time to Contact
TUPLEE	Technische Universität Berlin Powered Lower Extremity Exoskeleton

VRAM	Video Random Access Memory
VTC	Virtual Time to Collision
WPAL	Wearable Power Assist Leg
XCoM	Extrapolated Center of Mass

LIST OF SYMBOLS

$\%$	Percent
m_r	Robot inertia
f_i	Interaction force
k_a	Coupling stiffness
f_r	Force exerted by the robot
$\ddot{x}_h$	Human limb acceleration
$^\circ$	Degree
x	Biped state
p	Capture Point
m	Mass
v	Velocity
g	Acceleration of gravity
h	Height
d	Step length
v_d	Desired velocity
ω_0	Natural oscillating frequency
l	Effective pendulum length
u	Position of the center of pressure
b	Dynamic stability metric
T_n	Step time
s	Step length
ξ_n	Extrapolated center of mass position
u_{xn}	Forward center of pressure position (step location)
b_x	Forward offset

u_{zn}	Lateral center of pressure position (step location)
b_z	Lateral offset
w_c	Desired stride width
k_1	Lateral proportional gain
x_c	"Middle of the road" setpoint
$\tau(x)$	*Tau* function
v	Center of mass velocity
a	Center of mass acceleration
p_{max}	Location of the toe or heel markers (stability boundaries)
p	Center of mass position
D_{min}	Minimum distance between the vertical projection of the center of mass the and edges of the base of support
D_{tCv}	Distance to the edge of the base of support in the direction of the velocity of the center of mass
D_{tCa}	Distance to the edge of the base of support considering instantaneous acceleration of the center of mass
T_{tCv}	Time to contact between center of mass and base of support considering constant velocity;
T_{tCa}	Time to contact between center of mass and base of support taking acceleration into account
A_{BoS}	Total surface area of the base of support
t	Time
m	Number of states for the ECN
$\hat{q}(k)$	Best-match ECN state
$q(k)$	Current biped state
ϕ	Golden Ratio
H_T	Total body height
L_L	Lower leg length

R_L	Leg radius
H_F	Foot height (from sole to ankle)
V_R	Varus rotation
I_R	Internal rotation
Z_{DIS}	Anterior-posterior translation
Y_{DIS}	Distal-proximal translation
F	Flexion angle
$L_1 \dots L_4$	Four-bar linkage lengths
ψ_T	Four-bar tibial tilt angle
ψ_F	Four-bar femoral tilt angle
$x_0 \dots x_4$	Horizontal coordinates of the four-bar linkage
$y_0 \dots y_4$	Vertical coordinates of the four-bar linkage
A, B, C, D	Four-bar linkage lengths
θ_F	Knee flexion angle
$\theta_B, \theta_C, \theta_D$	Four-bar linkage angles
π	Mathematical constant pi
m_1, m_2	Line angular coefficients
θ_{std}	Standardized joint angle
θ_{input}	Input joint angle
μ	Mean for a joint angle computed with training data
σ	Standard deviation for a joint angle computed with training data
h_t	Context of past pose observations
$\hat{x}_t^{(k)}$	Predicted joint pose
len_{window}	Total length of the data window
$len_{sequence}$	Target sequence length
hor_{max}	Maximum prediction horizon

dt	Sampling time between two consecutive inputs
p_i	Probability of choosing individual i
β	Roulette Wheel Selection bias factor
c_i	Cost of individual i
$\bar{c}$	Average cost
n	Total number of individuals
r	Random number
x_1, x_2	Parent individuals
y_1, y_2	Offspring individuals
α	Crossover weighting array
x_i'	Mutated value for parameter i of individual x
x_i	Original value for parameter i of individual x
δ	Random value sampled from the normal distribution $N(0, \sigma^2)$
σ	Mutation step size
μ	Probability threshold for a mutation to occur
$\sigma(x)$	Sigmoid function
$\varsigma(x)$	Softplus function
μ	Mean
σ	Standard deviation
n	Number of data points

CONTENTS

1 INTRODUCTION

Exoskeletons are robots with morphology similar to the human body as a whole, or part of it, designed to operate in close contact with humans for a variety of activities, generating supplementary forces to empower and overcome human physical limits (ALAMI et al., 2006). These activities include metabolic rate reduction (AGUIRRE-OLLINGER et al., 2012), transport of high mass loads (KAZEROONI et al., 2005) and user force amplification. Such objectives, which markedly alter the natural operation of the human body prior to the coupling between it and the exoskeleton, are achieved with good synergy with the user only if the robot is not interfering in the movements and tasks that the user wishes to perform (ZANOTTO et al., 2013). In front of what was explained above, the concept of *transparency* emerges in exoskeletons, seeking to explain how imperceptible the robot is to its user. In a scenario of perfect transparency, the human could perform any movement without feeling any resistance coming from the exoskeleton, while having the benefits of increased strength, reduced muscle fatigue, among others. Exoskeletons are also valuable tools for rehabilitation (NOGUEIRA et al., 2014), however this type of application generally involves nontransparent behavior, with the robot imposing a given trajectory for the patient to train. As the therapy evolves, it its then possible to reduce the assistance levels, until the exoskeleton behaves transparently. Transparency in rehabilitation can also be used in specific joints, in which the patient has enough muscular mobility and independence.

1.1 Motivation

Exoskeletons will soon have an important role in people's daily lives (FERRIS; SAWICKI; DALEY, 2007), being used as assistive devices for patients (BLAYA; HERR, 2004; SAWICKI; DOMINGO; FERRIS, 2006) or as a support tool for healthy subjects. Military soldiers, for example, carry loads ranging from 30 % to 100 % of their own body weight (CARON et al., 2015). Carrying heavy weights is also common in recreational activities such as hiking, where participants walk for long periods in wilderness environments, ranging from simple day hikes to expeditions that last several months (BOHNE, 2005). It is then common to carry loads ranging from 20 % to 40 % of body weight, what can affect muscle activity patterns of lower limbs (SIMPSON; MUNRO; STEELE, 2011) and increase the risk of injury (MCINTOSH et al., 2007). Exoskeletons can also play a role during walking for extended periods, like the ranges of 25 km to 74 km accomplished in one day by ancient Roman legionnaires (FORNARIS; AUBERT, 1998).

The development of a package of solutions that, when integrated, provide an increase in the transparency of a wearable robot is undoubtedly an important step towards

greater use of existing technologies in robotics for the benefit of human health and work. It only makes sense to use an exoskeleton in assistive applications when it, at the very least, does not bring any additional stress to the user compared to performing the same task without any assistance. Therefore, such solutions need components such as sensors, actuators, prediction algorithms, and control systems that provide compensation for robot dynamics and sufficiently fast response times, resulting in ideally zero interaction forces.

1.2 Goals

1.2.1 Main goal

This dissertation aims at improving the level of transparency perceived by a human wearing an exoskeleton, through the proposal of solutions focused on both mechanical design and prediction algorithms. Focus is given to the lower limbs (hip, knee, and ankle joints).

1.2.2 Detailed goals

- *To propose ergonomic principles for mechanical exoskeleton design.*
  Every exoskeleton possesses a direct correspondence between its joints (or sets of joints) and the human anatomical joints. Thus, its design must pursue, besides safety, comfort, and ergonomics. The proposed design principles seek to minimize motor incompatibilities, be simple and easy to use, and maximize force transmission between the robot and its wearer. This objective encompasses the design and assessment of two lower-limb external joints, comprising ankle and knee.

- *To develop a human motion predictor.*
  This system is responsible for processing the sequence of poses (joint angles) from the human user and predicting these motions for future time intervals. Such predicted poses can be used as an anticipatory input for different control algorithms, enabling better synchronization between human and robot motions.

1.3 Dissertation outline

This dissertation starts with an overview of related works in Chapter 2. Then, Chapter 3 presents important mechanical design principles for exoskeleton robots focused at transparent operation. Next, in Chapter 4, a motion prediction algorithm is developed in detail, enabling to estimate future poses to be performed by the exoskeleton user. Last, Chapter 5 draws some conclusions about the present work, and lists some envisioned future research.

2 STATE OF THE ART REVIEW

The following sections aim at providing a general overview of works that are related to this dissertation. Transparent assistive exoskeleton development is a rather new research subject, thus many of the references are recently published articles. In the present case, newness does not imply in scarcity of material, being not possible to give reference to every work produced. However, the most relevant and related contributions are listed in a comprehensive manner. For the sake of organization, the references are grouped together in categories.

2.1 Transparent wearable robotics

The concept of transparent wearable robots is a subset of the complete universe of exoskeletons and is represented by a diversity of approaches and solutions. This section shortly describes some of them, following an approximate chronological order. While the goal of closely following the motion patterns generated by the user is common, the means to fulfill it are multiple, as shown next.

Figure 1 – The HAL-3 exoskeleton and its user.

Source: Kawamoto and Sankai (2005)

Lee and Sankai (2002) developed the *HAL-3* exoskeleton (Figure 1) focusing on assisting people with locomotion difficulties. To attest the user's intention of movement, this exoskeleton was instrumented with surface electromyography sensors (s-EMG), which

measure the muscle activity from the associated nerve impulses. The amplitude of the measured nervous activity is approximately proportional to the force exerted by the muscle fibers. This is an approach that allows some anticipation in terms of being able to perceive the intention of the movement just before it actually occurs. This system enabled to minimize the torque requirements for moving the knee joint.

Pratt, Krupp, et al. (2004) created the *RoboKnee*, a knee joint driven orthosis, which provides increased strength and resistance, but has considerable impedance in fast movements, preventing the user from running. This work used a series elastic actuator, which consists in connecting the actuator and the load to be moved with an elastic element (spring). This way, the robot impedance perceived by the user is physically reduced. It is an actuation proposal focused on this type of human-robot interaction, aiming at controlling forces without a great concern with position (which rigid actuators provide, in contrast). Due to the presence of elastic elements, the force in the actuator can be easily measured from the deformation of this element with a position transducer.

Figure 2 – Berkeley Lower Extremity Exoskeleton (*BLEEX*) and its user, carrying a remarkably large backpack.

Source: Kazerooni et al. (2005)

Kazerooni et al. (2005) worked on controlling the *BLEEX* (Berkeley Lower Extremity Exoskeleton), an exoskeleton for the lower limbs (Figure 2) whose purpose is to carry loads during the movement of its user, without interfering in its movement. This was implemented without directly measuring the interaction forces between the human and the robot, using instead a high sensitivity controller. This allows the robot to respond quickly when following the user's movements, but culminates in a controller with little robustness. Thus, the control becomes highly dependent on a very precise modeling, which

should be avoided when aiming to make an exoskeleton capable of being used by a wide range of subjects (there are differences in height, body proportion, muscle tone and agility, for example).

Still regarding the work of Kazerooni et al. (2005), only the contact between the sole of the user's foot and the robot was sensed, measuring the contact pressure on four spots. This was necessary to assess which ground contact situation the system is subject to, then select the correct dynamics for the controller. This exoskeleton also had important considerations in terms of mechanical design, making use of Clinical Gait Analysis to achieve biomimetism in the sagittal plane (CHU; KAZEROONI; ZOSS, 2005) (see Figure 3).

Figure 3 – Model of 1st generation *BLEEX*, with robot joints corresponding to human joints in the sagittal plane.

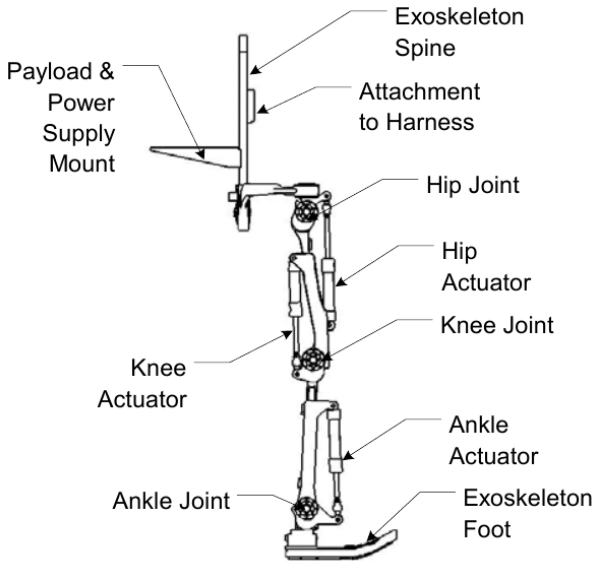

Source: Chu, Kazerooni, and Zoss (2005)

Vallery, Duschau-Wicke, and Riener (2009) sought to raise the levels of transparency of haptic devices or exoskeletons. In their work, it was observed that the more traditional approach of compensating inertial and gravitational terms has some important disadvantages:

- The reduction of inertia is limited, there are always inertial effects remaining, and this technique requires force sensors;

- The compensation of gravity is not always beneficial, because the human organism naturally uses gravitational effects to aid some movements, such as walking or moving downstairs.

Thus, they proposed to model the passive dynamics of interaction devices (haptics or exoskeletons) to approach the passive dynamics of the human organism. For this, the technique of Generalized Elasticity is used, which dispenses with modeling the human organism and does not require a device physically similar to the members in question. However, the desired movement must be known *a priori* (performance is associated with the quality of this prediction) and the application of this and other comparative approaches have failed to raise the walking cadence of test subjects.

Moreno et al. (2009) analysed the interaction of human subjects with a wearable unilateral lower-limb exoskeleton. Every such interaction is bidirectional: while the robot uses its sensors to monitor the user's intentions and act based on that, healthy users also slightly adapt their motion patterns to obtain the desired responses from the exoskeleton. The mentioned study reported that the subjects actively learned how to best interact with the exoskeleton after undergoing training sessions. As a result, the authors state that exoskeletons must preferably adapt themselves to their users in a coupled learning approach.

Aguirre-Ollinger et al. (2012) argued that an exoskeleton should be as transparent as possible to the user while producing forces to aid movement, contributing to reduce the normal metabolic rate for a given task. Such concepts are fundamental for humans to be willing to use the exoskeleton. Using a stationary model to operate the knee joint, the focus of the controller was to compensate the inertia of the set by performing positive feedback of a torque sensor installed between the robotic member and the actuator (servomotor). This makes the exoskeleton unstable if isolated (something that also occurs with the *BLEEX* of Kazerooni et al. (2005)).

In the work of Aguirre-Ollinger et al. (2012), a practical test involving the pendular movement of the leg using the knee joint showed that the compensation of inertia provided gains of amplitude in this movement. There was even a comparison with *BLEEX*, saying that it only seeks to support the additional load placed on the exoskeleton, while the inertial compensator seeks to perform liquid work on the movements initiated by the human user.

Zanotto et al. (2013) aimed at raising the level of transparency of human-robot interaction by using force sensors at the point of connection between user limbs and robot links. According to the authors, such approach allows the robot inertia to be masked from the user's perspective, which torque sensors located in the robot joints do not provide. The traditional solution makes the user have to exert additional forces to compensate the inertial forces generated by the exoskeleton structure. The new controller has indeed succeeded in reducing the interaction torques. However, the implementation depends on six-axis force sensors installed right between the user and the robot.

Walking gait has unarguable relevance concerning exoskeletons, especially lower-

limb ones, that can be used by patients during rehabilitation or by healthy subjects. Dijk, Kooij, et al. (2013) proposes exploiting the cyclic nature of walking to develop transparency controllers based on adaptive frequency oscillators and kernel-based nonlinear filters (GAMS et al., 2009; RONSSE et al., 2011). Incorporating the predictions from these systems in controller operation, it was possible to improve joint torque tracking by at least 52 % in assisted walking experiments.

Dijk and Kooij (2013) studied the effectiveness of exoskeletons in effectively reducing human energy expenditure during walking. The authors point out that simply delivering torque patterns similar to the ones observed in unsupported walking does not guarantee a reduced metabolic cost, due to the following effects:

- Humans adapt their motion patterns to supported walking (KAO; LEWIS; FERRIS, 2010);
- The human motor system has energy-efficient mechanisms such as temporal energy storage in tendons and energy transfer between joints through bi-articular muscles (WIGGIN; SAWICKI; COLLINS, 2011; ISHIKAWA et al., 2005).

As such, Dijk and Kooij (2013) applied a muscle-reflex model (GEYER; HERR, 2010) to closely represent the human body in a simulated environment, and two different controllers to model an ankle exoskeleton that assists plantarflexion. The muscle-reflex model was able to represent adaptation to the external support, and the simulated exoskeleton was able to consistently reduce energy consumption at the ankle joint.

Accoto, Sergi, et al. (2014) proposed a novel design for lower-limb exoskeletons, based on a nonanthropomorphic architecture, allowing for low reflected inertia on the user's body, high backdrivability, and tolerance to misalignment. This robot assists hip and knee flexion in the sagittal plane through a pair of custom series elastic actuators (ACCOTO; CARPINO, et al., 2013). The nonanthropomorphic design also makes the wearing procedure easy and intuitive, as it does not require precise mechanical alignment with the corresponding human body joints.

Nogueira et al. (2014) have concentrated their work on designing a position estimator for lower limb exoskeletons. The proposal is initially based on the Kalman Filter (KALMAN, 1960), an estimator of wide dissemination in the literature. However, the authors used a Markovian estimation model in combination with the Kalman filtering techniques, in addition to jointly using angular position data from all available sensors for the lower limbs, comprising the absolute trunk, thigh, leg and foot orientations and the relative hip, knee and ankle joint orientations. Such sensor fusion achieves better results than just Kalman filtering. These results show the importance of joint motor coordination, as the complete movement of the human body takes place in harmony.

Boaventura and Buchli (2016) proposed transparency control based on the disparity between the acceleration signals of the human and the coupled exoskeleton. To do so, the measurement would be performed using inertial measurement units (IMUs) rigidly connected to each of these bodies. When it comes to mathematical modeling, it is a very promising way to implement such control. The basic dynamics is represented by the following expression, based on the diagram in Figure 4.

Figure 4 – Free-body diagram of the human-robot coupling, as well as a graphical representation of the real coupling

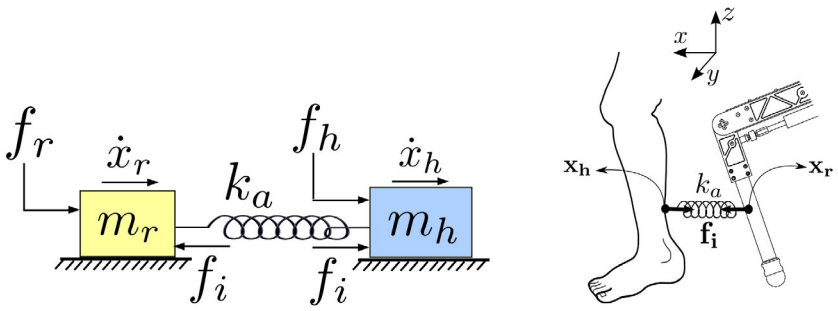

Source: Boaventura and Buchli (2016)

$$m_r \ddot{f}_i + k_a f_i = k_a(f_r - m_r \ddot{x}_h) \tag{2.1}$$

In which:

- m_r: robot inertia;
- f_i: interaction force;
- k_a: coupling stiffness;
- f_r: force exerted by the robot;
- $\ddot{x}_h$: human limb acceleration.

As the focus of the controller is to make the robot imperceptible to the user, the task is to make the interaction force f_i converge as quickly as possible to zero (BOAVENTURA; BUCHLI, 2016). To achieve this goal, mixed control techniques were used, with the combination of anticipatory control (*feedforward*) and feedback control (*feedback*). Such techniques can be summarized as follows (FRANKLIN; POWELL; EMAMI-NAEINI, 2015; OKLE, 2016):

- Model-based anticipatory control (model-based feedforward) often uses an inverse version of plant dynamics (MISTRY; BUCHLI; SCHAAL, 2010; RIGHETTI et al.,

2011), predicting the input that must be applied to obtain the desired output. It is possible to see that such a controller mitigates delays by not relying on error signals. However, any minimal deviations between the model and the actual plant or disturbances cause such controllers to diverge rapidly;

- In contrast, feedback control calculates the error between the current and the desired output, and from this calculates a control action responsible for resetting that error. In this way, it is possible to compensate some differences between the model and the actual plant and still follow the reference, but all this is done only after the appearance of a non-zero error.

Thus, the combination of *feedforward* and *feedback* techniques seeks to take advantage of the features of each controller, constituting a system with smaller delays thanks to model-based anticipation, combined with the robustness brought by feedback, whose focus is to bring errors to zero. In the specific case of Boaventura and Buchli (2016), an anticipatory controller based on inverse dynamics was used in conjunction with a feedback controller, so that the robot acceleration follows the reference given by the human acceleration, and a state estimator for the interaction force, which uses as input the accelerations of both bodies involved.

However, such a proposal comes up against two main issues:

- Inertial unit acceleration signals have noise, like any signal from sensors, and the amplitudes of the disparities need to be quite small for the controller to respond before the user feels any discomfort or lack of synchrony between him and the exoskeleton. Therefore, separating these low amplitude signals from the noise is a notable challenge;

- Using an acceleration signal as an input for transparency control implies that there is a difference between the displacement profiles of the human and the robot. In this way, the controller acts on a condition that already disrespects the concept of transparency, because there has already been a nonsynchronized movement between the two parts.

Boaventura, Hammer, and Buchli (2017) sought, in a later work, to estimate the force of interaction between the human and the exoskeleton. This type of approach is particularly interesting because it does not require sensors to directly measure such a magnitude, which always adds complexity to the system and can, depending on the type of sensor, make it larger, heavier, less efficient and more expensive. However, even if such interaction force sensors are present, the estimator can be used in conjunction to filter their

signals. As discussed in the previous work, this system is based on acceleration signals from both bodies.

Besides the topic of transparency in isolation, the concept of stability is noteworthy in this application. In a system that works in isolation, instability causes, in the worst case, system failure. However, an exoskeleton works coupled to a human being, so the loss of stability is likely to cause physical injury to the user (OKLE, 2016). It is possible, as done by Kazerooni et al. (2005) and Aguirre-Ollinger et al. (2012), to make the system unstable in isolation, but its coupling with the user brings stability to the system as a whole. Regardless of how it is implemented, such a controller needs to be robust enough to handle variations inherent to this type of plant, such as variations in the user's body structure or different contact situations between members and the environment.

2.2 Sensing

A harmonic and synchronized motion between the exoskeleton and its user is certainly the core aspect of transparency, which is directly translated into a continuous search for a negligible interaction force (ZANOTTO et al., 2013; BOAVENTURA; BUCHLI, 2016). Thus, the robot needs, in simple terms, to mimic the human's movements with the best possible tracking (KIM; DURFEE, 2018). As this type of response needs to be fast, a series of sensory techniques may be applied to prospect the necessary motion or torque profile to pass as input to the controller.

A remarkably anticipatory way of tracking the robot's user motion is by predicting the motion from motor cortex neuronal activity. Georgopoulos, Schwartz, and Kettner (1986) successfully fitted a regression that relates the frequency of discharge of motor neurons to the direction of movement in 3D space for the left arm of Rhesus monkeys. It is worth noting the concept of neuronal population activity rather than a single neuron in isolation. To capture brain activity, electrodes were surgically inserted into the primates' heads (GEORGOPOULOS; KALASKA, et al., 1982).

Analogous results were obtained by Nicolelis, Baccala, et al. (1995) while observing neuronal activity related to whisker movement in rats. Neural activity oscillations in the observed neuronal region started 500 ms before the actual whisker motion in 62.5 % of all episodes. This study also used implanted electrodes and Principal Components Analysis (PCA) (SMITH, 2002) to create the mathematical correlation. Another more recent work (NICOLELIS; CHAPIN, 2002) stated that "someday the research (...) could lead to devices that restore or augument other motor, sensory or cognitive functions". At that time, the researchers were able to link an owl monkey's motor cortex activity to the motion of two robot arms. It was also noted that the neuronal activity anticipates actual movement by a matter of 300 ms. A related article (WESSBERG et al., 2000) stated the use of a linear model associated with an artificial neural network to create the relation between neural

firing and hand position.

Apart from measuring the motor cortex activity to predict limb motion, it is also possible to monitor muscular fiber activity through surface electromyography (s-EMG). Lee and Sankai (2002) and Kawamoto and Sankai (2005) applied EMG on extensor and flexor of knee and hip as inputs for the HAL-3, a lower limb exoskeleton (Figure 1). Apart from serving as sensors for transparency or motion control during normal operation of the exoskeleton, EMG is particularly desirable during the design phase for detecting changes in muscular activity with or without a specific assistive system.

EMG has also been used in prosthesis control, as seen in Aeyels et al. (1995). In this case, an above-knee prosthesis received EMG signals from the stump muscles of the amputee. EMG shares the anticipative character of neuronal activity, as myographic signals start around 20 to 80 ms before the contraction begins (ZHOU et al., 1995).

Fleischer and Hommel (2008) used EMG as the main input for controlling the Technische Universität Berlin Powered Lower Extremity Exoskeleton (TUPLEE). This work employed a biomechanical model of the human body to compute motion directly from EMG data, rather than relying on machine learning techniques such as in Kiguchi et al. (2003). Biomechanical models may be more complex, but require no prior training as do supervised machine learning algorithms.

Moving away from monitoring electrical signals from the human neural or muscular systems, the human-robot motion coupling can have as input the notorious interaction forces between the human limbs and the robot links. The connection between these bodies is commonly made with some type of strap, as shown in Figure 5, which enables positioning some type of force sensor at the neighborhood of this interface.

Figure 5 – From left to right: EXO-TAO, BLEEX and ALEX II. Notice the recurrent usage of straps (marked in green) to connect the exoskeleton to the human user.

Source: Santos et al. (2017), Kazerooni et al. (2005), Zanotto et al. (2013)

A common way of measuring forces and torques between the user and the exoskeleton is to apply a multiaxial sensor at the anchor point of the strap on the corresponding link. The ALEX II (Active Leg Exoskeleton) (WINFREE; STEGALL; AGRAWAL, 2011) employs a force/torque sensor at each connection point, as well as a torque sensor at each actuated joint (ZANOTTO et al., 2013). Another robot, WPAL (Wearable Power Assist Leg) (SUN et al., 2007), estimates the wearer's intentions by monitoring leg reaction forces (also between straps and robot link), ground reaction force, joint (knee and hip) angles and body posture. Sun et al. (2007) stated that "biological signals such as myoelectricity cannot be measured properly"; besides being more antecipatory data, biological signals might not be so easily obtainable or of clear interpretation, as discussed before. The interaction sensors of the two exoskeletons mentioned are shown in Figure 6.

Figure 6 – From left to right: ALEX II and WPAL. Force and torque sensors are marked in green.

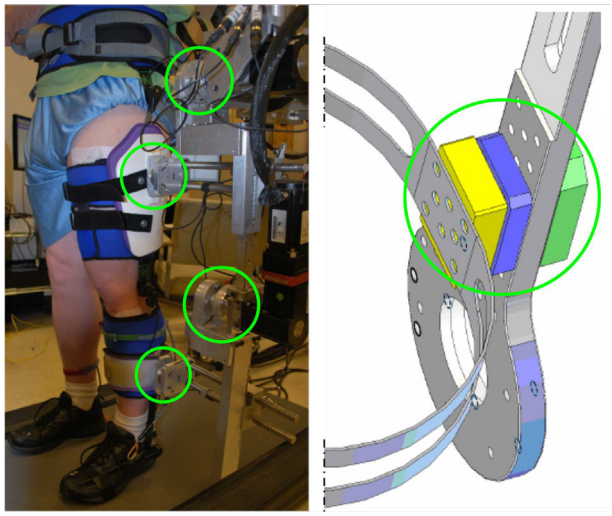

Source: Zanotto et al. (2013), Sun et al. (2007)

Furthermore, instead of sensing force-related quantities, the interaction may be monitored by means of kinematic variables (position and its derivatives). Boaventura and Buchli (2016) used IMUs in both the user and the robot, with a control system based on acceleration feedback, model-based feedforward (inverse dynamics) and state estimation. IMUs have the advantage, according to the authors, of being lightweight and easy to be integrated on the hardware. Apart from being used for transparency control, acceleration signals can also serve as inputs for estimating the interaction force, provided a good knowledge of the coupling compliance characteristics (BOAVENTURA; HAMMER; BUCHLI, 2017). This estimated force may dispense with the use of force/torque sensors, or be used as a filtering signal for noisy sensor data.

Apart from serving as inputs for transparency control methods, kinematic data is of vital importance for almost every robotic system, being utilized in feedback and feedforward controllers while also describing the current system state. Legged systems also

require knowledge about contacts between feet and ground (JARDIM; SIQUEIRA, 2009; LEAL-JUNIOR; DÍAZ, et al., 2019), describing which legs can be used as support, and computing the shape and size of the base of support.

Focusing on kinematic data, joint angles are a sensible choice for representing human body poses, mainly due to their independence of body shape and size. There are two main strategies for monitoring such quantities:

- Measure the position of the exoskeleton and, knowing the geometry and kinematics of the system, compute the pose of the human user connected to it;
- Directly measure the user's joint angles, decoupling such measurements from the attached robot.

The first approach has flexibility as one of the main advantages, as the robot can be designed from the ground up to house a number of sensors, with many actuators having at least one type of embedded sensor for closed loop operation. The geometry of the robot also is a design choice, making the required kinematic computations reliable. Nevertheless, such a strategy is limited to the part of the body where the exoskeleton is attached to, and there might not be a closed-form representation to map robot poses to user poses. This situation may happen with exoskeleton designs that boast additional degrees of freedom to compensate joint misalignment, or soft wearable robots.

Capturing user poses independently from the exoskeleton, on the other hand, may seem an additional burden to the user at first glance. However, sensor technology has evolved dramatically in the last few years, being still under active development, enabling smart solutions that may be as simple as putting on some clothes. Such direct measurements, as the name suggests, are easily mapped to joint angles and allow for capturing data on body regions outside the actuation boundaries of the exoskeleton, or in a more reliable way.

An example of human body position sensing is motion capture, where a set of stationary cameras recognize motion from a series of reflective spheres placed along the subject's body. This enables creating rich data (TERLEMEZ et al., 2014; MANDERY et al., 2015, 2016; MAHMOOD et al., 2019), however it is of limited applicability regarding exoskeletons, as it demands a structured environment with a set of specialized cameras installed. While such a scenario may occur in situations such as therapy, rehabilitation, or some specific industrial environment, exoskeletons in general are mobile robots, thus relying on embedded sensors.

A versatile and compact type of sensor is the inertial measurement unit (IMU), already adopted in wearable robots development (BOAVENTURA; BUCHLI, 2016). Each IMU is a combination of an accelerometer, a gyroscope, and a magnetometer, capable of

detecting linear acceleration and rotational rate thanks to the first two sensors, with the magnetometer serving mainly as orientation (due to the Earth's magnetic field). A 3D IMU contains one of each type of sensor for each coordinate axis.

Figure 7 – Commercial solutions for body motion capture that use inertial sensors.

(a) Xsens MVN Awinda. (b) Xsens MVN Link.

Source: Xsens (2020)

Commercial solutions employing IMUs for motion capture are already available from companies such as Xsens[1] or Motion Workshop[2]. One example product from Xsens uses a total of 17 IMUs for whole-body measurements, together with proprietary software. The sensors can be mounted to the user with individual straps or using a full-body fitted suit, offering "lab quality data in any field conditions" (XSENS, 2021) and requiring calibration for each individual subject. It is clear how this illustrative company is seeking improved usability and user comfort by designing a suit, which can be put on like a regular clothing, contrasting with using 17 individual straps.

One disadvantage of using IMUs for motion sensing is that human bodies have uneven surface shapes that additionally vary between individuals, posing a challenge in precise sensor positioning. This is sometimes treated with specific calibration postures that must be precisely mimicked by the subject. Such issues can be overcome by exploiting the human skeletal structure, as proposed by Seel, Raisch, and Schauer (2014). This method has the additional advantage of relying only on gyroscopes and accelerometers, thus not

[1] Available from: https://www.xsens.com/
[2] Available from: https://www.motionshadow.com/

suffering from distortions in the local magnetic field. It requires mounting a pair of inertial units on arbitrary locations of the neighboring links for each anatomical joint.

Measuring the complete pose of the human body, independently from the type of sensor used, is a problem of high dimensionality due to the large number of degrees of freedom involved. The AMASS dataset (MAHMOOD et al., 2019) uses a total of 24 spherical joints (72 angles) to describe the pose of the body, without hand motion or facial expressions (OSMAN; BOLKART; BLACK, 2020). When finger motion is considered, 30 additional joints are added (PAVLAKOS et al., 2019), with corresponding 90 DoFs, mapped to a 24-dimensional space using Principal Components Analysis (PCA) (SMITH, 2002). As a result, the number of sensors required is proportional to the large mobility of the human body. However, learning models can be applied to allow using fewer sensors. Huang, Kaufmann, et al. (2018) used only six IMUs and a recurrent neural network, the *Deep Inertial Poser* (DIP), to predict full-body poses. It produces smooth motions with rare inter-penetrations, using almost three times less sensors than the aforementioned full-body suits and relying on a simple calibration (holding a straight pose). Failure cases mostly relates to ambiguous motion, as the model focuses on orientation data, whilst acceleration would be the disambiguation factor (VON MARCARD et al., 2017). Huang, Kaufmann, et al. (2018) recognize the challenges of using such a variable due to "sensitivity to IMU placement, environmental factors, and different noise characteristics per sensor".

Following the concept of soft wearable robots, soft sensors are a different way to measure body poses. Instead of monitoring the relative orientation of body links, these sensors focus on the deformations caused by flexion and extension of each body joint. Some works from the State of the Art use a combination of silicone and liquid metal (MENGÜÇ et al., 2014) or a composite of conductive fabric and silicone (ATALAY et al., 2017). Mengüç et al. (2014) found that the developed solution is precise and robust to cyclic loading, however is not accurate enough to directly represent absolute joint positions. The silicone textile solution is highly linear with low hysteresis (ATALAY et al., 2017), apart from being suitable for batch fabrication. The lightness and compactness of this type of approach, capable of being easily integrated into some type of vest or suit, is a remarkable highlight.

Another type of sensor comprises polymer optical fibers (POFs). These fibers have higher attenuation compared to the silica optical fiber commonly used for data transmission, and superior mechanical properties such as higher strain resistance and higher flexibility (ZIEMANN et al., 2008). The underlying operating principle is that when a POF undergoes some physical change such as stress or bending, the light signal passing through it also modified, in terms of intensity (BILRO et al., 2012), phase, or wavelength. A sensor is created by analyzing the function that relates these two changes. Leal-Junior, Avellar, Díaz, et al. (2019) uses an intensity variation-based POF sensor to

measure multi-plane bending (roll, pitch, and yaw). A multiplexing technique, employing three LEDs and two photodetectors (LEAL-JUNIOR; DIAZ, et al., 2019), allows using a single fiber to detect 3D rotations with root mean squared (RMS) error inferior to one degree.

Regarding exoskeletons, polymer optical fibers have varied applications in measuring joint angles (LEAL-JUNIOR; FRIZERA; PONTES, et al., 2017), human-robot interaction forces (LEAL-JUNIOR; FRIZERA; MARQUES, et al., 2018) and ground reaction forces (LEAL-JUNIOR; DÍAZ, et al., 2019). Leal-Junior, Avellar, Jaimes, et al. (2020) put this multipurpose potential into practice by using POFs to measure the three previously listed variables, together with the user's breath rate, positioning a POF sensor on the chest. As a result, such proofs of concept indicate POFs as a lightweight, low-cost, and multipurpose sensory system.

To sum up, human body position sensing for wearable robot applications can be tackled by applying multiple types of sensors, including, but not limited to, IMUs, soft sensors, and POFs. Sensor fusion approaches, which mean combining different types of sensors to obtain richer or more accurate data, are also welcome, as well as learning algorithms like the DIP (HUANG; KAUFMANN, et al., 2018), bringing advantages such as dimensionality reduction or noise rejection. As pointed out by the literature, apart from delivering reliable performance in bench tests, any sensory system must be comfortable and easy to use from the user's perspective, while being robust to varying body shapes and sizes.

2.3 Biomechanics

A key aspect of exoskeletons is that the kinematic chain of an exoskeleton maps on to the human limb anatomy, configuring a one-to-one correspondence between human anatomical joints and the robot's joints (or sets of joints) (PONS, 2008, Chapter 1). These two chains must be mutually kinematically compatible for the interaction to be ergonomic and, as the ultimate goal, transparent. Thus, it is necessary to have some knowledge about the biological human system that interacts with the robot. Greater focus will be given on the lower limbs, as they are directly related to locomotion.

Concerning animal locomotion, the presently known locomotor systems are a result of millions of years of biological evolution, with the beautiful diversity of nature: enormous size and structural variations, apart from the different types of environment (BIEWENER; PATEK, 2018). Speaking of terrestrial animals, a large amount of their energy is spent moving, searching for food or escaping from predators. Therefore, it is a natural necessity (and an objective function for evolution) that locomotion is done with minimal energy consumption, without injuring the animal tissues, while still keeping required precision (PONS, 2008, Chapter 2).

It is not different with bipeds: human gait can be defined as the translation of the body center of mass with minimal expenditure of energy (KOOPMAN, 1989). A natural energy-efficient trajectory can be generated with three pelvic motions (rotation, tilt and lateral displacement), knee flexion and double ankle-knee interaction (SAUNDERS; INMAN; EBERHART, 1953). Furthermore, human muscles are not active during the whole gait, but only in certain phases, which is highly energy-efficient (SAUNDERS; INMAN; EBERHART, 1953). Humans also naturally select a combination of step length and cadence for each walking speed (BERTRAM; RUINA, 2001) and even an optimal speed (RALSTON, 1958), everything seeking a minimal metabolic rate.

As a result, all previous mechanisms must be taken into account when designing a transparent exoskeleton for locomotion assistance. Other key aspects regarding specially mechanical design are related to lower limb (leg) kinematics. They enable the individual to stand (weight bearing) and locomote (propulsion). The main joints are: hip, knee and ankle, connecting pelvis, upper leg, lower leg, and foot (MOORE; AGUR; DALLEY, 2018). The following paragraphs will focus on the main degrees of freedom (DoFs) of each joint, as this definition is vital for the correct design of a lower-limb exoskeleton.

The *hip joint* is a multiaxial ball-and-socket synovial joint, behaving like a spherical joint, allowing three rotations (PONS, 2008, Chapter 3). The hip is a very strong and stable joint, responsible for transferring body weight from the pelvis to the legs. The joint itself is made up of an acetabulum on the hip bone and the head of the femur, as seen in Figure 8. This same figure compares bipeds and quadrupeds, clarifying the importance of the oblique orientation of human femurs. Hip joint movements and typical ranges are given by (MOORE; AGUR; DALLEY, 2018):

- *Flexion-extension:* flexion brings the thigh forward and upward, the opposite is extension. The complete range is up to 120°;
- *Abduction-adduction:* abduction moves the lower limb away from the mid-line of the body, ranging up to 40°. Adduction is the opposite and ranges between 30° and 35°.
- *Medial-lateral rotation:* medial rotation rotates the leg around its own axis so that the toe points medially, with a range of only 15° to 30°. Lateral rotation points the toe laterally, with a larger range, up to 60°.

Next comes the *knee joint*, the body's largest joint, with a big surface area of complicated shape (MOORE; AGUR; DALLEY, 2018). It connects the oblique femur with the vertical lower leg, being mechanically weak because of the incongruence of the articular surfaces (two spheres on a warped surface). Thus, the surrounding muscles, tendons, and ligaments play an important role on stabilizing this joint, shown in anterior view in Figure 9. This joint has a very special and efficient feature: it locks on the fully extended position,

Figure 8 – (A) The weight of the upper body is transmitted vertically through the vertebral column, being divided laterally through the sacrum and ilia, reaching the acetabulum of the hip joint. The head of the femur then directs this weight down and obliquely towards the center. (B) Bipeds have diagonal femurs to bring the base of support directly inferior to the trunk, as during walking the whole body is supported by one foot at a time. On the other hand, quadrupeds have essentially vertical limbs, requiring support from both sides of the body.

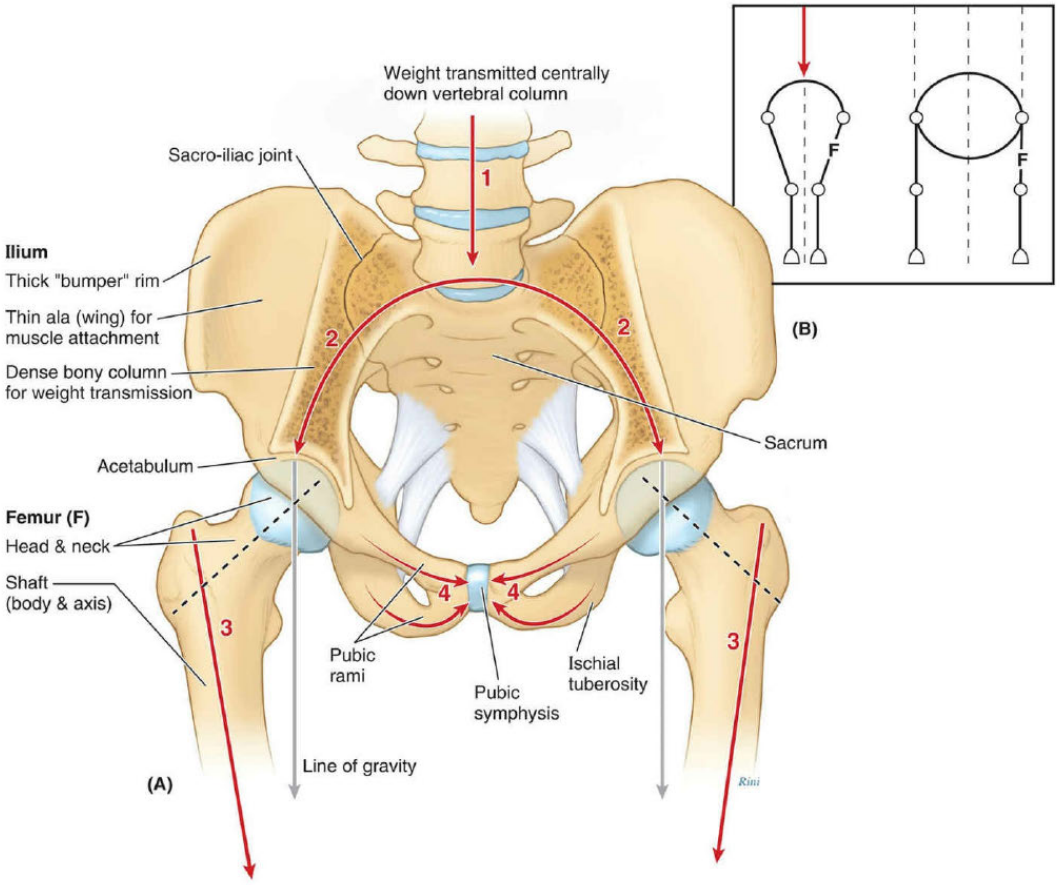

Source: Moore, Agur, and Dalley (2018)

enabling weight bearing in the standing position with minimal muscular activity (PONS, 2008, Chapter 3). The knee can be roughly approximated by a hinge joint, with most of its motion on the sagittal plane. Its movements are (MOORE; AGUR; DALLEY, 2018):

- *Flexion-extension:* in flexion, the shank approaches the thigh while femur and tibia remain coplanar, with a maximum range of 120° (hip extended), 140° (hip flexed) or 160° (passive knee flexion). Extension is the opposite motion; in full extension, the knee locks, enabling weight bearing and freeing the patella (it sits loosely inside the joint);

- *Medial-lateral rotation:* this motion is possible when the knee is flexed (unlocked). Medial rotation goes up to 10° with 30° of flexion and 15° with full flexion. Lateral

(external) rotation is wider, ranging up to 30° with 30° of flexion and 50° with 120° of flexion.

Figure 9 – Anterior view of the knee joint, including the hip bone and femur to show the Q-angle (diagonal femur orientation).

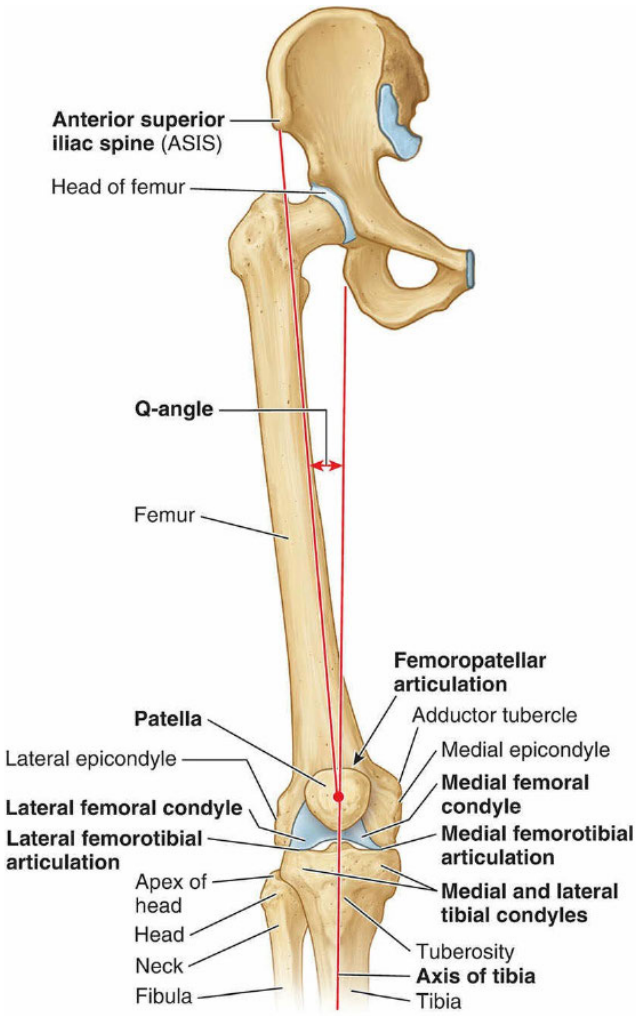

Source: Moore, Agur, and Dalley (2018)

The third and last joint is the *ankle joint*, connecting the lower leg to the foot. When considering the ankle and foot together, there is an incredible number of bones, joints, muscles, tendons, and ligaments within that relatively small volume. This large number of elements connected together give the foot ability to deform with each ground contact, serving as a damper for contact-inherent impacts. Furthermore, the arches of the foot (longitudinal and transverse) are restrained by flexible tendons, contributing to weight-bearing capabilities, propelling during walking, running and jumping, and adaptability to different shapes of contact surfaces (MOORE; AGUR; DALLEY, 2018). All these characteristics of the main base of support of humans may be of great value when designing the soles of wearable robots.

Returning to the ankle joint, it is a hinge-type synovial joint, shown in Figure 10. Its main movement is flexion, however the space inside the joint allows some further movements, as following described (MOORE; AGUR; DALLEY, 2018).

Figure 10 – Ankle joint demonstrated radiographically, in lateral (A) and anteroposterior (B) views.

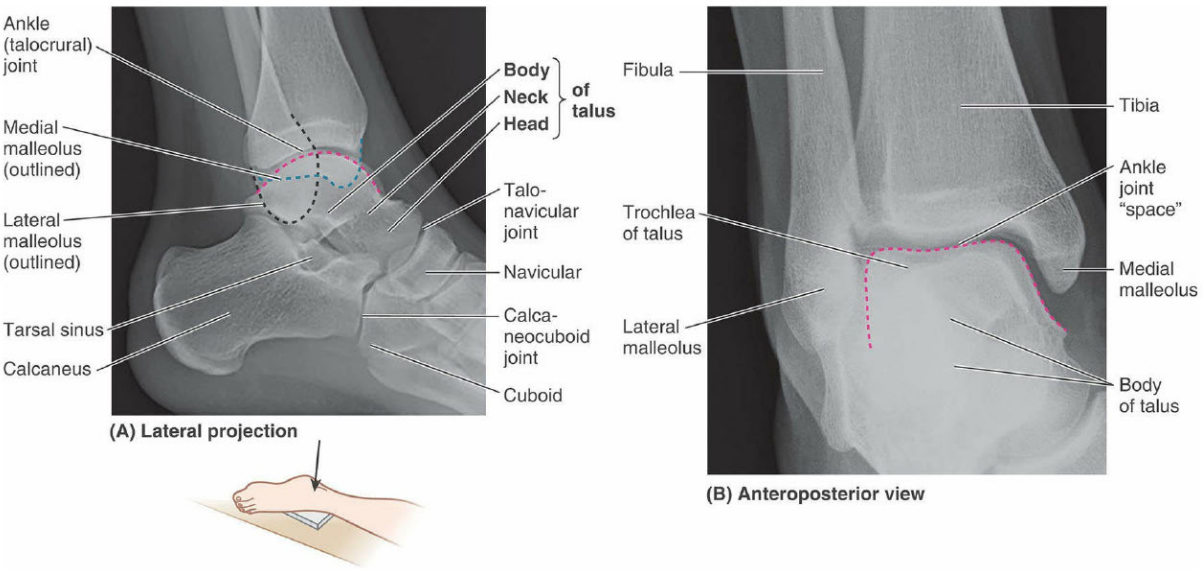

Source: Moore, Agur, and Dalley (2018)

- *Dorsiflexion:* this movement brings the foot dorsally to the anterior surface of the leg, ranging up to 20°;
- *Plantarflexion:* opposite to dorsiflexion, is the characteristic foot position in ballet toe dancing. The range is from 40° to 50°;
- *Eversion:* rotates the foot so that the sole points away from the median plane. When standing up, eversion presses on the inside part of the sole. Ranges between 15° and 20°;
- *Inversion:* contrarily to eversion, rotates the foot sole towards the median plane. When standing, inversion puts pressure on the outside part of the sole. Range is a bit wider, between 30° and 35°.

2.4 Physical human-exoskeleton interaction

Revisiting the concept of exoskeletons, these are robots that operate in close contact with humans, being continuously attached to the latter's limbs. As a result, any type of interaction will manifest itself in terms of forces exchanged between the two systems (robotic and human). To make the human user feel comfortable during this interaction,

the coupling between them must be designed bearing in mind the way humans perceive physical interactions.

2.4.1 Human physiology

Concerning force and pressure application on the contact between human and exoskeleton, primary attention is given to the human tactile sensory system. The human force and pressure sensory system has varied receptors; among them, mechanoreceptors are the ones that detect several types of mechanical stimuli: pressure, touch, vibration, strain, and tactile sensation. These sensors are mainly located in the skin (SILBERNAGL; DESPOPOULOS, 2011), along with receptors for pain and temperature.

Other important classes of receptors are proprioceptors, named this way because they provide information about the person's internal state, describing the orientation of limbs relative to each other and their relative speeds. They generate the human's sense of position, movement, and force (PONS, 2008, Chapter 5). Knowing this basic information about what the human body is able to feel in a mechanical point of view, it is possible to note some key aspects regarding exoskeleton design that directly affect these sensations.

2.4.2 Exoskeleton design for harmonic interaction

In general terms, an exoskeleton must be, apart from safe to use, ergonomic and comfortable for its user (SCHIELE; HELM, 2006). When necessary, it must apply forces on its user in a conscious and controlled way. The first factor to be considered is the kinematic compatibility between the robot and its user is that the exoskeleton's kinematic chain must be designed in such a way that the user does not have its natural biomechanics affected (see section 2.3). This is a challenge when facing the wide range of variations observed in different individuals, regarding aspects such as limb length, joint orientation, and corporal mass (PONS, 2008, Chapter 5).

One of the most pressing problems that can make the human-robot interaction extremely unpleasant is joint misalignment. This occurs when a particular joint of the human is oversimplified, resulting in a robot with less DoFs than necessary to enable complete motion of that specific joint. However, even when the number of DoFs is compatible, perfect alignment between the corresponding joints of the human and the robot may not be achieved, usually resulting in secondary interaction forces during motion, such as shear forces between the band and the user's skin. These joint misalignments can even arise from slippage of connection surfaces (COLOMBO et al., 2000).

Thereafter, motor incompatibilities are possible and have adverse effects, disturbing users in such a way that forces them to change their natural motion patterns (HIDLER; WALL, 2005). It is then essential that specific design criteria is respected. Schiele and Helm (2006) state that a truly ergonomic exoskeleton must be able to:

- Interact with the complete workspace of the human limb(s) of interest;
- Induce exact torques, positions and velocities to the human joints, being thus able to resolve redundancies;
- Not cause discomfort or safety hazards for the user.

The previous criteria are then achieved with the following design principles:

- An exoskeleton must be wearable (not end-point based[3]);
- An exoskeleton must have no more than 6 DoFs between two consecutive attachments;
- An exoskeleton must *not* be kinematically equivalent to the human limb it interacts with. This item mitigates the small misalignments stated before and enables structures that are easy to use and require no adjustments to fit specific individuals.

An example of a kinematically nonequivalent exoskeleton is the *Robomorphism* (ACCOTO; SERGI, et al., 2014), mentioned in Section 2.1. The authors described it as a nonanthropomorphic system, having as one of its main characteristics the intrinsic tolerance to misalignment.

2.4.3 Application of interaction forces to human tissues

In scenarios such as rehabilitation or unstable body position, the exoskeleton must actively produce forces that help the user to perform a specific task, or to recover balance and prevent from falling. During these or other situations, loads will be directly applied to the anchor points between the user and the exoskeleton, which is definitely not transparent, but essential for a safe and healthy operation. Applied pressure must not exceed the ischemic level, the pressure at which capillary vessels are unable to conduct blood and the tissue is compromised. This level is estimated at 30 mmHg (LANDIS, 1930), or 4 kPa.

Apart from being safe, the interaction must also not be uncomfortable, however comfort is very subjective and hard to quantify. Thus, strategies must always focus on pressure-tolerant areas or distributing the load over a large surface. General recommendations include avoiding the following particular regions (PONS, 2008, Chapter 5):

- Surfaces around or near to joints;
- Bony prominences, tendons and nerves;

[3] An end-point based exoskeleton is body- or wall-grounded and is only attached to the hand or foot of the human user (PONS, 2008, Chapter 3). Contrarily, a wearable exoskeleton is attached at several locations along the limbs.

- Areas with surface vessels or highly irrigated.

Regardless of the region chosen, interaction forces will always be applied to the human skin, thus the connection is mediated by soft tissues. These are quasi-incompressible, non-homogeneous, anisotropic, nonlinear viscoelastic tissues, described in mechanical terms as a combination of nonlinear elastic and viscoelastic elements (MAUREL, 1999). On top of these tissues, right on the skin, attachment elements are positioned, possessing the following high-level requirements (ROCON; RUIZ, et al., 2005):

- *To ensure the correct placement of the exoskeleton:* this is obtained with several points of connection between the attachment and the robot link, contributing for a stable fixation;
- *To maximize the transmission of forces:* the contact stiffness can be increased by compressing the underlying human tissues (to a comfortable extent), as their stiffness increases as they are compressed (nonlinear elasticity);
- *To be comfortable, easy to wear, adjust, use, and remove.*

In addition to contributing for a higher contact stiffness, slight compression of human tissues is beneficial for the muscles during sportive activities such as jumping (KRAEMER et al., 1998) or throughout recovery periods (BORN; SPERLICH; HOLMBERG, 2013).

2.5 Motion prediction

As previously shown in this chapter, many transparency control techniques of the State of the Art rely on some of the following techniques, or combinations of them: force feedback, electromyography (EMG), neuronal activity monitoring, impedance or admittance controllers, and model-based feedforward controllers. All these techniques, despite quite dissimilar, share a common characteristic: they all depend on the current and/or previous states of the system to compute actuator outputs. Combined with delays and characteristic cycle times of digital control systems, any action taken by the robot will always be a fraction of time delayed from the states that were measured and used to calculate it.

However, exoskeleton robots are mechanically coupled to a human organism, which possesses high sensitivity regarding mechanical stimuli. As mentioned in the previous section, there is an intricate network of mechanoreceptors distributed over the skin. Moreover, reaction times involving tactile stimuli are of the order of 245 $\pm$ 14 ms (BARNETT-COWAN; HARRIS, 2009). Thus, to be rendered imperceptible (transparent), the robot must move in synchronization with its user, leaving almost no room for delays or motion incompatibility.

It must be noted that, as seen in Section 2.2, there are neurological signals that possess some anticipation relative to the corresponding muscle motion. However, monitoring such quantities is somehow invasive (implanting electrodes on the brain or placing EMG sensors on the skin) and requires greater effort for interpreting the acquired values, when compared to sensing variables such as limb or joint poses.

Seeking to solve this antagonism, instead of relying exclusively on measured quantities, future state predictions can be employed to build transparency algorithms that are able to look ahead. For example, a predictive feedforward controller combined with force-feedback is effective in minimizing interaction forces, according to (JARRASSÉ et al., 2008). The aim of the mentioned work was to assess the effectiveness of using predictive inputs for transparency control, not generate such predictions, which came in turn from previously recorded free motion experiments.

Predicting a voluntary motion generated from a human arbitrary intent may seem strange at first glance; however, it is worth noting that human locomotion follows a series of minimal energy principles (recall Section 2.3). As a result, many motion patterns can be interpreted not as fully arbitrary, but somewhat related to these innate choices.

There is a wide range of works focused on the prediction of gait dynamics (CALDAS et al., 2017), with varied objectives. Gaussian regression, for instance, is capable of dealing with large amounts of highly correlated data (YUN et al., 2014), being used for rehabilitation by Glackin et al. (2014). Motor behavior prediction based on physical characteristics is addressed by Luu et al. (2014), applying Fourier series and artificial neural networks. This specific method has high mathematical complexity, which may require substantial computational power. This is an important aspect for developing such algorithms: they must be fast enough to enable high control bandwidth in real-time.

Other approaches involve optimality and energy efficiency principles (ACKERMANN; VAN DEN BOGERT, 2010) or bio and neuromechanical models (BLICKHAN, 1989; GEYER; HERR, 2010). Phase and event detection (BEJARANO et al., 2014; MARTINEZ-HERNANDEZ et al., 2017) are also important topics in gait analysis and possibly useful tools for prediction algorithms. In fact, walking gait can be described as a sequence of states (FORNER-CORDERO; KOOPMAN; VAN DER HELM, 2006) that preserves intrinsic variability of human motion (HAUSDORFF et al., 1995; WEST; GRIFFIN, 1999; DINGWELL; CUSUMANO, 2000), instead of assuming strides as periodic events and averaging them (WINTER; YACK, 1987). The cyclic behavior of walking can be exploited to create predictive control algorithms (DIJK; KOOIJ, et al., 2013), requiring additional models to address sudden motions or irregular gait patterns.

An important reference on this topic comes from Bruno Pisi Garcia, fellow researcher

of the author. In his Scientific Initiation work[4], he proposed a simple and robust walking motion prediction system. Being a data-driven approach, it starts from segmenting walking gait trajectories based on peak values of hip flexion/extension, as these are well defined for a normal walking gait. These segments are then converted into a fixed number of frames. Prediction is done through a *clustering* technique, which defines some trajectories as reference, according to their prediction capacity, and linear operators for computing each future frame. Prediction learning is accomplished through a recursive least squares filter (HAYES, 2009), while cluster succession uses a K-Nearest Neighbors (KNN) classifier (DUDANI, 1976).

Another family of algorithms used for motion prediction are recurrent neural networks (RNNs), capable of processing sequential data (more on that on the next section). Architectures may vary (MARTINEZ; BLACK; ROMERO, 2017), and also the pose representation: for instance, Pavllo, Grangier, and Auli (2018) use quaternions as representation within the recurrent network. An interesting application involving autonomous vehicles is shown by Du, Vasudevan, and Johnson-Roberson (2019), using physical constraints to improve prediction realism. A neural network with internal structure related to the human skeleton morphology is proposed by Aksan, Kaufmann, and Hilliges (2019), enabling to solve motion degrading issues observed in other methods.

2.6 Artificial neural networks

The concept of artificial neural networks, something increasingly present nowadays, is as old as the 1940s (HAYKIN, 2009), when McCulloch and Pitts (1943) introduced the underlying ideas of neural networks. Later, Rosenblatt (1958) introduced the *perceptron*, a mathematical equivalent of a biological neuron. The perceptron is a rather simple and elegant concept: it takes a weighted sum of its inputs added with a bias and passes this result through a nonlinear activation function. This nonlinear characteristic is what makes neural networks powerful: a network composed by a finite number of perceptrons linked together can approximate any arbitrary function. This is, in simple terms, what states the *universal approximation theorem* (CSÁJI et al., 2001).

Starting from the previous foundations, neural networks with diverse architectures started to be used to solve increasingly complex problems from several different areas, which became feasible thanks to advances in computer hardware, with notably more powerful central processing units (CPUs) and graphical processing units (GPUs), the latter specially suited for parallelism. Another milestone in neural networks history is the LeNet-5 (LECUN et al., 1998), considered the first convolutional neural network (CNN), incorporating the concepts of convolution and subsampling (pooling). This type of network is very powerful in evaluating inputs with high dimensionality (interpreted as matrices).

[4] Available from: https://bv.fapesp.br/52133

Convolutional neural networks have important properties such as space independence (LE et al., 2011), being robust to rigid transforms (translation and rotation) applied to the input data. All these characteristics made this type of network well suited to work with images as input, as seen in the famous ImageNet[5] challenge and its most successful networks, starting with the AlexNet (KRIZHEVSKY; SUTSKEVER; HINTON, 2012) in 2012 and counting with astonishing results such as the 3.6 % top 5 error in the ResNet (HE et al., 2016). ImageNet focuses mainly on image classification, which is the process of giving a label to an image (identifying objects, people or animals, for example), however convolutional networks have also been successfully applied in other types of data, such as music (OORD; DIELEMAN; SCHRAUWEN, 2013).

All the previously cited works are a subset of *supervised learning*, in which neural networks are trained to fit a function that generalizes the information found in a labeled data set. Taking the ImageNet as example, one shows an input image *and* the desired label to the network, which will apply backpropagation (HAYKIN, 2009) and update all its weights and biases to increase the likelihood of outputting the correct label. In this framework, neural networks with different architectures have proven to be a great tool to solve many problems, being able to generate more abstract knowledge as they get deeper (higher number of layers).

Another important class of artificial neural networks comprises *recurrent neural networks* (RNNs). All previous examples of networks, despite showing impressive results of generating remarkably deep and abstract understandings, are incapable of analyzing sequential data, such as temporal events or texts (sequences of words). In contrast, recurrent neural networks have some type of persistent hidden state, capable of storing information while sequences of different inputs are given. The two main implementations of RNNs are the Long Short-Term Memory (LSTM) (HOCHREITER; SCHMIDHUBER, 1997) and the Gated Recurrent Unit (GRU) (CHO et al., 2014), each one with its particular aspects and key strengths (CHUNG et al., 2014). Often used for text processing applications such as translation (SUTSKEVER; VINYALS; LE, 2014), RNNs have a potential in understanding time sequences characteristic of dynamic systems.

There also is another set of problems at which the input-output pair (image and label, recalling ImageNet) is unknown or very difficult to describe for training a network in a supervised fashion. However, it is possible to state how positive or negative the outcome of a given network output is. Developing algorithms for neural networks to adjust themselves seeking to maximize the goodness of their actions is what is called *reinforcement learning* (SUTTON; BARTO, 2018), which is currently making great advances and bringing artificial intelligence to an even broader scope of applications.

The underlying process of reinforcement learning is composed by an *agent* that

[5] Available from: http://image-net.org/challenges/LSVRC/2016/index

interacts with an *environment*, choosing *actions* driven by a specific *policy* and receiving *rewards* for that specific action in a particular environment *state*. The goal of the agent is to adjust its policy so that it maximizes the expected *return* (return is composed by the *discounted sum of rewards*: it considers the immediate reward for a given action and an optional weighted sum of future rewards). Before moving on, it is important to note that reinforcement learning does not need a data set: instead, the agent creates its own training information by continuously interacting with the environment.

Some recent and impressive achievements of reinforcement learning involved mastering a number of games. After learning to play 49 Atari games using raw images as input data (employing the convolutional networks cited before) and an artificial agent called *deep Q-network* (MNIH et al., 2015), DeepMind[6] created an AI to play the game of Go, called AlphaGo (SILVER; HUANG, et al., 2016), that was able to defeat the world champion, Lee Sedol. Due to the incredibly large number of possible board configurations in Go (superior to the estimated total number of atoms in the universe), this has always been a great challenge for AI, and its solution was thought to be at least a decade away (SILVER; HUANG, et al., 2016). AlphaGo started its training with a vast number of Go games played by professional humans, using afterwards self-play to refine the acquired knowledge. After that, AlphaZero (SILVER; HUBERT, et al., 2018) was created, which is a general AI capable of mastering different games (chess, shogi and Go) using only self-play, knowing *a priori* nothing more than the basic rules of the games. DeepMind also created a grandmaster level AI (VINYALS et al., 2019) for StarCraft 2, a very complex strategy computer game. Another computer game was also recently tackled by OpenAI[7]: Dota 2 (BERNER et al., 2019). Apart from involving strategy as in StarCraft 2, Dota 2 is played in teams of 5, relying on team work for consolidating the victory. The final AI, called OpenAI Five, consistently defeated the current world champion human team.

With that information in mind, some considerations can be made:

- Artificial intelligence in the form of deep neural networks is proving to be able to learn abstract concepts, such as strategy, long-term planning, and team work. However, the manner at which they learn and how this knowledge is established is still difficult to interpret (ZEILER; FERGUS, 2014);
- Reinforcement learning broadens the scope of AI and enables algorithms to build knowledge without human interference, which can be interpreted as room for creativity;
- Given a sufficient amount of computational power, the time scale in which the agent learns can be much faster than real time. As an example, OpenAI Five (BERNER

[6] Available from: https://deepmind.com/
[7] Available from: https://openai.com/

et al., 2019) played about 45,000 years of Dota 2 in 10 real time months to achieve its final form;

- Learning algorithms can be interpreted as a step in evolution. To adapt to the environment, survive and reproduce more efficiently, natural selection (DARWIN, 1864) favors species that can reason logically and acquire knowledge. By creating systems that can learn to solve problems that were hard to tackle by humans, humanity itself is broadening the scope of problems that it can solve, becoming thus more adapted.

The broad application scope of machine learning and artificial neural networks also encompasses wearable robots. Exoskeletons used for rehabilitation can apply learning algorithms to correct abnormal joint trajectories, predicting personalized healthy motions for the patients (LIU et al., 2016). This one-to-one approach is, according to the authors, more beneficial then a generic pre-recorded motion. Also regarding rehabilitation, a promising therapy is to use exoskeletons to provide just the amount of assistance the patient requires (LYU et al., 2019), encouraging a more engaged behavior and consequently greater health benefits (IBARRA et al., 2014). Neural networks are also useful for gait analysis and motion pattern recognition (WANG; WU, et al., 2018; ZHENG et al., 2019). Relevant environmental factors are also capable of being represented by learning models, such as terrain slope (LEE; KANG, et al., 2021), which directly influences joint torque profiles. Control schemes can also benefit from machine learning, particularly deep reinforcement learning, with a potential of generating robust controllers that build intrinsic knowledge of the system dynamics (ROSE; BAZZOCCHI; NEJAT, 2020; ROSE, 2020) without requiring analytic system modeling. Last, as mentioned in the previous section, neural networks can be used to predict human motion, which can potentially provide anticipation to exoskeleton motions, synchronizing them with the user's intent.

2.7 Dynamic legged stability

Human beings, during two-legged standing or walking, are bipeds, characterized by a high position of their center of mass compared to a relatively small base of support (BALANCE, 2014). This creates an almost boundary stable system regarding upward posture, similar to an inverted pendulum. Thus, bipeds must always be concerned about their own balance to avoid falling. Some instinctive human behaviors include the *ankle strategy*, that moves the center of pressure[8] (CoP) along the base of support (BoS) and the *hip strategy*, that moves the upper body contrarily to the lower body, changing the body's total angular momentum (HORAK; NASHNER, 1986; KUO; ZAJAC, 1993). Arm

[8] The *center of pressure* of a human's base of support is the virtual point where the ground reaction force vector passes through (BALANCE, 2014).

motion also contributes to balance (BRUIJN et al., 2010), in addition to foot placement adjustment, taking small steps when necessary (TOWNSEND, 1985).

According to Wieber (2002), "the major issue for walking systems is to avoid to fall, and more precise objectives can be taken care of only when this point is guaranteed". Transparent behavior can be classified as a "more precise objective". Nevertheless, it is not trivial to state how stable a biped system is. Additionally, for application on control strategies, the result must be quantitative, or at least binary (*stable* or *falling*). For instance, an exoskeleton-oriented work used the inverted pendulum model for the human and a feedforward controller for returning the system to an upright posture (VALLERY; BÖGEL; RIENER, et al., 2012). The inverted pendulum is just one of the various metrics available for quantifying dynamic postural stability and thus define a *stability index* (BALANCE, 2014) to be used as input for the exoskeleton's controllers.

In the context of transparent wearable robots, it only makes sense to enable fully transparent operation when postural stability is guaranteed. If the robot perceives a loss of stability (through monitoring some type of stability index), it must assume a more active behavior, assisting its user to recover balance and return to a stable state. Then, it is safe to return to a transparent operating mode. Balance recovery is instinctively performed by healthy individuals in a number of different ways, depending on the type and timing of the perturbation (DUYSENS; FORNER-CORDERO, 2018). Apart from the aforementioned ankle and hip strategies, swing foot elevation and lowering (FORNER-CORDERO; KOOPMAN; HELM, 2004) and trunk flexion (FORNER-CORDERO; KOOPMAN; VAN DER HELM, 2014) are other possible recovery strategies.

The amount of stability a human possesses at a determined time is a result of the large number of dynamic variables related to it, translated in mathematical terms to the state-space representation. More high-level data may be obtained in the feature space, such as 3D positions of center of mass (CoM) and center of pressure (CoP). It is clear that all the data available is dynamic and of big dimensionality, one of the possible causes of the lack of consensus in how to judge or score, quantitatively, the dynamic stability of human locomotion (HURMUZLU; BASDOGAN, 1994; BRUIJN et al., 2013). Thereafter, some selected methods for quantifying dynamic bipedal balance are presented, with potential for serving as tools for defining a stability index.

2.7.1 Inverted Pendulum Model Approach

This technique exploits the inverted pendulum representation of a biped to compute step length. Assuming a constant leg length, the model computes the size d of the step required to reach the next step with zero velocity and upright position (COROS; BEAUDOIN; PANNE, 2010). According to Figure 11, the energy balance equation is given by:

Figure 11 – Inverted pendulum model for a biped walker.

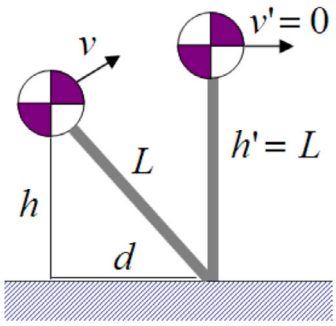

Source: Coros, Beaudoin, and Panne (2010)

$$\frac{1}{2}mv^2 + mgh = \frac{1}{2}mv'^2 + mgh' \tag{2.2}$$

Determining $v' = 0$ and $h' = L = \sqrt{h^2 + d^2}$ and solving for d, the step length is given by:

$$d = v\sqrt{\frac{h}{g} + \frac{v^2}{4g^2}} \tag{2.3}$$

Instead of always reaching an upright position with zero velocity, the biped can take shorter steps and keep the center of mass moving at a positive velocity. This is done by simply subtracting a fraction of the desired velocity, as shown:

$$d' = d - \alpha v_d \tag{2.4}$$

Coros, Beaudoin, and Panne (2010) used a fixed value of 0.05 for α, recalling that the whole system of the referred work also had a velocity tuning component. Moreover, the previous procedure considers just a planar motion; thus, the computation must be performed twice, once for the sagittal plane and once for the coronal plane, computing the desired step length for each direction, which are then composed into the final spatial result.

The d (or d') resultant value can be used as a stability index, as big values of step length translate into a posture that demands a large effort to keep balance. Moreover, the step length in the two body planes can be used as an input for a stability controller, playing a role similar to the one of the original work, controlling the motion of biped bodies simulated within a computational physics engine.

2.7.2 Capture Point

Stability for a biped can be defined as whether or not the biped will fall down (PRATT; TEDRAKE, 2006). For that, the system must be able to place its swinging foot in a proper location, enabling itself to *capture* its kinetic energy and stably stop in a finite number of steps. The following set of definitions introduce this topic:

- *Capture State:* state in which the kinetic energy of the biped is zero and can remain zero with suitable joint torques;
- *Safe Feasible Trajectory:* trajectory through state space that is consistent with the robot's dynamics, is achievable by the robot's actuators, and does not contain any falling states;
- *Capture Point:* for a biped in state x, a Capture Point, p, is a point on the ground where if the biped covers p, either with its stance foot or by stepping to p in a single step, and then maintains its center of pressure to lie on p, then there exists a Safe Feasible Trajectory that ends in a Capture State;
- *Capture Region:* the set of all Capture Points;
- *Reachable Region:* region on the ground that can be reached kinematically by any point on the bottom of the swing foot.

The concepts of capture point and capture region, first defined referring to a single-step motion, can be easily extended to multiple steps:

- *Two-step Capture Point:* a point on the ground, p, such that if the biped swung its swing leg to cover p with its foot and maintained its center of pressure to lie on p, then there exists a Safe Feasible Trajectory, such that at some state along that trajectory, there exists a Capture Point;
- *Two-step Capture Region:* the set of all two-step Capture Points;
- *N-step Capture Point:* a point on the ground, p, such that if the biped swung its swing leg to cover p with its foot and maintained its center of pressure to lie on p, then there exists a Safe Feasible Trajectory, such that at some state along that trajectory, there exists an N-1-step Capture Point;
- *N-step Capture Region:* the set of all N-step Capture Points.

From the previous definitions, Pratt and Tedrake (2006) proposes velocity-based stability margins:

- *Zero-step Capture Margin:* maximum distance from points in the capture region to their closest edge of the support polygon if the Capture Region and support polygon intersect. Otherwise, the negative distance from the Capture Region to the support polygon;
- *One-step Capture Margin:* maximum distance from points in the capture region to their nearest boundary of the Reachable Region if the Capture Region is nonempty. Otherwise, the negative distance from the Unreachable Capture Region to the Reachable Region;
- *N-step Capture Margin*: maximum distance from points in the N-step Capture Region to their nearest boundary of the Reachable Region if the n-step Capture Region is nonempty. Otherwise, the negative distance from the Unreachable N-step Capture Region to the Reachable Region.

Computing the Capture Region for a generic humanoid robot can be very difficult (PRATT; CARFF, et al., 2006). However, simplified walking models can be used to allow for such a computation, with an appropriate level of detail. The main models used are listed below and illustrated in Figure 12.

- *3D Linear Inverted Pendulum (LIPM) with point foot* (KAJITA; TANI, 1991; KAJITA; KANEHIRO, et al., 2001): comprises a point mass in the hip bone location, and a massless telescoping leg. This is the most basic model, focusing mainly on foot placement as balance strategy;
- *3D-LIPM with finite-sized foot* (KOOLEN et al., 2012): this model adds a massless, finite-sized foot at the end of the telescoping leg, connected with a 2-DoF ankle joint. This allows applying torques at the foot location, adding an ankle strategy (HORAK; NASHNER, 1986; KUO; ZAJAC, 1993) to the robot's repertoire;
- *LIPM plus flywheel* (PRATT; CARFF, et al., 2006): this model keeps using a point foot, but replaces the point mass with a rotating flywheel. Such an addition enables modeling instinctive human behaviors such as forward lunges and rapid arm rotations;
- *3D-LIPM with finite-sized foot and reaction mass* (KOOLEN et al., 2012): the most complete simplified model, extending the 3D-LIPM with finite-sized foot by replacing the point mass with a reaction mass, possessing a nonzero inertia tensor.

Capture Point dynamics have been successfully used for locomotion control of biped robots (ENGLSBERGER et al., 2011; PRATT; KOOLEN, et al., 2012), enabling them to robustly regain balance after receiving external perturbations (pushes). Thus, this approach is also capable of being used for both stability computation and trajectory planning and control.

Figure 12 – Simplified walking models for the capture point theory.

(a) 3D-LIPM with point foot

(b) 3D-LIPM with finite-sized foot

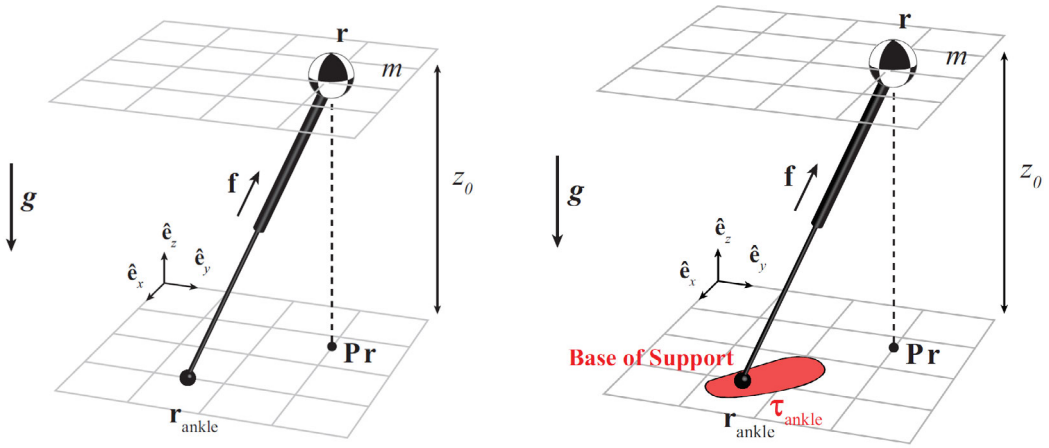

(c) LIPM plus flywheel

(d) 3D-LIPM with finite-sized foot and reaction mass

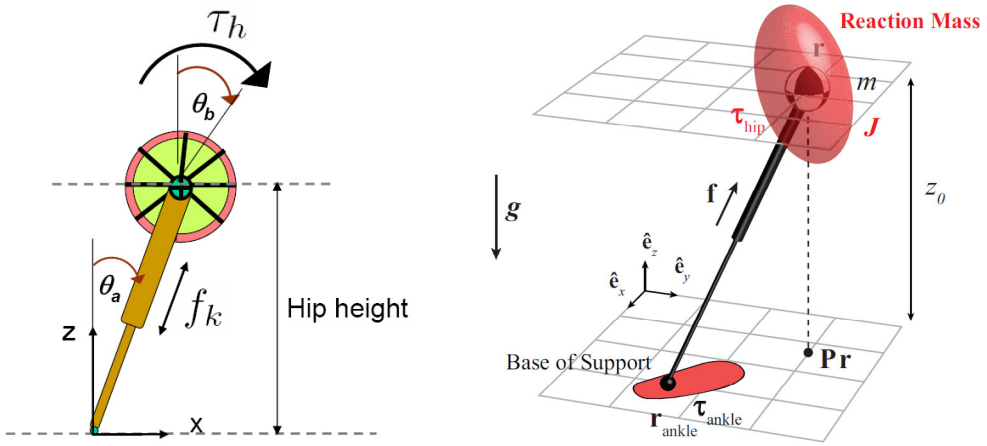

Source: Koolen et al. (2012) and Pratt, Carff, et al. (2006)

2.7.3 Extrapolated Center of Mass

The well-known condition for static stability of a legged system is that the vertical projection of the center of mass (CoM) must fall within the base of support (BoS) (SHUMWAY-COOK; WOOLLACOTT, 1995; WINTER, 1995). However, this condition is insufficient in dynamic situations (PAI; PATTON, 1997; IQBAL; PAI, 2000). Seeking to create a stability condition for dynamic situations, Hof, Gazendam, and Sinke (2005) also started from a planar inverted pendulum model, as shown in Figure 13. The natural frequency $\omega_0 = \sqrt{g/l}$ is defined to create the metric, given by $x_0 + {}^{v_0}/_{\omega_0}$. This brings dynamics to the original static stability condition, meaning that the actual projection x_0 of the center of mass added to a fraction of the center of mass' translational velocity must stay inside the base of support. This is mathematically given by:

Figure 13 – Planar model for biped stability, highlighting the center of mass (CoM), center of pressure (CoP) and base of support (BoS), this last one roughly equal to the footsole.

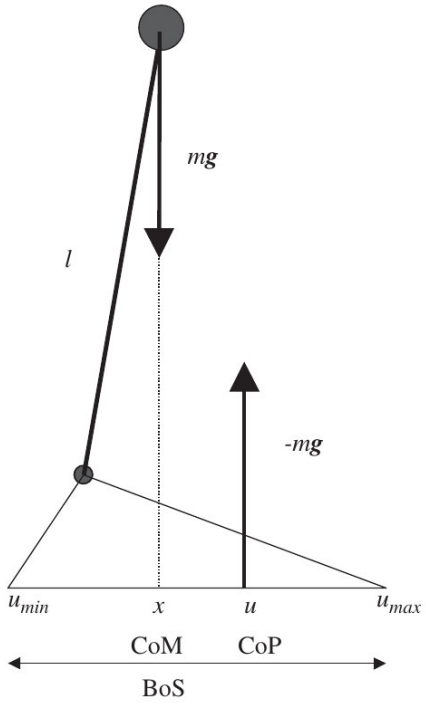

Source: Hof, Gazendam, and Sinke (2005)

$$x_0 + \frac{v_0}{\omega_0} \leq u \tag{2.5}$$

As bipeds are able to shift the center of pressure (CoP) by means of muscle action (WINTER, 1995), u in the last expression can be theoretically moved freely inside the range $[u_{min}, u_{max}]$. This, combined with Equation (2.5), enables the definition of a dynamic stability metric b:

$$b = |u_{max} - (x + {}^{v}/_{\omega_0})| \tag{2.6}$$

All of the previous definitions can be extended to the two-dimensional case, for a biped walking over a surface. There, the b metric is computed as the shortest distance between $\vec{r} + {}^{\vec{v}}/_{\omega_0}$ and the boundary of the base of support (convex polygon around feet). Another important definition is the effective pendulum length l required to compute ω_0. When moving on the sagittal plane, data collected by Winter (2009) and the model proposed by Geurtsen et al. (1975) predicts l between 1.20 and 1.24 times the throchanteric height, which is the distance between the highest point of the greater trochanter and the lowest point of the medial condyle (PANDYA; KHIMA; TULSHI, 2016), both part of the

femur (Figure 14). For movements on the frontal plane, l is given by 1.34 times the same throcanteric height (MASSEN; KODDE, 1979).

Figure 14 – Measurement of throcanteric length.

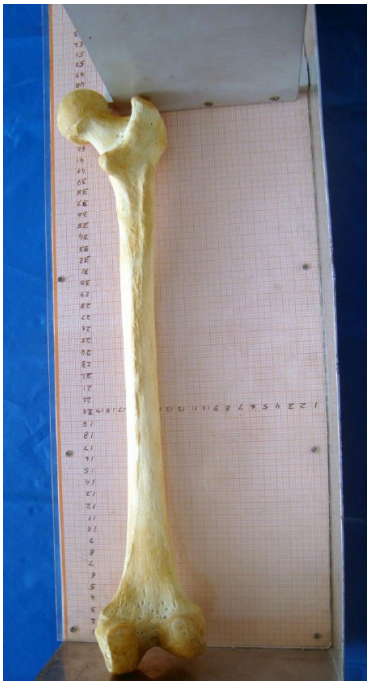

Source: Pandya, Khima, and Tulshi (2016)

That being said, Hof, Bockel, et al. (2007) studied the dynamics of human walking, a movement that can be interpreted as a continuous fall to either side, controlled by the exact timing of foot placement. The Extrapolated Center of Mass (XCoM) was used to analyze lateral motions, with above-knee amputee subjects and a control group of non-amputees. Stable walking, as stated, is achieved through precise foot placement and some ankle strategy for non-amputee subjects, while amputees showed temporal asymmetry in gait due to the structure of the prosthesis (leg prostheses often lack ankle motion control).

From the inverted pendulum model and the definition of the Extrapolated Center of Mass (XCoM), two important properties of stable gait are defined (HOF, 2008):

- *Property 1:* a sufficient condition for stability of the CoM trajectory is that the XCoM trajectory is stable;
- *Property 2:* at any point the tangent to the trajectory of the XCoM runs through the CoP.

Thus, for constant position of the CoP during each step, the trajectory of the XCoM consists of several straight line segments, similar to a triangular wave. Thus, the CoP position and the step time can be controlled as a function of the XCoM position. Figure 15 shows the trajectories of these key points during gait.

Figure 15 – Theoretical trajectories of CoP, XCoM and CoM for a walking motion.

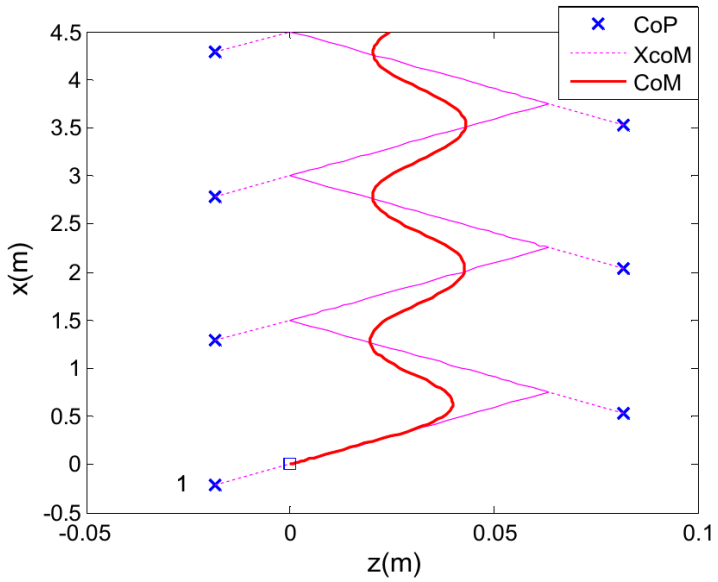

Source: Hof (2008)

The control laws proposed by Hof (2008) are summarized as follows, starting with forward motion control:

$$T_n = \frac{1}{\omega_0} ln\left(\frac{s}{\xi_n - u_{xn}} + 1\right) \tag{2.7}$$

$$u_{xn} = \xi_n - b_x \tag{2.8}$$

$$b_x = \frac{s_c}{e^{\omega_0 T_c} - 1} \tag{2.9}$$

In which:

- T_n: step time;
- ω_0: natural frequency, $\omega_0 = \sqrt{g/l}$;
- s: step length (assumed constant);
- ξ_n: XCoM position;
- u_{xn}: forward CoP position (step location);
- b_x: forward offset.

For lateral control, the computations are analogous:

$$u_{zn} = \xi_n + (-1)^n b_z \tag{2.10}$$

$$b_z = \frac{w_c}{e_{\omega_0 T_c} + 1} \tag{2.11}$$

In which:

- u_{zn}: lateral CoP position (step location);
- ξ_n: XCoM position;
- b_z: lateral offset;
- w_c: desired stride width.

However, when subject to a lateral perturbation, the previous expressions result in a trajectory with steady-state error, which can be dangerous if the subject is walking over a narrow pathway. This is remedied with the addition of proportional control, as in the following expressions:

$$u_{zn} = \xi_n + (-1)^n b_z + k_1(\xi_n - x_c) \tag{2.12}$$

$$w = b_z \frac{e^{\omega_0 T_c} + 1}{1 - \frac{k_1}{2}(e^{\omega_0 T_c} - 1)} \tag{2.13}$$

In which:

- k_1: lateral proportional gain, $0 \leq k_1 < {}^{2}/_{e^{\omega_0 T_c} - 1}$
- x_c: *middle of the road* setpoint.

The subject may also perform turns by rotating the lateral offsets over an angle. For a 2D motion, this is simply done with a two-by-two rotation matrix:

$$\begin{pmatrix} u_x \\ u_z \end{pmatrix} = \begin{bmatrix} \cos(\phi) & \sin(\phi) \\ -\sin(\phi) & \cos(\phi) \end{bmatrix} \begin{pmatrix} -b_x \\ (-1)^n b_z \end{pmatrix} \tag{2.14}$$

As a result, the Extrapolated Center of Mass (XCoM) can be used both as a stability index and as a stepping motion planner. These were the key concepts used by Vallery, Bögel, Riener, et al. (2012) when developing the feedforward balance assistance controller, mentioned at the beginning of this section.

Before moving to the next method, remark: XCoM and Capture Point (previous subsection) theories, which are visibly similar, were independently proposed (KOOLEN et al., 2012). While Pratt and Tedrake (2006), Pratt, Carff, et al. (2006), and Koolen et al. (2012) focused mainly on robotics, Hof, Gazendam, and Sinke (2005), Hof, Bockel, et al. (2007), and Hof (2008) had a greater emphasis on human biomechanics. Nonetheless, both theories are equally relevant regarding the objective of dynamic legged stability assessment and control.

2.7.4 Time to Contact

The concept of Time to Contact was first explored by the astrophysicist Hoyle (1961), being then used by Lee (1976) to introduce the *tau* function, mathematically described as a coordinate divided by its temporal rate of change:

$$\tau(x) = \frac{x}{\dot{x}} \tag{2.15}$$

Accordingly, $-\tau(x)$, termed the *tau-margin* (LEE; YOUNG, 1985), estimates the time it would take for the object to reach the destination point, assuming a constant velocity approach (LEE; YOUNG; REWT, 1992). This *tau* metric has been used in the most diverse areas, and Slobounov, Slobounova, and Newell (1997) proposed using an extension of it for posture control analysis. The traditional *tau* function (2.15) is not directly applicable due to biped support motions taking place in a two-dimensional domain, and foot contact is subject to nonzero acceleration. So, authors defined the Virtual Time to Collision (VTC), which is the spatiotemporal proximity of the center of pressure (CoP) to the stability boundary (SLOBOUNOV; SLOBOUNOVA; NEWELL, 1997), defined as the geometric outline of the base created by the person's feet (BARIN, 1992).

The VTC is computed as the time it would take for the CoP to hit the stability boundary with the actual velocity as the initial and the actual acceleration kept constant. Not forgetting that this is a two-dimensional motion, the trajectories can be points (no motion), straight lines (velocity and acceleration vectors aligned), or parabolas (general case). With this computation, VTC becomes very adherent with instinctive biped behaviour, for example:

- VTC decreases with increased oscillatory body speed while standing;
- A reduced BoS, such as one-foot standing, reduces VTC;
- VTC of a human standing up increases instinctively when the CoP approaches the stability boundary.

During the experiments conducted by Slobounov, Slobounova, and Newell (1997), a lower bound of 300 ms was found for the VTC. This may be a safety margin to trigger

active behaviour towards posture recovery. It is also worth noticing the low dimensionality of time to contact information compared to the high number of degrees of freedom of human body dynamics.

Hasson, Van Emmerik, and Caldwell (2008) studied how time to contact information is used as a prediction for stability, enabling a biped to choose whether or not to take a corrective step to maintain balance. The main difference lies on using the time to contact of the CoM instead of the CoP. Regarding only movements in the sagittal plane, time to contact (considering acceleration, as in the previous case) is instantaneously computed by:

$$TtC_{ACC} = \frac{-v \pm \sqrt{v^2 - 2a(p_{max} - p)}}{a} \tag{2.16}$$

In which:

- v: velocity of the center of mass;
- a: acceleration of the center of mass;
- p_{max}: location of the toe or heel markers (stability boundaries);
- p: position of the center of mass.

This work also used the Extrapolated Center of Mass from Hof, Gazendam, and Sinke (2005) (Subsection 2.7.3) to compute a different type of Time to Contact, as follows:

$$TtC_{XCoM} = \left| \frac{p_{max} - XCoM}{v} \right| \tag{2.17}$$

The previous metrics were successful in assessing standing stability; the minimum Time to Contact (TtC_{ACC}) quadratically decreases as the postural challenge gets harder (instability was induced by colliding test subjects with a pendulum). Such metrics are also suitable for being used as thresholds to trigger stepping actions to recover from a more demanding loss of balance.

Next, Forth, Fiedler, and Paloski (2011) aimed at estimating functional limits of stability (LoS) during bipedal stance. The authors stated that Time to Boundary (another name for the Time to Contact technique) often uses the outer edges of the feet as a stability boundary, but this is overestimated as human motor coordination uses a smaller area as its own limit. It was possible to fit an ellipse representing this boundary after experiments with nine subjects, as shown in Figure 16.

Figure 16 – Best-fit CoP ellipse (solid line) and functional stability limit (dotted line), adding twice the standard deviation to both axes of the ellipse.

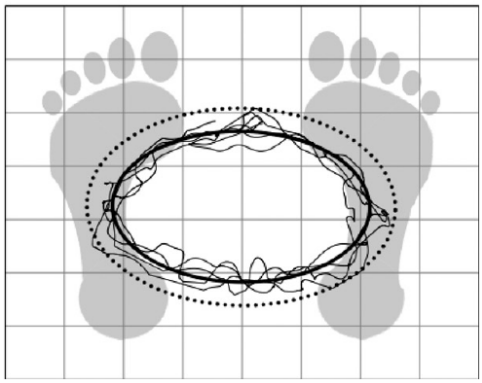

Source: Forth, Fiedler, and Paloski (2011)

2.7.5 Extended Stability Index

Apart from computing a Stability Index in situations of fixed base of support, an Extended Stability Index that includes a varying base was developed by BALANCE (2015). Base of support, in this case, is computed as the convex hull around the feet. This index takes into account a series of previously presented features, such as:

- D_{min}: minimum distance between the vertical projection of the CoM the and edges of the BoS;
- D_{tCv}: distance to the edge of the BoS in the direction of the velocity of the CoM;
- D_{tCa}: distance to the edge of the BoS considering instantaneous acceleration of the CoM;
- T_{tCv}: time to contact between CoM and BoS considering constant velocity;
- T_{tCa}: time to contact between CoM and BoS taking acceleration into account;
- A_{BoS}: total surface area of the BoS.

During simple dynamic situations such as walking and especially during the swing phase, the vertical projection of the CoM often falls outside the BoS, indicating a loss of first level stability. However, the motion itself aims at bringing the swing foot towards a safe placement spot, which is indeed stable. The Extended Stability Index assesses this scenario by creating an extended base of support that adds the projection of the swing foot to the total base of support, as shown in Figure 17.

The definition of an extended base of support brings a better understanding of dynamic activities such as walking, as Figure 18 suggests. The regular Stability Index shows some extreme values due to the constantly changing base of support and a consequently

Figure 17 – Extended base of support (yellow region), comprising the convex hull around support foot and vertical projection of swing foot.

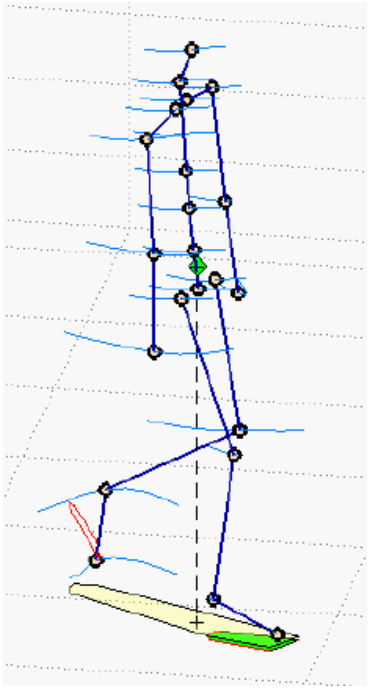

Source: BALANCE (2015)

theoretical loss of balance, whereas the Extended Stability Index helps filter out these values and thus not present false positives related to loss of stability.

2.7.6 Gait Sensitivity Norm and Nearest Neighbor Gait Index

The Gait Sensitivity Norm (GSN) (HOBBELEN; WISSE, 2007) and the Nearest Neighbor Gait Index (NNGI) (GALLEGO et al., 2012) are presented together, as they have a common focus on limit cycle walkers (MCGEER et al., 1990). The Gait Sensitivity Norm starts from defining a generalized system description for a limit cycle walker, with a set of disturbances e as inputs and gait indicators g as outputs. Disturbances can represent, for instance, floor irregularities, sensor noise, or torque ripple, while gait indicators can be step width, step time, or ground clearance at midswing. The system response can be obtained from direct input-output identification, or through a state-space description. The GSN is the H_2 norm of the system. Hobbelen and Wisse (2007) proposes the reciprocal of the GSN as the metric of choice, as a higher value indicates better disturbance rejection. It boasts a fast calculation time and a high correlation (93 % on average) with actual disturbance rejection. Thangal, Talaty, and Balasubramanian (2013) combined the GSN with a neuromusculoskeletal human walking model, supporting the potential of applying this norm to systems more complex than limit cycle walkers.

Next, the Nearest Neighbor Gait Index (GALLEGO et al., 2012) starts by defining a Reference Limit Cycle (RLC), by averaging a series of stable runs. For each time t,

Figure 18 – Indexes computed for straight unperturbed walking.

(a) Stability index values.

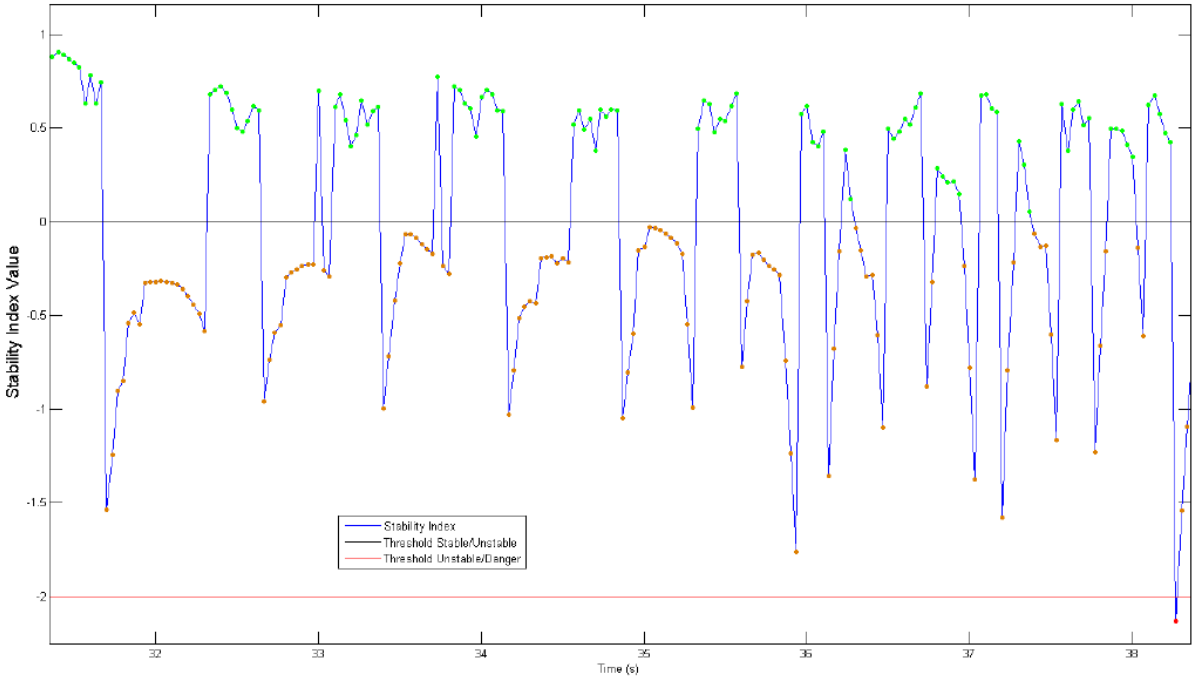

(b) Extended stability index values.

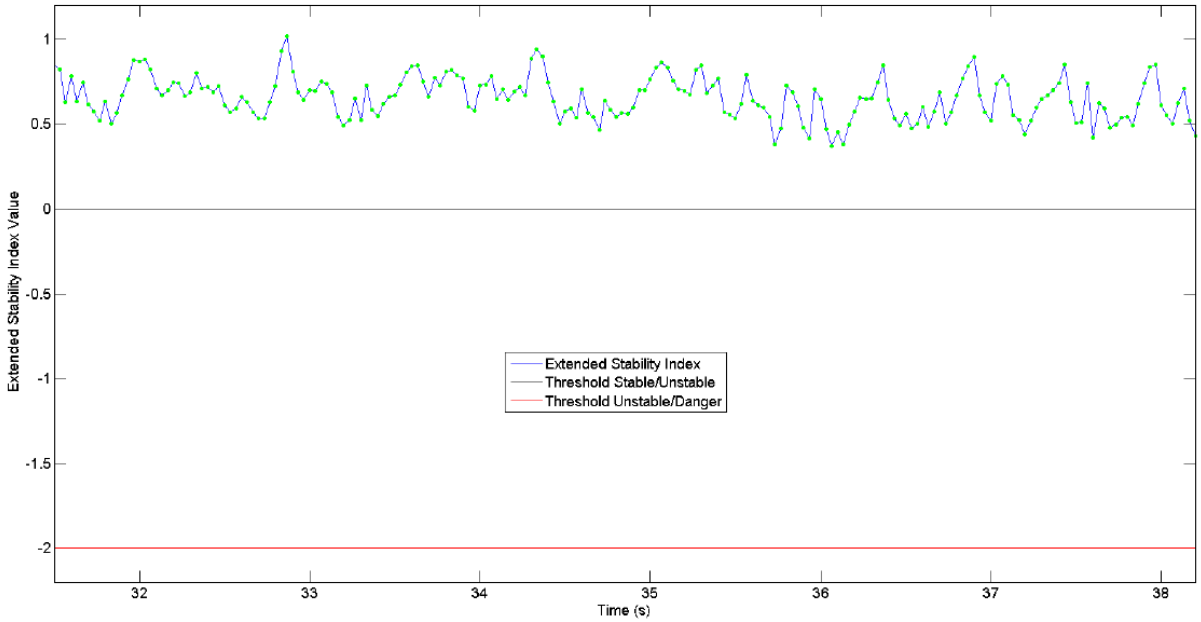

Source: BALANCE (2015)

an Ensemble of Candidate Neighbors (ECN) is defined as a set of m points around the expected state at time t. As limit cycle walking is nominally periodic, an unperturbed robot will have its state always within the ECN. The number m of states must be tuned, as a too large set fails to detect perturbations, while a too small one is prone to output false positives. Then, a nearest neighbor search constantly finds the state $\hat{q}(k)$ inside the ECN that best matches the current state $q(k)$ of the biped. The distance between $\hat{q}(k)$ and $q(k)$ is computed with the D-statistic (KARSSEN; WISSE, 2009), with high values representing a perturbation. However, apart from that, the method can provide a lienarized measurement of the dynamic stability of a walker.

3 MECHANICAL EXOSKELETON DESIGN

This chapter aims at explaining the key aspects related to the ergonomic design of a wearable robot, focusing on the lower limbs. Perhaps the most important principles are the ones from Schiele and Helm (2006), recalled here: wearable exoskeleton (not end-point based), no more than 6 DoFs between consecutive attachments, and kinematically inequivalent to the human. A wearable exoskeleton is composed by an attachment for each limb section of the human, with joints connecting these attachments together.

The following sections will present bibliographic data about this topic, together with experimental designs focused on different joints and underlying principles. Afterwards, general conclusions are drawn from the observed results.

3.1 Ankle joint: a 6-DoF parallel mechanism

The ankle joint is responsible for connecting the lower leg to the foot (MOORE; AGUR; DALLEY, 2018). Ankle motions that move the center of pressure along the base of support, known as *ankle strategy*, configure an important instinctive behavior that favours postural stability, together with the *hip strategy* (HORAK; NASHNER, 1986; KUO; ZAJAC, 1993). So, apart from the two major motions of the ankle - dorsiflexion and plantarflexion -, an external joint must allow its user to exert authority over the other minor ones (see Section 2.3) and thus have full control of the natural motion of the ankle, recalling the concept of *transparency*.

Among the three main joints of the lower extremity (hip, knee, and ankle), the ankle, being the one closest to the ground, is responsible for supporting almost the whole weight of the individual. As it is common to have only one foot in contact with the ground (one-foot standing, walking, running), this joint needs to be stiff and strong. Furthermore, this is the joint with the greatest power and moment requirements during gait (see Figure 19), although having the smallest angular range of motion compared to the other two (FAN; YIN, 2009). In fact, half of the positive joint work is done by the ankle during push-off (WINTER, 1983).

Due to the power preponderance of the ankle joint during walking, several exoskeletons that focus at assisting ankle plantarflexion are successful in reducing metabolic power. Through plantarflexion assistance with pneumatic muscles, it is possible to achieve a reduction between 6 % and 17 % in metabolic power compared to walking with an equivalent unpowered exoskeleton (NORRIS et al., 2007; SAWICKI; FERRIS, 2008, 2009a,b; GALLE et al., 2013; MALCOLM; DERAVE, et al., 2013). Loaded walking was studied by Galle et al. (2014), where an exosuit with pneumatic muscles was effective at boosting

Figure 19 – Lower limb joints moment and power during a whole gait cycle (75 kg person walking at 1.3 m/s).

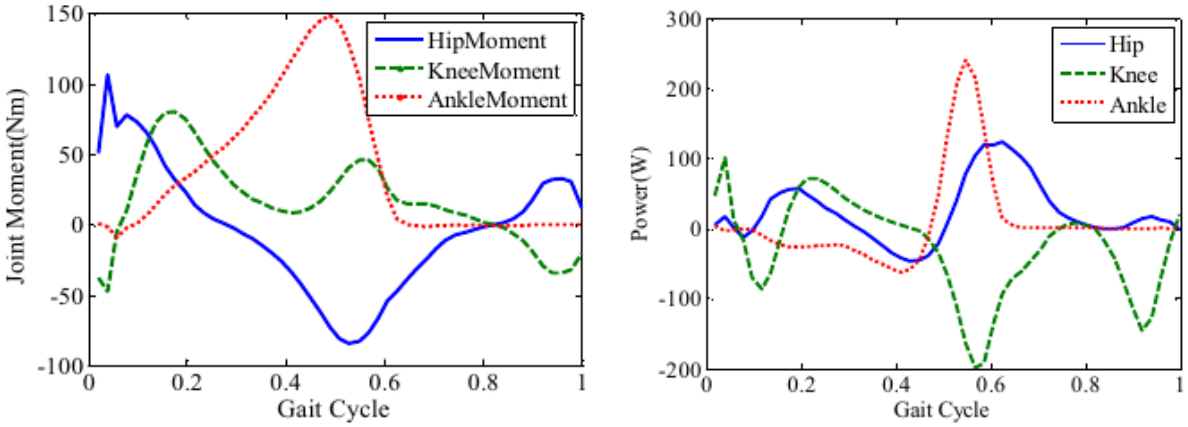

Source: Fan and Yin (2009)

endurance and total weight carried. The same plantarflexion assistance was also made possible using bowden cable actuation, with the same result of metabolic rate reduction (GRIMMER et al., 2017; MALCOLM; LEE, et al., 2017; BAKER et al., 2017). The previous exoskeletons are not autonomous, requiring an external compressed air supply or bowden cable drive mechanism, what could make their efficiency questionable, but Mooney, Rouse, and Herr (2014) created an autonomous ankle exoskeleton that reduced the metabolic cost of walking by 8 % compared to walking without using the exoskeleton.

As a result, it is of central importance that the designed ankle joint is efficient at applying forces that directly assist ankle plantarflexion. Many of the previous examples regarded soft exoskeletons that do not have joints in fact, but mimic the user's muscular actuation. The present work focuses on a *hard* joint, due to its structural advantages, that allows offloading of the exoskeleton weight and additional loads to the ground.

3.1.1 Related work

A parallel mechanism with three degrees of freedom was used for designing an ankle joint by Fan and Yin (2009), due to its better rigidity and compactness compared to serial mechanisms. The authors of that paper had a similar focus on not compromising natural human motion. The basic model of the mechanism is reproduced at Figure 20. The authors then used a multiobjective optimization to select the dimensions of the mechanism, resulting in the design shown in Figure 21. The present work aims at enabling an even broader range of motion, unachievable with a 3-DoF platform.

3.1.2 The mechanism

To define the required number of degrees of freedom of the proposed mechanism, the first step is to list the necessary motions:

Figure 20 – Model of the 3-DoF parallel mechanism for the ankle.

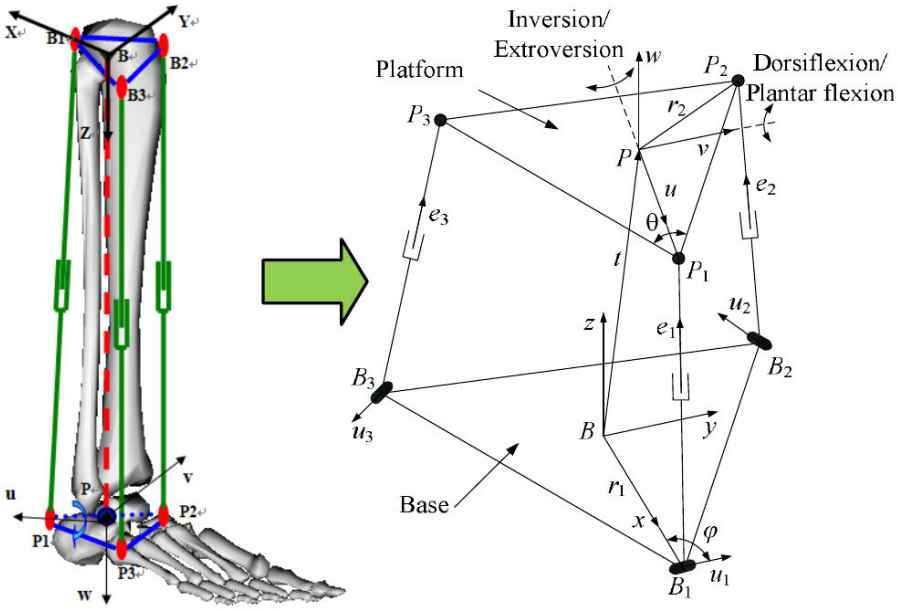

Source: Fan and Yin (2009)

Figure 21 – 3-DoF parallel ankle after design optimization.

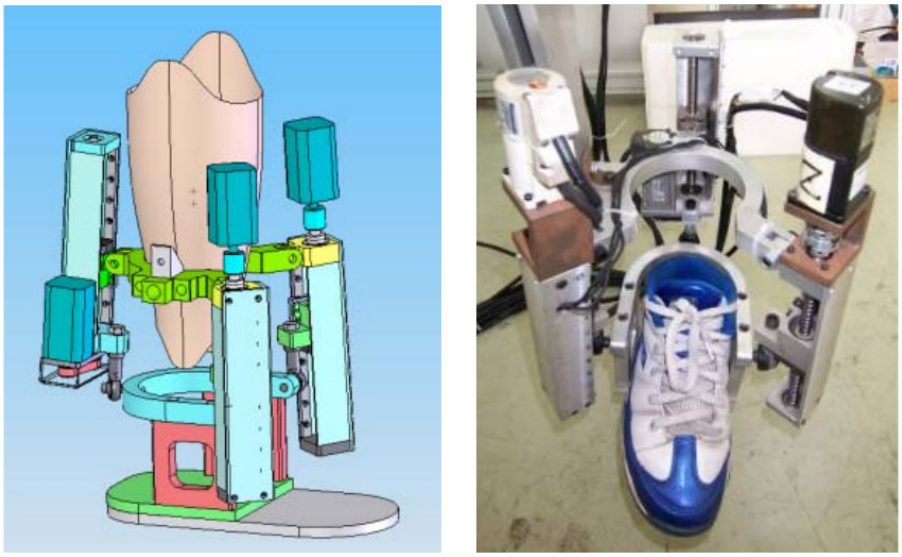

Source: Fan and Yin (2009)

- *Position* the virtual center of the joint at the point corresponding to the ankle of the human. The position can vary between users in all three dimensions, so three degrees of freedom are required here;
- *Rotate* the ankle in the two anatomical movement sets: dorsiflexion-plantarflexion and eversion-inversion. Therefore, two more DoFs are demanded.

As a result, the mechanism requires a minimum of five degrees of freedom. The overall concept will be based on previous works of Stewart (1965) and Gough (1957, 1962). Whilst becoming more popular after Stewart's publication (STEWART, 1965), Gough's tyre testing machine (GOUGH, 1962) was probably the first device based on what it is presently known as a Stewart platform. Gough's design, shown in Figure 22, is often applied in areas a lot different than wearable robots, such as flight simulation systems. Stewart's approach, on the other hand, was less specific, stating that the platform can be conceived from any combination of six actuated joints.

Figure 22 – Gough's tyre testing machine.

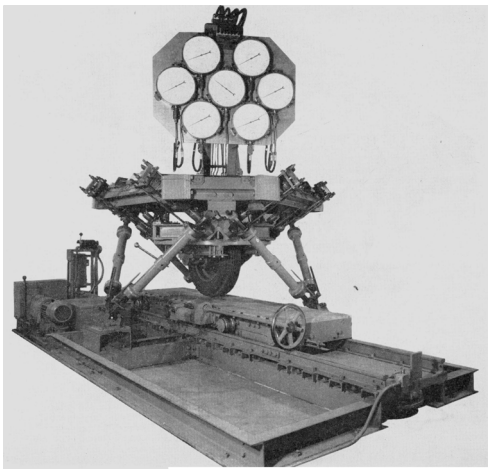

Source: Stewart (1965)

To be applied in the present work, it is necessary to consider the lower leg as the ground point of the Stewart platform, with the sole of the human foot being the platform itself. Additionally, the platform always considers a total of six degrees of freedom; a 5-DoF version can be obtained by locking one of the actuated links, however this ends up decreasing the mechanism dexterity. As a result, the ankle joint will be designed with all six degrees of freedom of the original Stewart platform.

3.1.3 Design

The concept phase of the design begins with connecting the actuators between the two main anchor points of this joint: the lower leg and the foot. One extremity of the actuators receives a universal (2-DoF) joint, whilst the other one has a spherical

(3-DoF) joint. Spherical joints at both extremities are also allowed; while not necessary, the additional DoF represents rotation around the actuator's own axis and is not detrimental.

The points of connection between the leg and the actuators must lie at the posterior part of the lower leg, allowing the user to put on the exoskeleton from the front, enhancing the important aspect of user friendliness (ROCON; RUIZ, et al., 2005). Figure 23 shows the most important elements of the concept. It is also worth noticing that one of the six actuators is vertically aligned with the heel, being the key one in plantarflexion assistance.

Figure 23 – Initial concept of the 6-DoF parallel linkage for the ankle joint.

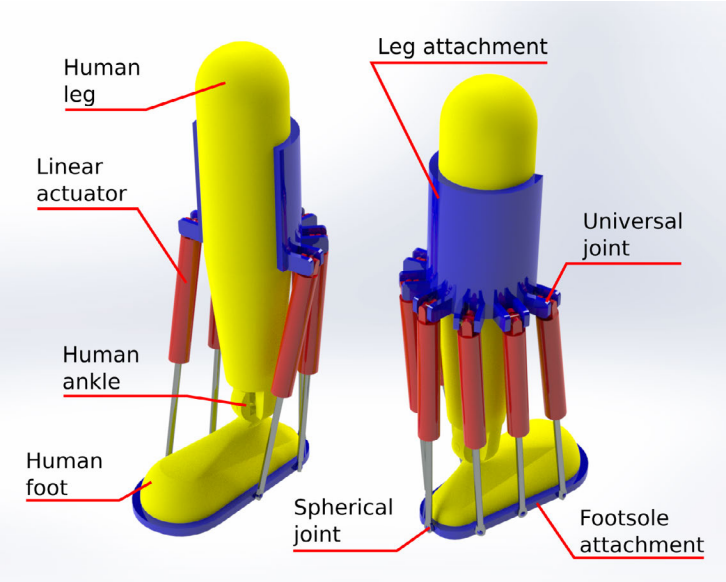

Source: authored

3.1.3.1 Kinematic optimization

After defining the concept and how the mechanism should look like, it is clear that the locations of the joints of each actuator are not fully defined. Some constraints, like the spherical joints lying on the same plane of the foot sole and one of the actuators aligned with the heel, are well-posed, but there still is plenty of freedom on the design as a whole. This brings room for an optimization algorithm, allowing for the best placement of each actuator according to a specific metric.

To make this possible, the concept shown in Figure 23 was first translated to a physics simulation environment, *Simscape Multibody*[1] from *MATLAB*, version R2019b. There, the human leg and foot are represented from simple solids, and the mechanism is built with cylinders. *Simscape Multibody* has many types of joints built in, such as universal, spherical, and prismatic joints (all used in this work). There also is a relevant feature for detecting spatial contact, as the actuators must not touch the user's body while performing the natural motions of the ankle. Last, *MATLAB* allows for seamless

[1] Available from: https://www.mathworks.com/products/simmechanics.html

integration of the physics simulation - with multiple simulations running in parallel - and the optimization algorithm.

As the goal of the mechanism is to allow the user to perform the whole natural range of that joint, the angles described in section 2.3 were passed to the universal joint that represents the human ankle by means of two sinusoidal waves:

- *Dorsiflexion/Plantarflexion:* from -20° to 50°, at 1.0 Hz;
- *Eversion/Inversion:* from -20° to 35°, at 0.75 Hz.

The previous nonmatching frequencies aim at combining different points of each rotation trajectory during the five total seconds of simulation. The optimization technique of choice was a genetic algorithm (MITCHELL, 1998), containing crossover and mutation, performed sequentially for each actuator, starting from the heel and working towards the toes. Appendix A has a detailed explanation of the overall functioning of genetic algorithm optimization. Each actuator is represented by a population of 40 individuals, each one containing four parameters referring to the polar (radial and angular) placement of each joint. See Figure 24 for clarification. The joints are allowed to come no closer than 30 degrees and no farther than 60 from one another.

As stated before, one goal of this joint is to fit a range of body structures. Thus, the optimization was carried out for two extreme leg and foot sizes, representing a tall (2 m) and a short (1.5 m) person, and one average height (1.75 m tall). Proportions between total height and leg and foot lengths are derived from the Golden Ratio (ϕ) and the Vitruvian Man (ABU-TAIEH, 2015).

- Total body height: $H_T = [1.5, 1.75, 2]$;
- Lower leg length: $L_L = \frac{H_T}{4}$;
- Leg radius: $R_L = \frac{\phi}{1+\phi} \cdot \frac{L_L}{4}$;
- Foot height (from sole to ankle): $H_F = \frac{L_L}{(1+\phi)^2}$

The cost function to be optimized comprises the sum of the distance of each joint end to the leg axis, i.e., their radii, the total motion amplitude of each linear guide, and a penalty ($1 \cdot 10^6$) for collision between the mechanism and leg or foot. After executing the optimization, parameters are obtained for each total height, summarized at Tables 1 and 2, together with each corresponding standard deviation. Analyzing the results, there is a clear tendency of the joints moving away from the leg as the total height increases, however

Figure 24 – Schematics showing the radial positioning of the actuators around the heel.

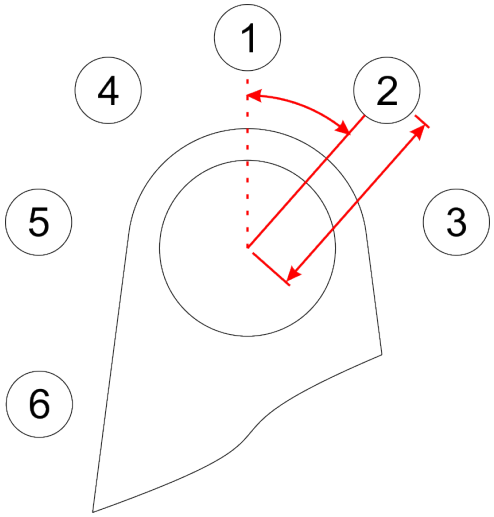

Source: authored

the angles experience little variation. This indicates that joint angular positions have a small dependency on body structure, relating almost solely on the motions performed by the ankle joint. Another important result concerns the total displacement of each linear actuator, summarized at Table 3; notice that the tallest subject provides the maximum amplitude for all actuators.

Table 1 – Optimized parameters for leg joint placement, with radii in mm and angles in radians [authored].

	Height	**1.5 m**	**1.75 m**	**2.0 m**	**Std. dev.**
Actuator 1	Radius	54,374	63,956	77,747	11,749
	Angle	0,000	0,000	0,000	0,000
Actuator 2	Radius	74,770	79,306	74,691	2,642
	Angle	-0,561	-0,797	-1,010	0,225
Actuator 3	Radius	57,122	63,600	80,949	12,320
	Angle	-1,301	-1,797	-1,652	0,255
Actuator 4	Radius	67,016	69,551	67,887	1,288
	Angle	0,883	0,575	0,725	0,154
Actuator 5	Radius	50,263	56,765	70,631	10,404
	Angle	1,522	1,248	1,494	0,151
Actuator 6	Radius	69,091	68,348	69,496	0,582
	Angle	2,170	2,163	2,070	0,056

Table 2 – Optimized parameters for foot joint placement, with radii in mm and angles in radians [authored].

	Height	**1.5 m**	**1.75 m**	**2.0 m**	**Std. dev.**
Actuator 1	Radius	47,201	59,938	64,412	8,930
	Angle	0,000	0,000	0,000	0,000
Actuator 2	Radius	50,689	55,200	66,755	8,286
	Angle	-0,795	-0,957	-0,757	0,106
Actuator 3	Radius	52,033	64,132	64,983	7,244
	Angle	-1,412	-1,917	-1,745	0,257
Actuator 4	Radius	56,800	57,256	75,797	10,839
	Angle	0,792	0,529	0,548	0,147
Actuator 5	Radius	63,692	80,461	82,003	10,156
	Angle	1,420	1,442	1,470	0,025
Actuator 6	Radius	64,459	82,133	94,021	14,875
	Angle	2,161	1,991	2,163	0,099

Table 3 – Total displacement for each actuator (optimized parameters) [authored].

Act. disp.	**1.5 m**	**1.75 m**	**2.0 m**
Actuator 1	93,7	128,4	168,3
Actuator 2	104,4	135	174,5
Actuator 3	89,1	128,8	168,6
Actuator 4	111,9	141,8	180,6
Actuator 5	107,3	146,2	185,2
Actuator 6	120,7	158,1	195,8

3.1.3.2 Final design

To design each mechanical part of the prototype, optimization results were taken for each individual joint (2 for each actuator, 12 total) as the *maximum* radius (rounded up to the nearest integer, in mm) and the *average* angle (rounded to the nearest integer, in degrees). The total motion range of the actuators is related to the maximum values of Table 3 with around 5 additional millimeters as follows:

- Actuator 1: 175 mm
- Actuator 2: 180 mm
- Actuator 3: 175 mm
- Actuator 4: 185 mm
- Actuator 5: 190 mm
- Actuator 6: 200 mm

With the previously explained parameters and observance of manufacturing and assembly principles, the CAD prototype was designed as shown in Figure 25. It features

Figure 25 – Final CAD design of the parallel ankle joint prototype.

Source: authored

an articulated band with a ratchet fixture for the leg and an adjustable foot sole, with slots for insertion of fabric bands. This design, more detailed than the one created under *Simscape Multibody*, was again checked for collisions between actuators and leg or foot and for reaching any end stops within every linear actuator. There were no issues found.

3.1.4 Manufacturing and assembly

Aiming to assess real-world commitment of the prototype to the proposed objectives, the previously shown CAD prototype was translated into reality in 1:1 scale, allowing it to be later on attached to test subjects. It was mainly made out of commercial mechanical components, 3D printed ABS parts, and machined components. The leg fixture is composed by an articulated band that is also responsible for ensuring the correct positioning of each linear actuator. It is held in place with a rather uncommon fixture system regarding the field of wearable robots: a ratcheting mechanism. This is also an early proposal, coming from the belief that it is superior to the more widely used adhesive fabric straps. The band interior is partially covered with nonslip material to ensure enough grip without needing to over-compress the user's leg. Figure 26 shows a picture of the leg band.

The whole mechanism is completed by connecting the leg and foot fixtures with the linear guides, containing spherical joints at both ends. The complete assembly is shown in Figure 27. It is worth mentioning that mounting the system to the leg is very simple, performed with ease by the user alone. The articulated leg band clamps the lower leg at calf height from behind and stays firmly in place. The correct alignment, with the rearmost linear actuator oriented vertically, is also straightforward.

Figure 26 – Fixture band for the leg, with ratchet mechanism in pink.

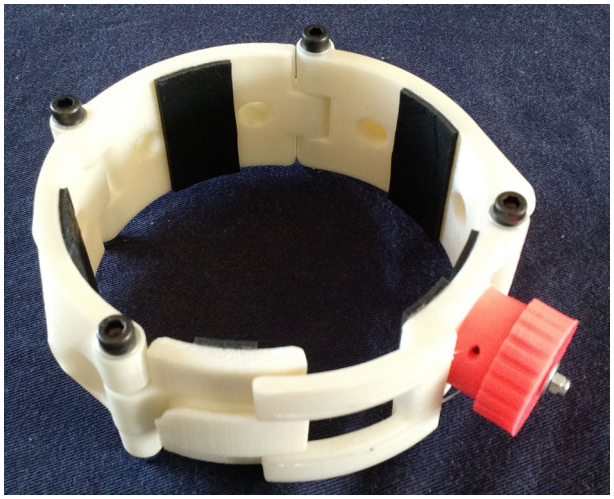

Source: authored

Figure 27 – Completely assembled prototype attached to a test subject's leg and foot.

Source: authored

3.1.5 Kinematic testing and assessment

Experiments are now performed on the system shown in Figure 27. The ankle joint exoskeleton must be attached to the subject's leg at calf height, with the rearmost linear joint (Actuator 1 of Figure 24) vertically aligned with the subject's heel. The foot attachment can have its length adjusted to match the foot size, holding it in place with two adhesive straps. After firmly attaching the ankle joint exoskeleton to the subjects' leg and foot, they are asked to perform the maximum range of dorsiflexion, plantarflexion, eversion and inversion, checking whether the system is preventing them from completing any movement or the linear guides are coming into contact with their body. An example result is shown in Figure 27. No spurious contacts between the exoskeleton and the human body

were reported, however subjects reported difficulties in performing both plantarflexion and inversion. A closer analysis showed that the issue was directly related to the limited angular range of the commercial spherical rod ends connecting the actuators with the foot sole.

Figure 28 – Test subject performing the four anatomical ankle motions. From left to right: dorsiflexion, plantarflexion, eversion and inversion.

Source: authored

3.1.6 Improved joints and final testing

After the previously reported problems with the limited range of spherical joints, a custom universal joint with a larger range of angular motion was designed. Its manufacturing was made possible by 3D printing, with the interesting feature of the joint printed already assembled, and unable to be taken apart - a *print-in-place* design. Figure 29 shows the previously used spherical joints and the custom 3D printed universal joint. It must be made clear that, although universal joints have one less degree of freedom than spherical joints, this is not an issue to the overall design, as this corresponds to the rotation around the actuator's own axis and is already addressed by the upper spherical rod end. In other words, it is a redundant degree of freedom, as already mentioned in Subsection 3.1.3.

After attaching universal joints to all six corresponding spots, the whole mechanism was rebuilt. Figure 30 shows a detail picture focusing on the foot attachment, where the newly added universal joints appear in yellowish white. Testing was again conducted in the same manner, with the subjects performing the whole range of anatomical ankle motions, on all directions. Collisions were again non-existent, whilst the whole motion range was now performed without any issues. See Figure 31 for a picture of the results. Visual comparison with the previous scenario (Figure 28) shows how the new joints positively affected the total motion amplitude.

Figure 29 – Custom universal joint (left) side by side with the commercial spherical rod ends (right), connected to the lower extremity of the linear actuators.

Source: authored

Figure 30 – Complete prototype with spherical rod ends replaced by custom universal joints.

Source: authored

Figure 31 – Four anatomical motions performed with universal joints installed. From left to right: dorsiflexion, plantarflexion, eversion and inversion.

Source: authored

The tests covered a total of three individuals[2]: 1.81 m male, 1.77 m male and 1.72 m female. They all reported being able to perform the whole allowable range of their ankle joints, without any interference or contact caused by the external device. The resulting design is also very easy to wear and remove, an operation that can be done by the user alone.

3.1.7 Results and discussion

Recalling the principle of Section 3.1, the goal of this joint design was to allow for the whole range of natural human ankle motion, while fitting a range of different body structures without requiring any mechanical adjustments. All this objectives were fully achieved in simulation and confirmed in experiments with real hardware. The proposed design is also easy to be put on and removed.

While the joint concept allowed test subjects to move their ankles without any interference from the mechanism, the rigid foot sole used brought on some strangeness, feeling like wearing a wooden sole clog. This stresses the importance of having flexible foot attachments in exoskeletons, maintaining user's ability to deform the arches of the foot. This type of flexible attachment might resemble a sneaker, offering added comfort and enabling activities such as prolonged gait.

Another positive aspect of this joint design is that the parallel linkage occupies a rather thin region of space around each leg, thus not demanding users to adopt an unnatural walking behavior, with their feet wide apart. This compactness may be improved by removing the restriction that all lower actuator attachments (universal joints) must lie on the foot sole, enabling the optimizer to move them freely in the 3D space around the ankle.

The proposed exoskeleton joint, with a total of 6 DoFs, has clear ergonomic advantages. However, it may raise a question about costs, as it requires, at first glance, six actuators for a single ankle. This may be a worth investment in some, but not all, applications. However, this is also a flexible aspect of this design: the modularity presented by the six individual linear joints enables them to be diverse. A prolonged walk scenario, that benefits mostly from plantarflexion assistance, may be addressed by powering just the rearmost joints. It is also possible to make some of the linear guides spring-loaded, supporting the ankle around a specific operating point. A specialized application, like physiotherapy or rehabilitation, certainly benefits from full actuation to a valid extent.

To sum up, recalling the initial objectives, the concepts laid by this work are an important step towards more ergonomic and kinematically compatible wearable robots. This ankle joint, still fully passive during this step of the design phase, is capable of

[2] Testing with a broader range of individuals was not possible due to social distancing measures imposed by COVID-19 pandemic circumstances, ongoing at the time this work was developed.

application in several scenarios, in conjunction with the most adequate set and type of actuators, e.g., hydraulic (BOAVENTURA, 2013), electric, or bowden cable (VENEMAN et al., 2006).

3.2 Knee joint: a four-bar biomimetic mechanism

At first glance, the knee may seem a simple joint, with a predominant motion of flexion-extension together with a small amount of medial-lateral rotation (see Section 2.3 for more details). Thus, it is very common to see exoskeletons that include a rotational joint to actuate knee motion (RAKSHIT, 2017); however, it has been found, many years from now, that a single-axis rotational joint is an extremely rough approximation for the human knee (TRENT; WALKER; WOLF, 1976).

Knee orthoses with some kind of articulation are readily available as commercial products for a number of applications, including compensating for abnormal joint mobility or mechanical deficits in patients. They can also serve as protection equipment, helping the joint not to be overstressed, overstretched, or bent laterally (this is seen, for example, in motorcycling, as shown in Figure 32) (CAI et al., 2017). Also, these devices can be worn by patients after undergoing knee surgery (KIM; KANG; CHOI; HAN, et al., 2011), on what is called *continuous passive motion*, which can be less harmful than a traditional immobilization treatment (EVANS et al., 1960). Many orthoses still employ simple-axis hinge joints (see Figure 33a), which are completely prone to misalignment, resulting in pistoning forces between the orthosis and the limb tissues (LEW et al., 1982). The modified motion pattern also influences ligament length patterns, femoral-tibial contact points and meniscal movements (WALKER; ROVICK; ROBERTSON, 1988), which can be of great harm in surgical recovery or prolonged usage scenarios.

Figure 32 – Knee brace used as protection in motocross.

Source: Alpinestars (2021)

Figure 33 – Commercial knee orthoses.

(a) Knee orthosis with a simple-axis hinge joint.

(b) Knee orthosis with polycentric hinges.

Source: Breg (2019) and McDavid (2020)

As a way to address this incompatibility, manufacturers use a special type of joint called a *polycentric hinge*, like the orthosis depicted in Figure 33b. As the name suggests, this type of joint rotates around a nonfixed center, aiming to improve motion compatibility, but this is still a lot far from perfect, specially when the knee makes a high-amplitude flexion (BERTOMEU et al., 2007). Apart from that, some mechanisms utilized, such as pin-in-slot or cam-follower, are hard to manufacture and usually rely on friction between the parts.

As a result, to properly design a knee joint for a transparent exoskeleton, it is important first to mathematically describe the complex motion occurring in the human knee. Next, choose and detail a mechanism that is able to mimic that motion, while being simple and strong, recalling the essential load-bearing characteristics of this joint.

3.2.1 Motion of the human knee

The human knee joint performs the flexion-extension movement with a complex combination of slide and roll, according to the interaction between the joint surfaces of femur and tibia, together with the two cruciate ligaments (OLINSKI et al., 2016) (see Figure 34). The result of this structure is a change in the instantaneous center of rotation (ICR) of the joint with the flexion angle. This change is the main source of incompatibility between the knee and a simple hinge joint, something that polycentric joints such as the one shown in Figure 33b are still unable to address satisfactorily.

Figure 34 – Internal anatomy of the human knee joint.

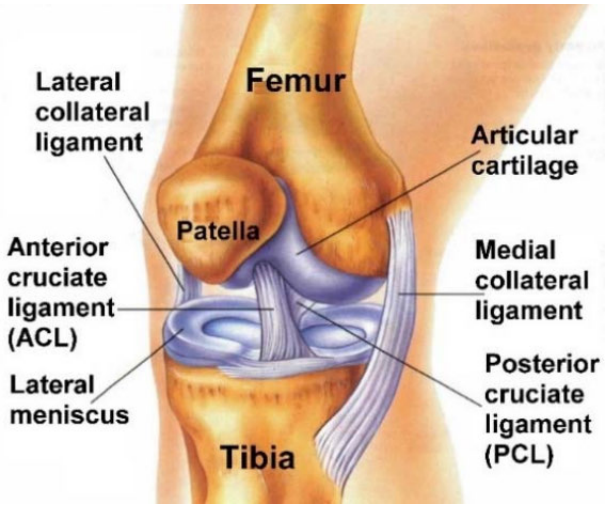

Source: Olinski et al. (2016)

Seeking to quantify the knee motion in three dimensions and thus create a mathematical model to serve as a foundation for external joint design, a thorough work was done by Walker, Kurosawa, et al. (1985) with 14 fresh cadavers and 8 volunteers. One part of the work involved embedding the femurs from the cadavers in plaster and cutting them in a total of 17 sections, from lateral to medial, digitizing them and determining the best-fit surface to represent the femoral articulation. It was possible to accurately describe the articular surfaces using spheres.

Then, the authors accurately measured the motion from cadaveric knees, using afterwards measurements from the volunteers as another source of data. It was possible to average among all knees with relatively low deviation, and then define best-fit quadratic equations for varus rotation (V_R), internal rotation (I_R), anterior-posterior translation (Z_{DIS}) and distal-proximal translation (Y_{DIS}) as a function of flexion angle (F). The equations are as follows, with angles in degrees and displacements in millimeters (WALKER; KUROSAWA, et al., 1985; KUROSAWA et al., 1985):

$$V_R = 0.124F - 0.000913F^2 \tag{3.1}$$

$$I_R = 0.378F - 0.00178F^2 \tag{3.2}$$

$$Y_{DIS} = -0.05125F + 0.000308F^2 \tag{3.3}$$

$$Z_{DIS} = -0.0602F + 0.0000178F^2 \tag{3.4}$$

In a more recent article, Walker, Rovick, and Robertson (1988) fitted higher degree equations for the same description (this time from 23 cadaveric knees), as follows:

$$V_R = 0.0791F - 5.733 \cdot 10^{-4}F^2 - 7.682 \cdot 10^{-6}F^3 + 5.759 \cdot 10^{-8}F^4 \tag{3.5}$$

$$I_R = 0.3695F - 2.958 \cdot 10^{-3}F^2 + 7.666 \cdot 10^{-6}F^3 \tag{3.6}$$

$$Y_{DIS} = -0.0683F + 8.804 \cdot 10^{-4}F^2 - 3.750 \cdot 10^{-6}F^3 \tag{3.7}$$

$$Z_{DIS} = -0.1283F + 4.796 \cdot 10^{-4}F^2 \tag{3.8}$$

The coordinate system for both sets of equations is shown in Figure 35, with the Z axis parallel to the upper surface of the tibia and the Y axis perpendicular to it. The X axis joins the centers of the two femoral spheres (lateral and medial). The origin is at the posterior corner of the tibial surface (WALKER; KUROSAWA, et al., 1985), and the orientation suggests using the right knee as reference.

Figure 35 – Coordinate system for knee motion description.

(a) Sagittal plane view. (b) Three-dimensional view.

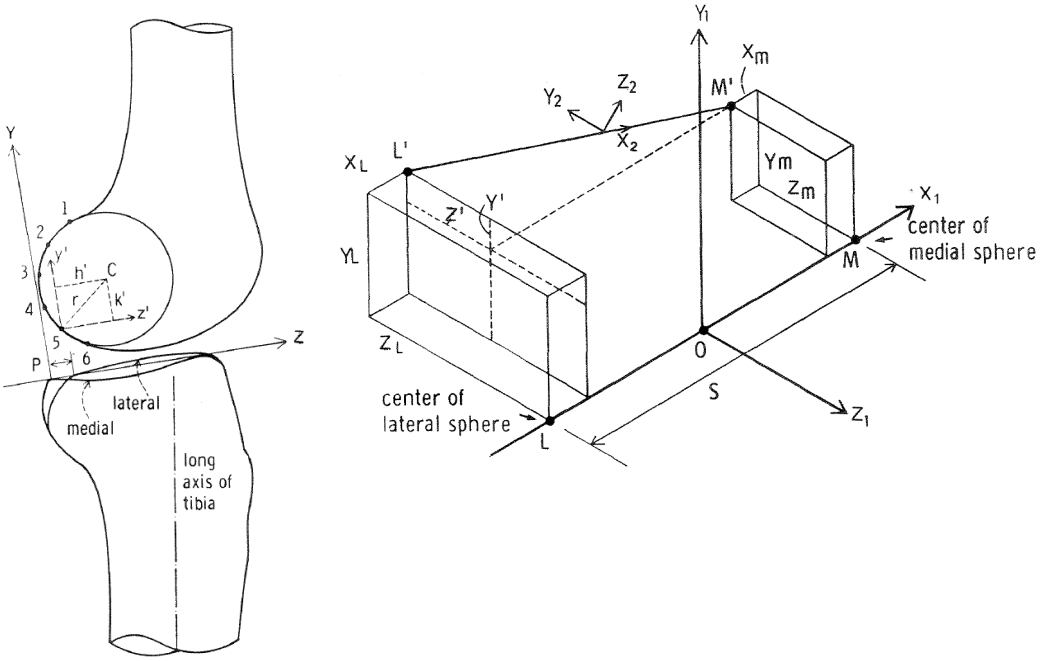

Source: Walker, Kurosawa, et al. (1985)

To design an external joint for the knee, one must define the distance between the joint and the knee center, or the femoral origin. According to the described coordinate system, this is a distance along the X axis. With this defined, it is possible to compute the YZ trajectory of the instantaneous center of rotation (ICR) on that given plane with the following two equations (WALKER; KUROSAWA, et al., 1985):

$$Y = -\sin V_R \cdot X + Y_{DIS} \tag{3.9}$$

$$Z = \cos V_R \cdot \sin I_R \cdot X + Z_{DIS} \tag{3.10}$$

Substituting a motion range of zero (complete extension) up to 120° of flexion in Equations (3.1) to (3.8), it is possible to obtain the translations and rotations that define the knee motion, according to each one of the models. Figure 36 summarizes this data, showing that the two models are not perfectly the same, which may be because of differences between the observed knees, or the way that flexion angle was imposed. However, differences are small in magnitude and inside the internal laxity of the knee joint, which is between 5 and 10 millimeters (anterior-posterior) and between 20 to 30 degrees (total rotational laxity) (WANG; WALKER, 1974; HSIEH; WALKER, 1976; MARKOLF; MENSCH; AMSTUTZ, 1976; MARKOLF; GRAFF-RADFORD; AMSTUTZ, 1978).

Figure 36 – Knee motion during a complete flexion (0 - 120°).

(a) Translational motions. (b) Rotational motions.

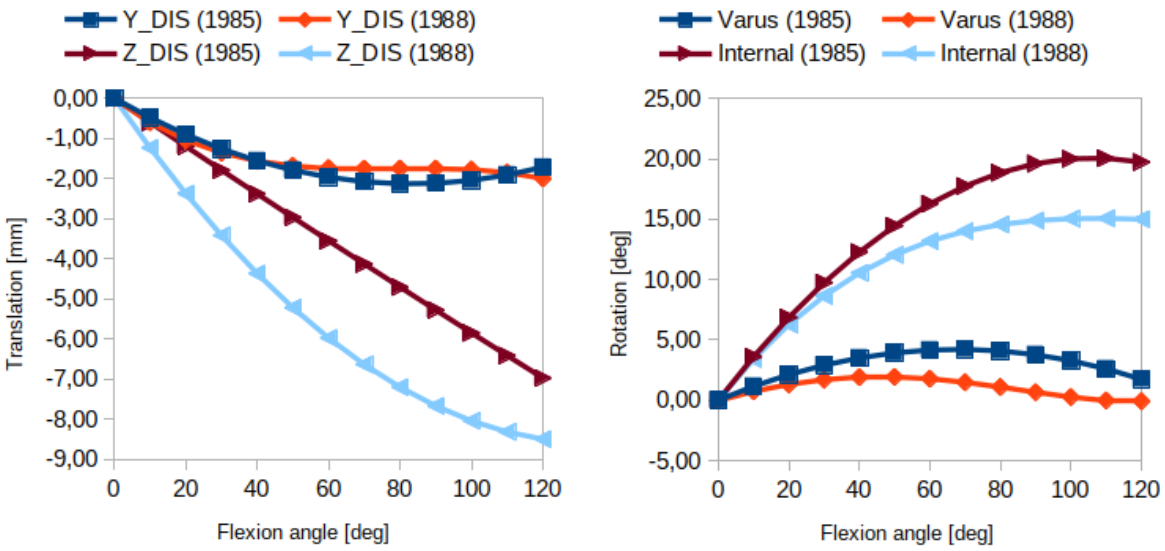

Source: authored

Now, considering exoskeleton design, the joint must be offset in the X axis to a certain amount, for example 60 mm from the femoral origin (WALKER; KUROSAWA, et al., 1985). However, due to varus and internal rotations of the joint, the trajectory on either side of the knee is different (see Figure 37 for clarification). Thus, to design an exoskeleton joint placed outward from the sagittal plane, the value is in fact $X = -60$. Using this value and Equations (3.9) and (3.10), target motion for the exoskeleton joint is computed, as shown in Figure 38. There are small differences between the two fitted models, which are averaged into a third trajectory.

The previously shown computations complete the main objective for an external knee joint design, with a target planar trajectory to be followed. This enables a subsequent design of a joint that respects these natural trajectories that emerge from the particular internal geometry of the human knee.

Figure 37 – Movement of the femoral transverse axis with respect to the tibia. Notice how the behavior on either side of the joint is different.

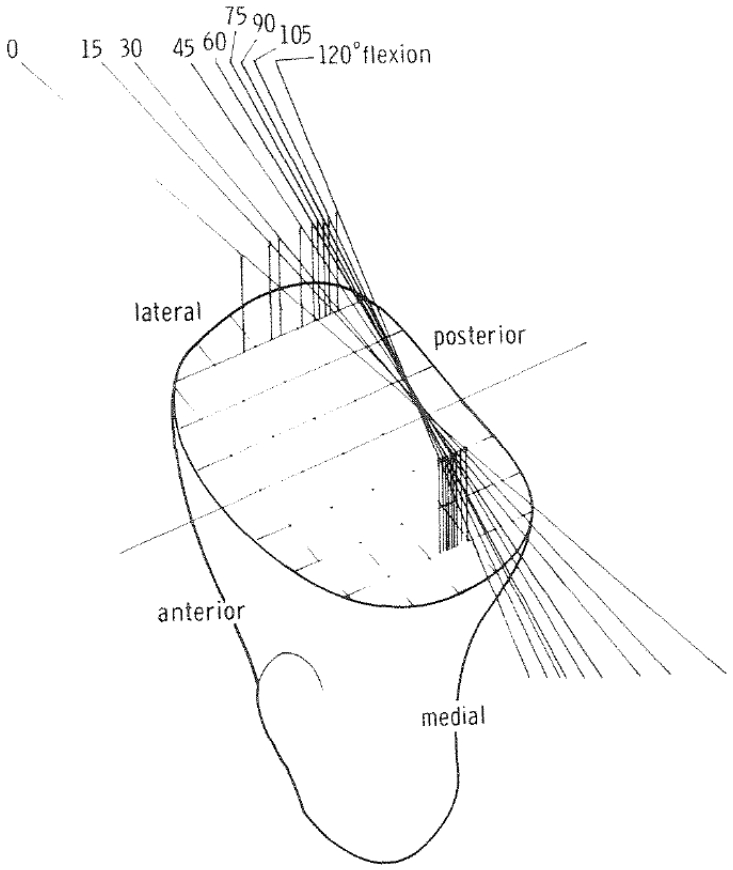

Source: Walker, Kurosawa, et al. (1985)

Figure 38 – Femoral axis translation at $X = -60\ mm$ during a complete flexion (0 - 120°).

(a) Displacements as a function of the flexion angle.

(b) Displacements in YZ coordinates.

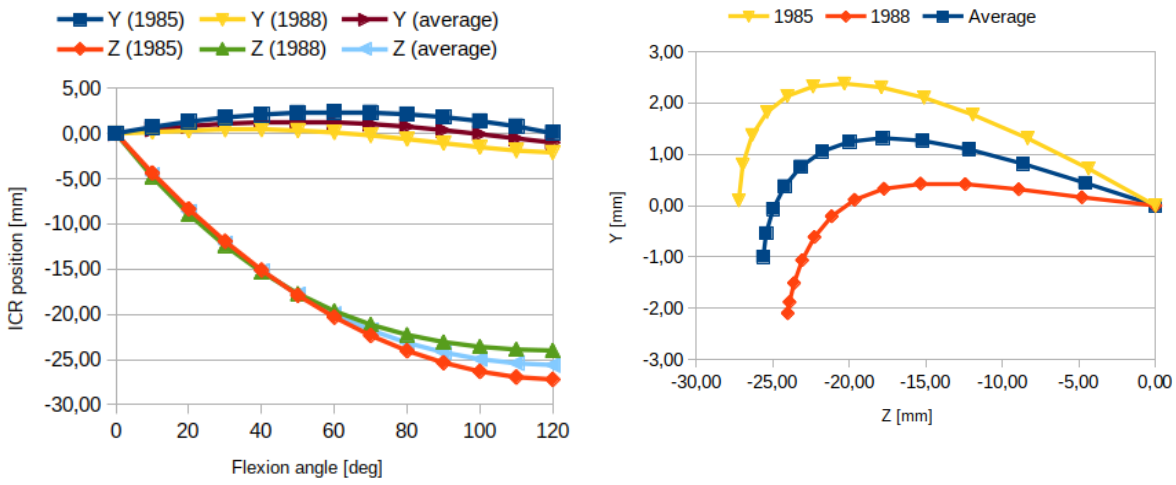

Source: authored

3.2.2 The mechanism

Recalling the concepts of biomimetism and ergonomic design, the human knee is composed by two articular surfaces joined together by two cruciate ligaments (Figure 34). From a sagittal plane view, this configuration is extremely similar to a crossed four-bar linkage (KIM; KANG; CHOI; JANG, et al., 2012), as shown in Figure 39. Thus, an external joint based on the same type of linkage is a strong candidate to be ergonomic and follow the target curves from the previously shown model (Figure 38).

Figure 39 – Simplified view of the knee joint, recalling the similarity between its internal configuration and a four-bar linkage.

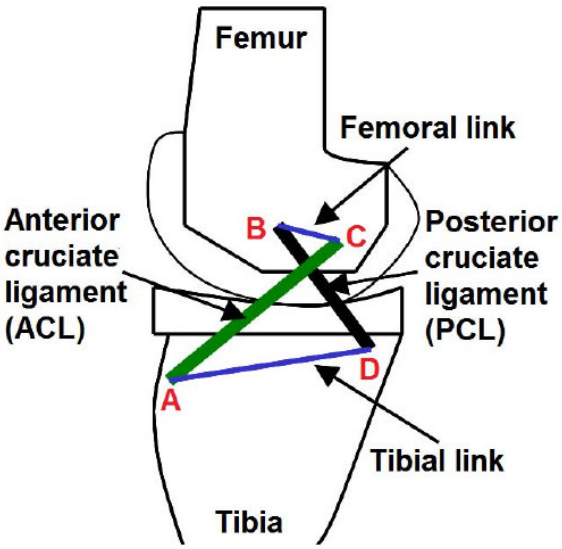

Source: Olinski et al. (2016)

The simple four-bar linkage composes an adequate knee orthosis, as reported by multiple studies in the literature. Bertomeu et al. (2007) used Freudenstein's equation (SUH; RADCLIFFE, 1978) and a genetic algorithm to create a four-bar linkage for an external knee hinge. The maximum error between the obtained solution and the model from Walker, Kurosawa, et al. (1985) was 1.993 mm. Comparatively, a simple monocentric hinge had a maximum misalignment of 27.212 mm, while a polycentric hinge with 8 mm gears had 23.920 mm. Bapat and Sujatha (2017) followed a similar procedure, now based on Walker, Rovick, and Robertson (1988), obtaining a mean error between the four-bar mechanism and the reference trajectory of only 0.2 mm.

The crossed four-bar was also used as an external knee joint for some quite different applications: for example, Tucker et al. (2013) created an external perturbator for impedance measurements, actuated by a clutch and a motor. Taking the model from Walker, Kurosawa, et al. (1985) as optimal, a four-bar linkage was optimized with a genetic algorithm, achieving a maximum error of 1.06 mm with the parameters shown in Table 4. Refer to Figure 40 for localizing the geometric parameters.

Table 4 – Final four-bar linkage parameters for the knee perturbator.

Parameter	**Value**	**Units**
L_1 linkage length	44.5	mm
L_2 linkage length	51.6	mm
L_3 linkage length	40.9	mm
L_4 linkage length	47.2	mm
$\Psi_{femoral}$ pitch	-27.5	deg
Ψ_{tibial} pitch	-19.5	deg

Source: Tucker et al. (2013)

Figure 40 – Geometric parameters of the four-bar linkage.

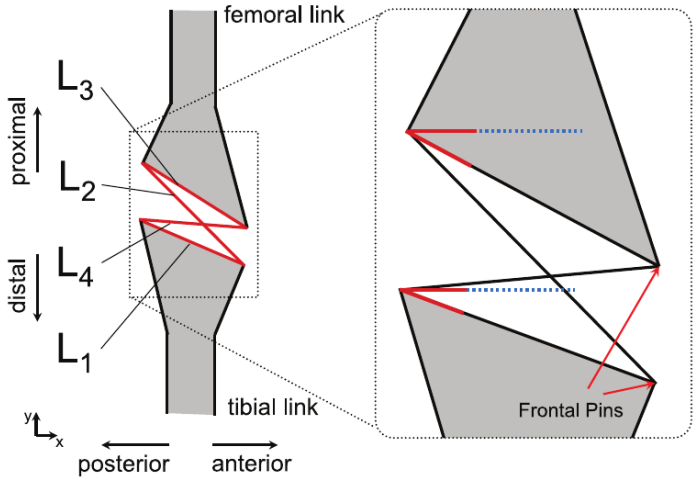

Source: Tucker et al. (2013)

Another application of knee orthoses is cycling assistance. The most utilized muscle group during cycling is the quadriceps femoris (the four anterior thigh muscles responsible for knee extension), while the hamstrings (three posterior thigh muscles) are less used. Employing a knee orthosis with a torsion spring (CHAICHAOWARAT; GRANADOS, et al., 2017), the cyclist can use the hamstrings to compress the spring during upward pedal motion, using the stored potential energy to help the quadriceps during downward motion; the result is a more balanced muscular activity. The torsion spring was later replaced by a planar one (Archimedean spiral), resulting in a more compact orthosis (CHAICHAOWARAT; KINUGAWA; KOSUGE, 2018). Both the systems used the four-bar parameters obtained by Tucker et al. (2013).

The previous examples from the State of the Art share common characteristics, such as the crossed morphology of the four-bar mechanism, which also does not meet the Grashof condition (WILLIAMS; REINHOLTZ, 1986): none of the links are capable of performing a full revolution. The femoral and tibial links also do not touch each other, a condition that was often checked, together with Grashof, during the optimization.

Last, aiming at reproducing the knee motion with greater accuracy, Olinski et al.

(2016) designed a variable four-bar linkage. This means that, instead of using four rigid bars, two of them are replaced by linear actuators, enabling instantaneous morphology adjustments. The resultant 3-DoF mechanism (Figure 41) is perfect in terms of tracking the reference trajectory (BERTOMEU et al., 2007; WALKER; KUROSAWA, et al., 1985). Authors suggest a less complex solution comprising only one variable link; however, this was not accomplished until the present date.

Figure 41 – Adaptive four-bar linkage: notice the two crossed bars, they are in fact linear actuators.

Source: Olinski et al. (2016)

3.2.3 Design

As presented above, it is clear that a four-bar mechanism is an excellent choice for mimicking the knee motion in the sagittal plane. However, this joint does not have purely planar motion (refer to section 2.3), and further aspects must be analyzed considering ergonomics and transparency, such as:

- The medial-lateral rotation performed by the knee when flexed (unlocked);
- The characteristic Q-angle of the femur, relative to the vertical tibia.

The first aspect would, at first glance, bring the complexity of the knee joint to another level. However, as an ankle joint with six degrees of freedom was previously designed, that mechanism is able to perform the medial-lateral rotation. What happens is that the tibia rotates around its own axis, creating a consequent rotation of the foot. Even with no motion of the lower leg supporting strap, the mechanism is able to follow the foot.

About the Q-angle, this aspect requires closer attention. As this angle may vary between individuals (for example, adult women have typically greater Q-angles, owing to

their wider pelves) (MOORE; AGUR; DALLEY, 2018), it is important to leave some room for small adjustments. Typical values go up to 17°, with larger angles occurring only due to a deformity called *genu valgum*. A too small Q-angle (close to zero), on the other hand, is called *genu varum* (MOORE; AGUR; DALLEY, 2018). A possible solution is to include passive rotational degrees of freedom, with limited range, so that the exoskeleton adjusts itself to the user when worn, or a simple adjustment feature that is able to compensate for these differences between individuals.

To fully define the planar four-bar mechanism, six parameters are needed: the length of the four bars, the angle of the tibial link relative to the tibia and the angle of the femoral link relative to the femur, with the knee fully extended. The instantaneous center of rotation of a crossed four-bar linkage is exactly the intersection point between the two crossed bars (TUCKER et al., 2013), which must align with the femoral spheres.

3.2.3.1 Four-bar linkage model

The first step for optimizing a four-bar linkage given a goal trajectory is to establish a mathematical procedure to solve for the kinematic parameters of the mechanism. In this particular scenario, one must solve for the instantaneous center of rotation (ICR) given the six parameters (four lengths and two angles, as earlier described) and the knee flexion angle. The linkage is parametrized as shown in Figure 42.

Figure 42 – Parameters for the knee four-bar linkage.

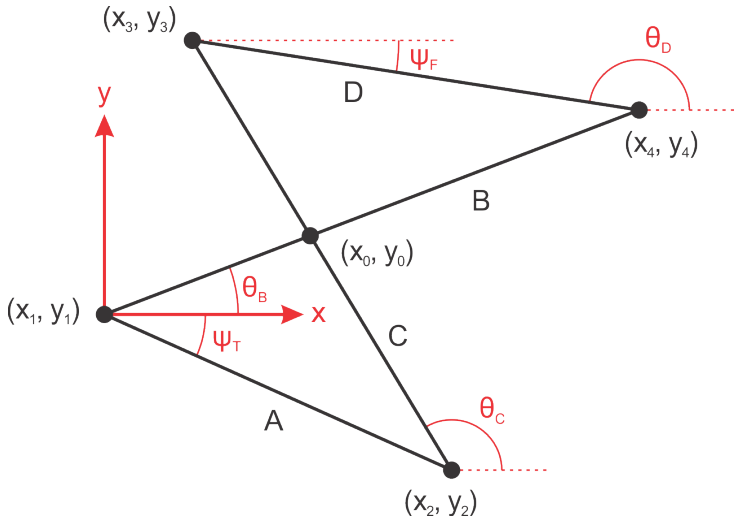

Source: authored

It is then possible to write the following equations:

$$x_1 = 0 \tag{3.11}$$
$$y_1 = 0 \tag{3.12}$$
$$x_2 = A\cos\psi_T \tag{3.13}$$
$$y_2 = A\sin\psi_T \tag{3.14}$$
$$x_3 = x_2 + C\cos\theta_C \tag{3.15}$$
$$y_3 = y_2 + C\sin\theta_C \tag{3.16}$$
$$x_4 = x_1 + B\cos\theta_B \tag{3.17}$$
$$y_4 = y_1 + B\sin\theta_B \tag{3.18}$$
$$x_3 = x_4 + D\cos\theta_D \tag{3.19}$$
$$y_3 = y_4 + D\sin\theta_D \tag{3.20}$$

Before heading to the solution, it is necessary to check whether the mechanism is impossible to be built, or is Grashof (allows continuous rotary motion). Both conditions enable the solution to be rejected. They are more easily checked when the four lengths are arranged in ascending order ($L_1 \leq L_2 \leq L_3 \leq L_4$). Then:

$$L_4 > L_1 + L_2 + L_3 \Rightarrow \text{Impossible} \tag{3.21}$$
$$L_1 + L_4 \leq L_2 + L_3 \Rightarrow \text{Grashof} \tag{3.22}$$

If none of the previous conditions are met, it is possible to compute the instantaneous center of rotation for each flexion angle θ_F using a Newton-Raphson iterative solution. The θ_D angle is analytically computed as follows:

$$\theta_D = \psi_F + \theta_F + \pi \tag{3.23}$$

Positions x_1, y_1, x_2 and y_2 are straightforward computed using equations (3.11) to (3.14), while equations (3.15) to (3.20) are used in the Newton-Raphson solution. For each flexion angle, it is also important to check if the tibial and femoral bars (A and D in Figure 42) are touching one another, which is also a condition to discard the solution. If these bars do not touch, line equations provide the position of the ICR as follows:

$$m_1 = \frac{y_4 - y_1}{x_4 - x_1} \tag{3.24}$$
$$m_2 = \frac{y_3 - y_2}{x_3 - x_2} \tag{3.25}$$
$$x_0 = \frac{y_2 - y_1 + m_1 x_1 - m_2 x_2}{m_1 - m_2} \tag{3.26}$$
$$y_0 = y_1 + m_1(x_0 - x_1) \tag{3.27}$$

Executing this solution for N flexion angles θ_F, N pairs (x_0, y_0) are returned, relative to point (x_1, y_1). To translate the reference to the ICR with the knee fully extended (as in Figure 38), simply subtract the first coordinate value from all points, as in the following equations:

$$x_0 = x_0 - x_0|_{\theta_F=0} \tag{3.28}$$

$$y_0 = y_0 - y_0|_{\theta_F=0} \tag{3.29}$$

3.2.3.2 Parametric optimization

With the previously described algorithm, the trajectory of the mechanism's ICR in planar coordinates can be described given a set of six geometric parameters (four lengths and two angles). Therefore, applying an optimization technique, it is possible to find the parameter set that best follows the average trajectory shown in Figure 38. The chosen technique is a genetic algorithm (MITCHELL, 1998), implementing crossover and mutation. Detais are available at Appendix A. For this particular problem, a population of 1024 individuals was used, running for a maximum of 200 iterations. The cost function is very simple, yet effective: the maximum across all flexion angles of the squared euclidean distance between the obtained ICR coordinate and the averaged reference (WALKER; KUROSAWA, et al., 1985; KUROSAWA et al., 1985; WALKER; ROVICK; ROBERTSON, 1988).

The algorithm has been executed from scratch a number of times to evaluate several slightly different solutions. The best overall solution, with a maximum error of only 0.65 mm, has the set of parameters given at Table 5.

Table 5 – Optimized parameters for the crossed four-bar linkage.

Parameter	**Value**
Length A (tibial link)	38.35 mm
Length B (crossed bar)	50.02 mm
Length C (crossed bar)	42.43 mm
Length D (femoral link)	43.93 mm
Angle ψ_F (femoral tilt)	14°
Angle ψ_T (tibial tilt)	8.2°

Source: authored

3.2.4 3D design

Defining the main geometric parameters for the four-bar linkage, it is now possible to design the mechanism in 3D CAD, including additional features to improve kinematic compatibility and user comfort. The crossed four-bar linkage aims at providing biomimetism

in the sagittal plane, however the Q-angle viewed from the frontal plane (Figure 9) should also be considered, with typical values ranging from 0 to 17°.

Moreover, the trajectory of the knee ICR was thoroughly investigated in previous sections, but a correct alignment of the four-bar linkage with the femoral sphere is important for adequate operation. Thus, the external joint must have adjustments in the sagittal plane to allow for correctly positioning the device relatively to the user's knee. Last, the vertical alignment between thigh and calf surfaces (to where the device is attached) also requires room for adjustment.

All the adjustments pointed out in the previous paragraphs are required as the joint has a single degree of freedom, and must fit human beings that have infinite variations in body structure. This scenario resembles, for example, ergonomic chairs: it is never possible to make a *one size fits all* product, requiring them to exhibit a number of different adjustment features.

Figure 43 – Rendering of the CAD for the knee joint. Red parts are fixture bands, yellow are vertical plates that allow planar adjustments, orange is the Q-angle adjustment part and green bars form the crossed linkage. Ratchets for adjustment are shown in metallic color.

Source: authored

Also, exoskeleton joints must have a correct attachment to the user's limbs. This connection is mediated by soft tissues, described as a combination of nonlinear elastic and viscoelastic elements (MAUREL, 1999). Attachment surfaces must preferably maximize the transmission of forces (this can be achieved with slight compression of the underlying

tissues), while being comfortable to wear, adjust, use and remove (ROCON; RUIZ, et al., 2005). This is addressed in the present work with rigid articulated bands, able to be opened such that the user can put on the exoskeleton from the front. These bands are held in place by a ratcheting fixture, rather uncommon regarding wearable robots. The author believes that they are superior to the more common adhesive fabric straps, making precise adjustments straightforward. With all the previously explained aspects in mind, the CAD representation for the prototype is created, shown in a rendered view in Figure 43.

3.2.5 Manufacturing, assembly and first impressions

A working prototype of the proposed knee joint was manufactured using mainly ABS 3D printing, and assembled using commercial fasteners. Figure 44 shows some pictures of the assembled prototype. It was further enhanced by adding strips of nonslip material, as shown in Figure 45. This enables the joint to be held firmly in place without needing to over-compress leg tissues.

Figure 44 – Manufactured prototype of the external knee joint.

(a) General overview.

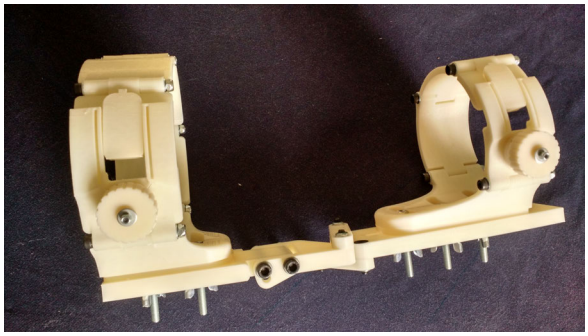

(b) Close-up of the four-bar linkage.

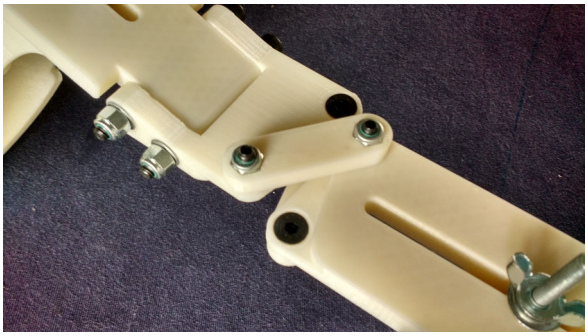

Source: authored

Both leg attachments can be fully opened, as Figure 45 suggests. This makes the joint easy to wear and remove, an operation that can be performed by the user alone, in a variety of postures. Contrarily to many commercial knee orthoses, the user does not need to slide the device from his foot towards the knee; instead, the proposed joint embraces the knee. Leg braces are both tensioned using ratchets, as shown in Figure 46, similarly to the leg attachment of the ankle joint (see Subsection 3.1.4). This design keeps being promising, as it allows for a precise adjustment of the fixture compression, holding stably in place, while being remarkably easy to unlock and remove.

Concerning the attachment band design, they were modeled as cylinders, with diameters corresponding to average thigh and calf sizes. The attachment sections that correspond to the fixture mechanism can slide relative to one another, enabling the band to open and close, thus fitting a range of individuals with diverse body structures. Figure 47 shows both attachments in isolation. This design choice allows for greater flexibility,

Figure 45 – Detail view of the inside of the upper leg attachment, showing the surface covered with non-slip material.

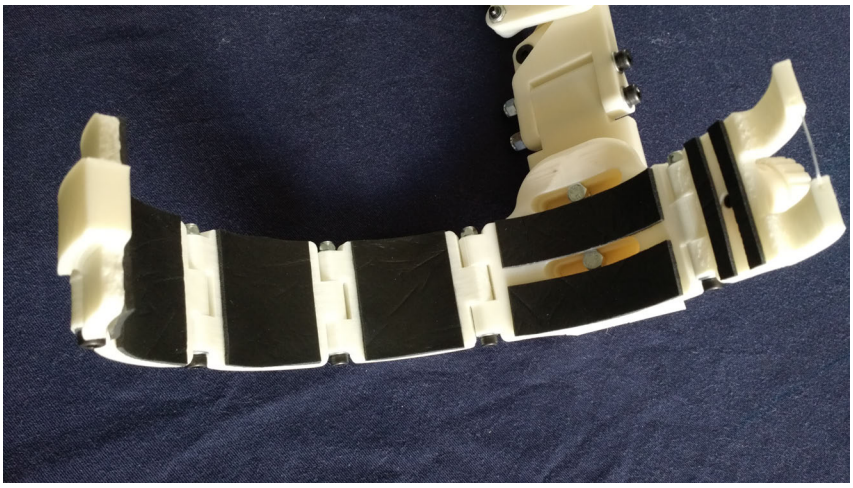

Source: authored

Figure 46 – The ratcheting fixture system, used at both upper and lower attachment bands. A *nylon* string is used to compress the band around the user's leg.

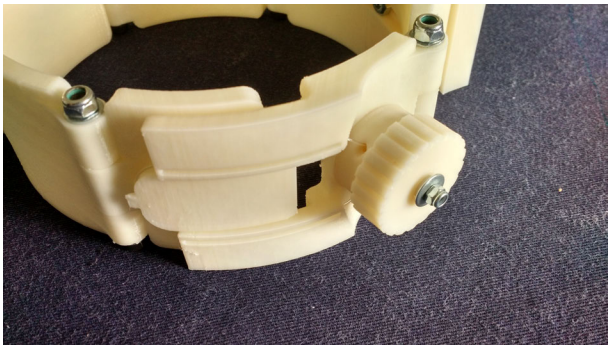

Source: authored

Figure 47 – Fixture bands for leg attachments of the proposed knee joint.

(a) Upper leg attachment.

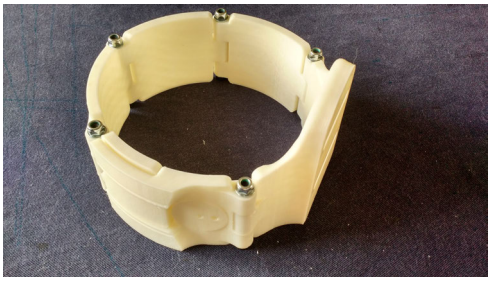

(b) Lower leg attachment.

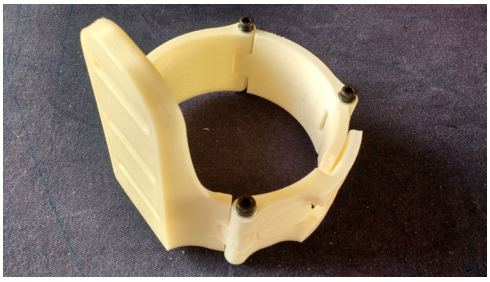

Source: authored

enabling it to be used by several individuals, while providing adequate fixture and comfort. Nevertheless, it is possible to enhance adaptability and comfort for specific individuals by creating customized fixtures by 3D scanning their legs. Nowadays, it is possible to reconstruct 3D surfaces using regular monocular cameras and photogrammetry software, like the open-source Meshroom[3]. Custom attachments can be manufactured using 3D printing, while keeping the ratchet mechanism for tissue compression.

3.2.6 Testing and assessment

One of the objectives of the complete knee joint design is to be easy to put on, adjust, and remove. A healthy subject is capable of performing these steps while sitting and demanding no external assistance. Figure 48 illustrates this procedure, showing a test subject placing the prototype on the right leg. The procedure is straightforward, embracing the leg from behind and closing the attachment band around it. Like in the ankle joint prototype (Subsection 3.1.4), the ratcheting mechanism brings great ease to adjusting the attachment tension in precise steps, while allowing the usage of materials more rigid than fabrics, which in turn enables greater efficiency in transmission of forces (see Subsection 2.4.3). After attaching both bands to the subject's leg, the prototype allows adjustment of the four-bar mechanism location on the sagittal plane and its distance from the leg using shims. It is important to closely align the point at which the bars cross to the knee center.

Next, Figure 49 shows the joint already attached to the subject's leg. The removal procedure is also straightforward, accomplished by axially pulling the ratchets away from the bands to unlock them, and opening them apart. Overall, the impressions with this proposed attachment system are very positive, supporting the belief that this is a promising replacement to the more widely used adhesive fabric straps.

The biomimetic design of this knee joint enables performing the full range of knee flexion. The subject must be able to completely flex the knee, as well as perform medial and lateral rotation with the knee unlocked. Figure 50 illustrates some daily motions that involve smaller angles of knee flexion. Figure 51, in contrast, shows poses with larger flexion angles. Figure 52 shows a genuflexion posture, with which the joint does not interfere, as it mostly covers the outer side of the knee.

In addition, Figure 53 captures an overall front view of the prototype. The captured standing posture also shows the Q-angle, small but existent, in this particular case. As mentioned in Subsection 3.2.4, the joint has an adjustment axis to follow the natural body geometry. This allowed visually assessing an important aspect of the knee joint: the Q-angle may experience a small variation when the knee is flexed. Figure 54 demonstrates this effect. As a result, it is possible to incorporate this degree of freedom as a passive joint of limited range, instead of locking it at a specific angle.

[3] Available from: https://alicevision.org/#meshroom

Figure 48 – Functionality of fixture bands for leg attachments of the proposed knee joint.

(a) Test subject placing the upper leg attachment, that embraces the thigh from behind.

(b) Test subject adjusting the tension of the leg brace, using the ratcheting mechanism.

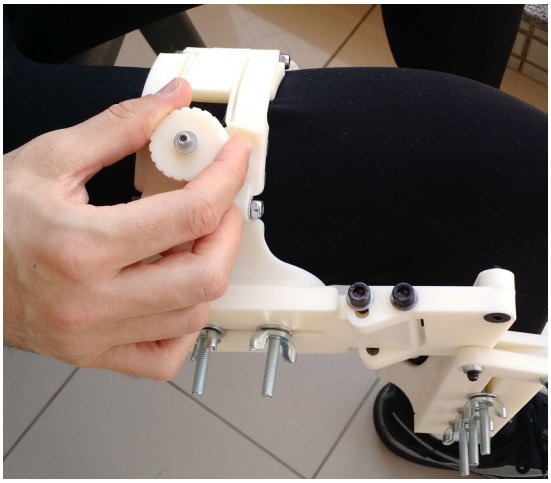

Source: authored

Figure 49 – Test subject wearing the external knee joint while sitting on a chair.

Source: authored

Figure 50 – Example upright poses performed with the knee joint.

(a) Slight knee flexion while performing a walking step.

(b) Knee flexion while stepping on a small bench, similar to upstairs motion.

Source: authored

3.2.7 Results and discussion

This section proposed creating a kinematically compatible external knee joint based on the internal geometry of the human knee, while also further exploring the concept of ratcheting mechanisms for limb attachments, first introduced in the ankle joint (refer to the previous section). The genetic algorithm proved itself to be of great value to find a crossed four-bar geometry that follows the natural motion of the knee's instantaneous center of rotation (ICR), that provides biomimetism on the sagittal plane. Additionally, a passive degree of freedom was added to follow the Q-angle between the femur and the tibia.

Following the designed geometry, a proof of concept prototype was built, using mainly ABS 3D printing. The four-bar linkage shows good robustness and minimal play, being also a type of mechanism that does not rely on friction between its components. The simplicity of a single-DoF mechanism contrasts with the need of a careful positioning of the system on the user's leg, as the mechanism needs to be aligned with the articular surfaces of the knee. This is a clear disadvantage of this type of mechanism, especially when considering more than a single human user. However, considering specifically the knee, it is a simple joint with little variation between subjects (WALKER; KUROSAWA, et al., 1985; KUROSAWA et al., 1985; WALKER; ROVICK; ROBERTSON, 1988).

Real-life assessment confirmed the attractive potential of the ratchet-based fixture

Figure 51 – Knee joint flexion while standing up.

(a) Active knee flexion, around 90 degrees.

(b) Maximum passive knee flexion.

Source: authored

Figure 52 – Genuflexion while wearing the external knee joint. The proposed geometry, with the joint not covering the patella region, does not interfere on such posture.

Source: authored

Figure 53 – Front view of the knee joint, with the test subject standing up. As most of the joint stays on the outer side of the leg, it does not demand the user to stand with the legs unnaturally apart. The Q-angle is evidenced by the red lines.

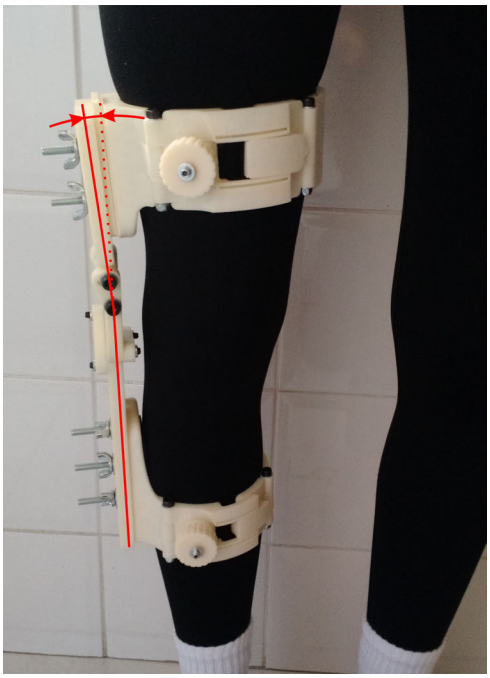

Source: authored

Figure 54 – Visual variation of the Q-angle, evidenced in red, during a full flexion of the knee joint.

(a) Knee extended. Here, the Q-angle is larger, with a visible gap between the top bolt washer and the right face of the ABS part.

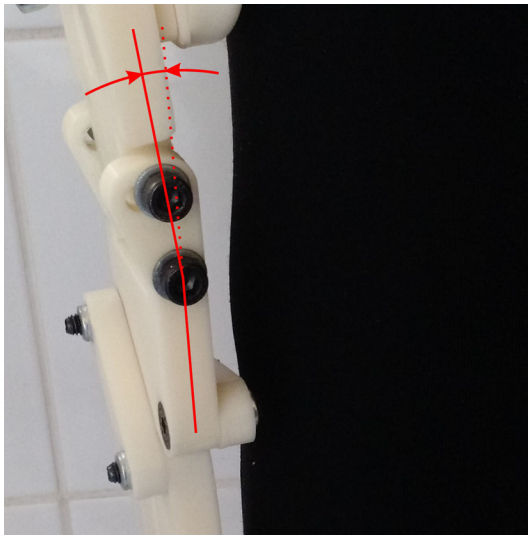

(b) Knee flexed. The Q-angle is now smaller (virtually zero), as the top bolt washer now overlaps with the right face of the ABS part.

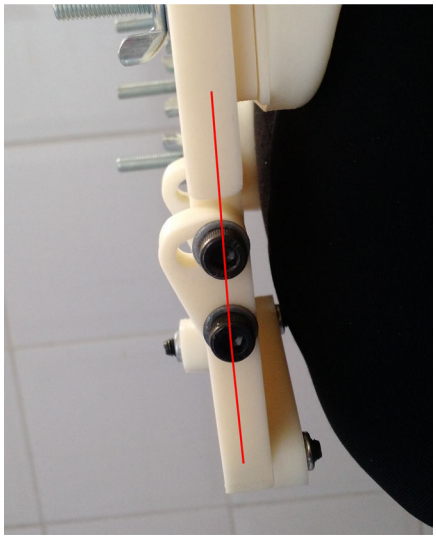

Source: authored

system, being easy to put, adjust compression, and remove. Designing the geometry of the fixture band based on the user's particular leg geometry is a possible step towards improving the comfort and performance of this concept. The added layer of nonslip material also helps mitigate attachment slippage without requiring exaggerated tissue compression.

The chosen location for the joint, on the outer side of the leg, follows many designs on the State of The Art and also commercial products, minimizing interference with the other leg and allowing poses with the knees on the ground. The four-bar mechanism is sufficiently stable to not require linkages on both sides of each knee.

3.3 The complementary joint principle: viewing human and exoskeleton as a single kinematic chain

Apart from proposing unconventional designs for external joints, the previous sections introduce general design principles that can be extended to any specific type of exoskeleton. These principles are summarized below, with their main features and disadvantages listed.

- The ankle joint (Section 3.1) possesses enough degrees of freedom to accommodate both the motion of the corresponding human joint and the anatomic differences between individuals, which can be interpreted as 3D translations. This enables covering the whole operational space of the corresponding human joint and fitting a range of different individuals without requiring mechanical adjustments. The main drawback is the resulting high DoF count, which translates into additional mechanical complexity and actuator requirements.

- The knee joint (Section 3.2), on the other hand, aims at mimicking the motion of the corresponding joint with great accuracy, so that misalignments are minimal and smaller than human joint laxity. As a result, the external joint has a single DoF (apart from the passive Q-angle axis, with limited amplitude), being thus mechanically simple and requiring a single actuator. However, the performance and comfort of the joint is intrinsically related to a sometimes nontrivial precise alignment.

A third principle for exoskeleton design emerges from a different way of facing this type of robot. Many wearable robots are conceived as fully actuated kinematic chains, which are later attached to the human user: see Figure 55 for examples. This becomes clear due to the fact that such robots can stand still by themselves, without being attached to a human user.

[4] Available from: http://connor-mccann.com/wp-content/uploads/2016/10/Ekso.png

[5] Available from: https://exoskeletonreport.com/wp-content/uploads/2016/09/CYBERDYNE-Inc-HAL-Side-View.png

Figure 55 – Examples of exoskeletons with fully actuated kinematic chains.

(a) The Ekso GT exoskeleton.

(b) The HAL exoskeleton.

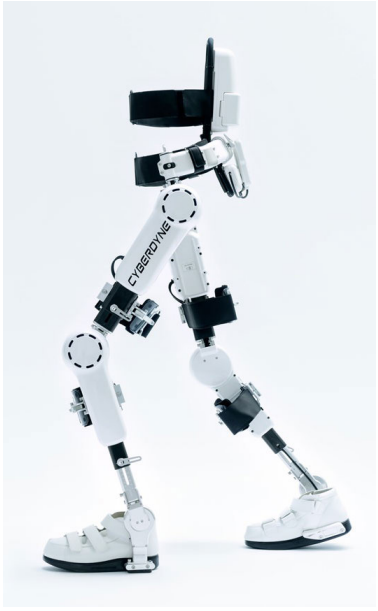

Source: connor-mccann.com[4] and exoskeletonreport.com[5]

In contrast, there are proposals such as those depicted in Figure 56, that do not possess fully actuated kinematic chains. Instead, these exoskeletons have passive degrees of freedom, such that the kinematic chain becomes fully actuated only when both the robot and the human user are coupled together. This concept is also shown by Pons (2008, Chapter 5) as a strategy to avoid misalignments between human and robot corresponding joints (see Subsection 2.4.2 for more details), illustrated in Figure 57.

As a result, this type of design views the exoskeleton as a device that adds to the kinematic chain defined by the user's skeleton, providing assistance just to motor tasks. Consequently, they can almost be interpreted as *exomuscles*. This is certainly a clever approach, as in most cases the human bones are very strong and stable[6], and the wearable robot does not aim at strengthening this structure, but assisting the organs that generate motion: the muscular system. As a result, such complementary wearable robots are also attractive for the context of transparent operation, as the focus is on helping healthy individuals expand their capabilities.

6 Patients with illnesses that severely affect postural and motor capabilities may suffer from not having a more rigid and stable exoskeleton, and might benefit more from fully actuated robots.

7 Available from: https://i.insider.com/573c7feddd089568328b47a8?width=3418

Figure 56 – Examples of exoskeletons that are not fully actuated when isolated, thus relying on the connection with the human user to create a fully actuated kinematic chain.

(a) The Harvard Soft Exosuit (PANIZZOLO et al., 2016).

(b) The MIT Anklebot.

(c) A parallel hip exoskeleton.

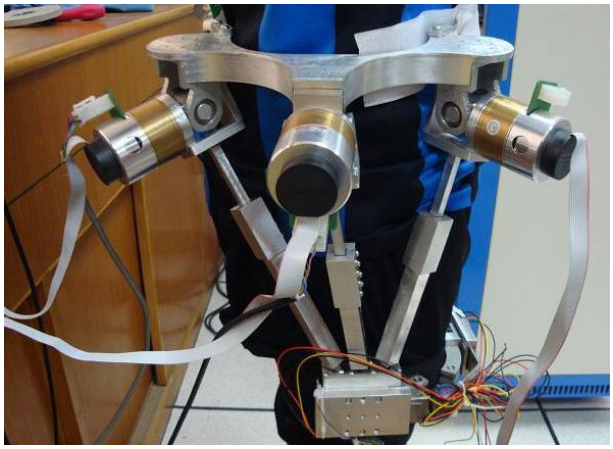

Source: businessinsider.com[7], Roy et al. (2007), and Yu and Liang (2012)

Figure 57 – Example of how an exoskeleton with passive joints can favour ergonomics. In (a), the singular rotational joint has a different instantaneous center of rotation (ICR) than the elbow, causing attachment slippage and shearing forces. In (b), the added translational joint compensates this effect, enhancing user comfort.

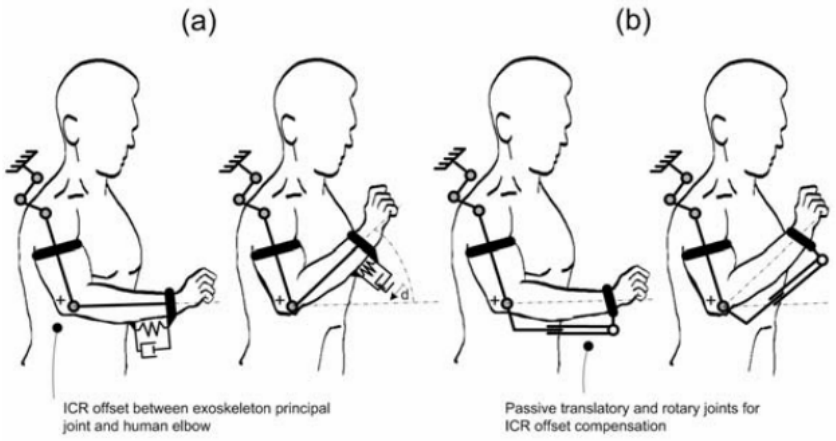

Source: Pons (2008, Chapter 5)

3.4 Closing remarks

This chapter explored several concepts and ways of designing external exoskeleton joints, focusing on the human lower limbs. A series of unconventional geometries and mechanisms were put into perspective, many of which show great potential to improve transparency levels of exoskeletons, and even related characteristics such as comfort and ease of use. This was also an opportunity to investigate an uncommon type of fixture, based on rigid attachments with a ratcheting mechanism to provide compression and adequate coupling between user and robot. The author believes that using this concept together with custom-made attachments may bring one of the best solutions in terms of force transmission efficiency and user comfort, while being remarkably easy to operate.

To sum up, the key concern for any anatomical exoskeleton design is to take the user's natural motion into consideration, not limiting or interfering with it in any detrimental way. The user's kinematic chain can also be favorably utilized during the design phase, working in conjunction with the exoskeleton. Indeed, the objective of a wearable assistive robot is not to be just another skeleton or some type of external armor, but to add power to the user's muscular system. This becomes particularly clear regarding soft wearable robotics: the human skeleton provides the structure, and the robot actuators cooperate with the user's muscles to provide motor and metabolical benefits.

4 MOTION PREDICTION

As introduced in Section 2.5, a promising strategy of enhancing transparency of exoskeleton robots is to predict the most likely user motion in a future time horizon, then act based on this prediction. Thus, it is essential to develop a software solution capable of generating such predictions. This part of the dissertation will start by defining high-level requisites, then selecting the most promising software architecture, which will then have its architecture fine-tuned for this specific problem. Analysis of the proposed algorithm comes next, covering selected use cases. Then, the effectiveness of the proposal as a whole is discussed.

4.1 Requisites

A motion prediction algorithm directed towards exoskeletons in general must follow a series of high-level requirements, so that it is capable of deployment in real usage scenarios. The items below show the most important requisites, and in some cases the chosen solution is also briefly presented.

- *Use only kinematic data as input.*
  The aim of the prediction algorithm is to function simultaneously with the exoskeleton operation, relying on data that is readily available and of easy interpretation. This implies using body poses, represented by joint angles, which are agnostic to limb size variations between individuals. Here, it is chosen not to monitor biological signals such as neuronal activity or EMG because they are less practical, more invasive, and also demand calibration and additional algorithms for data interpretation, such as biomechanical models or learning algorithms. Refer to Section 2.2 for more details.

- *Allow any input sample rate.*
  The prediction algorithm must not be hardware-specific, i.e., it must function in a series of different exoskeletons, which might be equipped with different sensory and acquisition systems. As a result, variations in sample rates for the input data are likely to occur, and the chosen model must adapt to these changes. Thus, the sample rate (Hz) or time (s) has to be taken into account, in the form of a model input, or as a hyperparameter.

- *Predict at any given time horizon.*
  Different exoskeletons may differ not only from their sensory systems, but also from control and actuation systems. This implies that the best time horizon for the pose prediction might vary between exoskeletons, and even for each operating condition.

Controller cycle times may also be faster than the acquisition counterparts, requiring more than one prediction before a new measurement becomes available. The proposed algorithm must then enable asking for a specific time in the future. It is worth noting that these future horizons lie in the near future (some milliseconds), as they are meant to be used as anticipatory inputs for control algorithms and actuators.

- *Work with any exoskeleton structure.*
  Many motion prediction works from the State of the Art consider whole-body motion, as both input and output. However, exoskeletons developed until the present day are quite diverse, and there is certainly more to come considering the recent advances in the area. A specific exoskeleton may be, for instance, whole-body (ISHII; YAMAMOTO; HYODO, 2005; SANKAI, 2006), lower-limb only (KAZEROONI et al., 2005; LEE; SANKAI, 2002), upper-limb only (ROSEN; PERRY, 2007), for a single leg (BANALA et al., 2008) or arm (ROCON; MANTO, et al., 2007; SCHIELE; VISENTIN, 2003), or for a specific joint (PRATT; KRUPP, et al., 2004; ROY et al., 2007). All these differences must be taken into account by the prediction algorithm, for it to be universal and applicable in several robots.

- *Work for various subjects and tasks, while allowing fine-tuning.*
  The prediction algorithm must show good generalization capacity, especially when targeting mass-production exoskeletons, with the same model being used by various people with different motion patterns and necessities. Nevertheless, enabling it to be fine-tuned for a specific task or individual is a welcome feature. For example, an exoskeleton may be factory loaded with a universal version of the algorithm, which collects data from its user during normal operation, making small adjustments to its behavior to become even more transparent for that specific subject.

- *Avoid characteristics that discourage real-time operation.*
  Robots, including exoskeletons, rely on real-time algorithms for stable operation, which are characterized by deterministic cycle times. Some types of computation, specially iterations with unknown total number of cycles, may not be suitable for real-time operation, specially when low-power embedded hardware is considered. Thus, the best structure for a prediction algorithm should operate in a fixed number of steps, with preferably low computational requisites.

4.2 The proposal

The present work proposes utilizing a fully data-driven learning algorithm for human pose prediction: an artificial neural network (HAYKIN, 2009). More specifically, the model architecture must contain some type of *recurrent neural network* (RNN), which is specialized in processing sequential data, due to the existence of a *hidden state*, in

addition to the inputs of traditional perceptrons (ROSENBLATT, 1958). The sequential data, in the present application, are the joint positions themselves. The added hidden state (the RNN's memory) enables viewing this category of neural networks as computer programs, that run accepting a set of inputs and keep another set of internal variables (KARPATHY, 2015); in fact, RNNs are Turing-Complete (SIEGELMANN, 1995). This means that, while non-recurrent (multi-layer perceptron, convolutional, etc.) networks can approximate any function, given a sufficient finite number of units (MCCULLOCH; PITTS, 1943), recurrent networks can approximate any *program* runnable on a Turing Machine (TURING, 1948).

However, vanilla RNNs have limited capacity, such as vanishing and exploding gradients, as well as difficulty dealing with long-term dependencies and noisy data. A different structure, called *Long Short-Term Memory* (LSTM), was introduced by Hochreiter and Schmidhuber (1997), with the objective of tackling the intrinsic problems of standard RNNs. It has a series of internal gates, each one with its own set of parameters, and two internal states. A more recent alternative is the *Gated Recurrent Unit* (GRU) (CHO et al., 2014), with fewer parameters and computations, what does not mean that GRUs are inferior than LSTMs: each implementation may work best for each specific problem (CHUNG et al., 2014). A related work, aimed at motion prediction (AKSAN; KAUFMANN; HILLIGES, 2019), found LSTM to consistently outperform GRU in a series of experiments. Thus, this work will focus only on this type of recurrent network.

Apart from proposing the GRU, Cho et al. (2014) also created an encoder-decoder architecture known today as *sequence-to-sequence* (seq2seq), which is composed by two interconnected RNNs: an *encoder*, which consumes and interprets input sequential data, transforming it onto a latent representation, and a *decoder*, which produces an output sequence from the latent interpretation. This approach is particularly useful for machine language translation, and was also used for motion prediction by Martinez, Black, and Romero (2017), producing a series of most likely body motions. As the present work focuses on predicting a single posture at a given time in the future, only a single RNN is needed for interpreting sequential input data. Multiple predictions, if required, are obtainable by querying the model more than once.

That being said, this work introduces *HuMAn* (Human Motion Anticipation), a neural network aimed at predicting future human poses having a sequence of past poses as input. Being a learning algorithm, it requires a dataset with sufficient data to allow good generalization. The chosen dataset will be presented in Section 4.3, followed by a detailed explanation of the model structure in Section 4.4.

4.3 The AMASS dataset

To train a motion prediction model with good accuracy and generalization, while incorporating a series of common movements performed by humans, it is of vital importance to have a dataset showing such motions recorded from real subjects. For this purpose, the AMASS (Archive of Motion Capture as Surface Shapes) dataset (MAHMOOD et al., 2019) was selected. It contains[1] more than 45 hours of recordings, spread across 18 sub-datasets (see Figure 58). Every sub-dataset has a specific set of motion capture markers, which are all converted into a single model, containing a skeleton with 23 spherical joints, plus root (hip bone) orientation and translation. Recordings also have varied sample rates: 60, 100, 120, and 250 Hz.

Figure 58 – Example data from some AMASS sub-datasets. From left to right: CMU (CMU, 2000), MPI-HDM05 (MÜLLER et al., 2007), MPI-Limits (AKHTER; BLACK, 2015), KIT (MANDERY et al., 2015, 2016), BMLrub (TROJE, 2002), TCD (HOYET et al., 2012), and ACCAD (OSU, 2021).

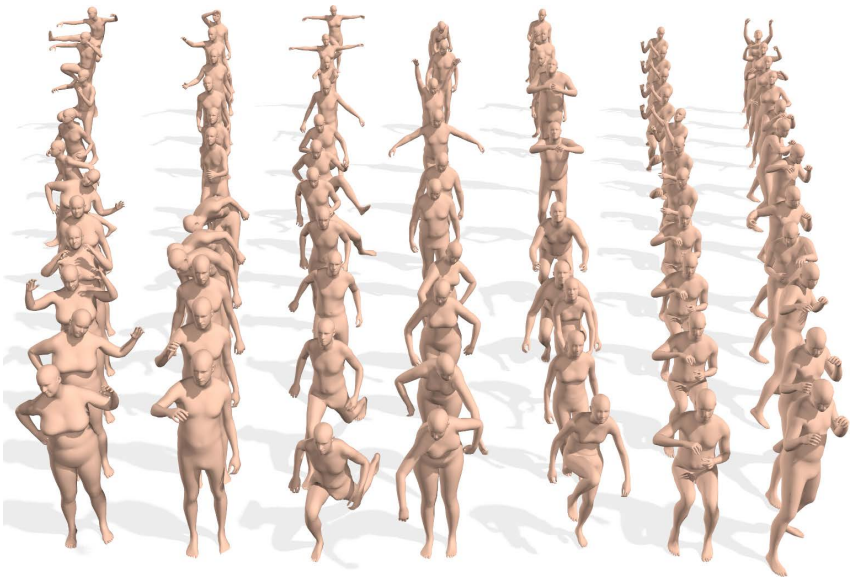

Source: Mahmood et al. (2019)

As its name suggests, AMASS also contains body shape data, encoded into a set of blend shapes, interpreted as the principal components of human body structure. This technique was introduced by the SMPL (Skinned Multi-Person Linear Model) body model (LOPER et al., 2015), which allows estimating the pose of each skeleton joint from a set of surface mesh vertices. This enables converting motion capture data (with markers located over the subjects' skin) to skeleton joint poses. SMPL has been upgraded through time, resulting in a series of models with particular characteristics, as summarized by the following items.

[1] As of April 2021.

- *SMPL* (Skinned Multi-Person Linear Model) (LOPER et al., 2015) lays the foundations for all posterior methods, learning shape representations from 3D scans.
- *DMPL* (Dynamic SMPL) (LOPER et al., 2015), proposed in conjunction with SMPL, introduces additive blend shapes that vary through time, modeling dynamic deformations that occur during body movement.
- *SMPL+H* (SMPL with articulated hands) (ROMERO; TZIONAS; BLACK, 2017) adds hand motion to the SMPL body.
- *SMPL-X* (SMPL eXpressive) (PAVLAKOS et al., 2019) is the most complete model based on SMPL, maintaining hand motion and adding an expressive face.
- *STAR* (Sparse Trained Articulated Human Body Regressor) (OSMAN; BOLKART; BLACK, 2020) is a drop-in replacement for SMPL, still considering just body motion, introducing a sparse mapping between joint motions and the corresponding surface mesh deformation. This results in a model with fewer parameters and fixes some problems with SMPL, such as spurious long-term correlations and shape-agnostic pose corrective offsets.

Figure 59 – Kinematic tree for the STAR model, with 23 joints plus root translation and orientation. It is the same for the previous models.

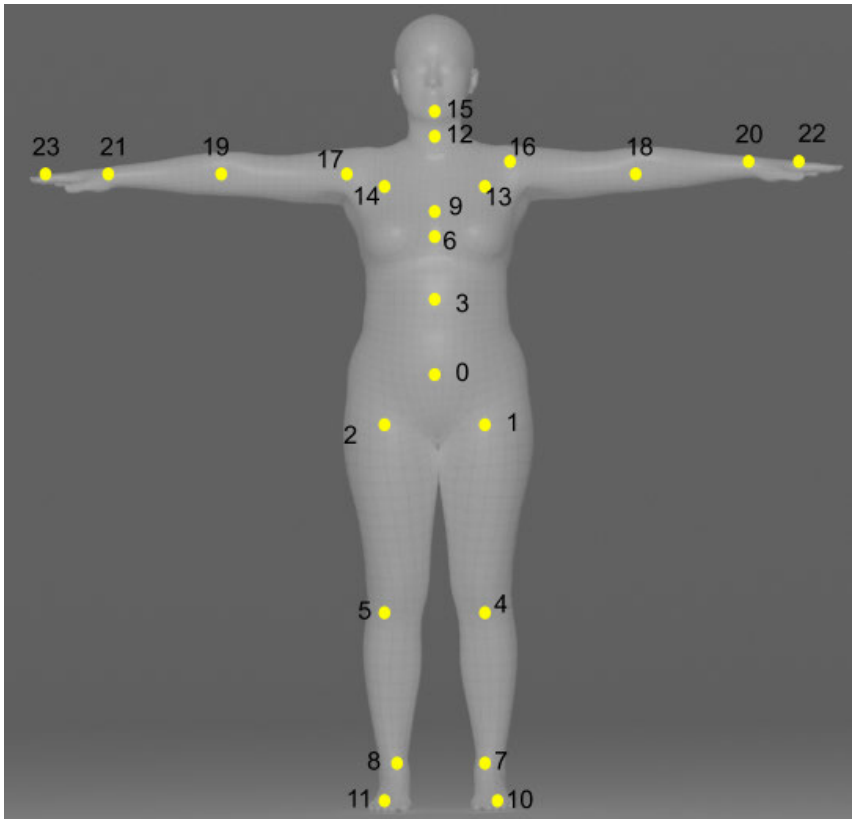

Source: Osman, Bolkart, and Black (2020)

While the previous body models are not directly used for training or evaluating the proposed prediction algorithm, they are useful for visualization purposes. As the present work focuses only on body motion (excluding hands and facial expression), STAR is the model of choice, being 100 % compatible with AMASS recordings. Figure 59 shows the kinematic tree for the body of all models. The 24 joints comprise the root orientation (pelvic bone, joint #0) and 23 anatomical joints. All joints are considered spherical, independently of which anatomical body joint they represent. Thus, each joint possesses three degrees of freedom, resulting in a total of 72 joint angles, that correspond to the first 72 entries of the *poses* array of all AMASS recordings.

4.4 Breaking down the model architecture

Knowing the general outline of the neural model and having an overview of the training dataset, this section will then make an in-depth description of the model architecture, highlighting the reasons behind most of the choices. It starts with the four data inputs:

- *Pose input:* a vector with 72 joint angles, according to the kinematic tree of Figure 59.
- *Selection input:* a vector with 72 inputs, accepting only two values: 0 or 1. This controls which joint angles are available, enabling customization for each particular exoskeleton type. Following the order of the previous input, filling an entry with 1 means that its corresponding joint is active and must be considered, and 0 makes it inactive.
- *Elapsed time:* elapsed time, in seconds, since the last pose measurement. All AMASS recordings have their frame rate (in Hz) annotated, requiring a simple inversion for feeding into the network. This keeps the values between 0 and 1.
- *Prediction horizon:* indicates the time, in seconds, to predict poses in the future. The model is trained considering a maximum horizon of 0.5 seconds, roughly twice the human reaction time to tactile stimuli (BARNETT-COWAN; HARRIS, 2009). The option for 0.5 seconds seeks a balance between small maximum horizons - that may be inadequate to stimulate model learning about this important input parameter - and very large ones - that are unnecessary considering the targeted control anticipation application, while also demanding too long input sequences.

The model uses only poses as inputs, not demanding velocity or acceleration. Such variables could enhance prediction; however, they may demand numerical differentiation, which is prone to introduce noisy data into the model. As the algorithm also knows the

time between two consecutive measurements, this enables building internal knowledge about kinematic time derivatives.

Pose inputs (in radians) are standardized before feeding them into the model. This and other types of data normalization are widely used in neural networks, known to improve the final accuracy and make the training procedure faster and more stable (SOLA; SEVILLA, 1997; KIM, 1999). In this model, standardization is done by computing, *a priori*, the mean and standard deviation of each one of the 72 angles for the whole training dataset. At runtime, the input data is scaled to a distribution with zero mean and unit variance as follows:

$$\theta_{std} = \frac{\theta_{input} - \mu}{\sigma} \tag{4.1}$$

In which:

- θ_{std}: standardized joint angle;
- θ_{input}: input joint angle;
- μ: mean for this angle computed with training data;
- σ: standard deviation for this angle computed with training data.

The other model inputs do not require normalization. The input pipeline follows by multiplying the normalized pose inputs with the selection input (element-wise), thus zeroing out all unused joint angles. These 72 angles are then fed into a single LSTM layer, together with the elapsed time input. The LSTM has a total of 1024 units as in Aksan, Kaufmann, and Hilliges (2019); preliminary tests have shown that enlarging the number of units does not sensibly improve performance, meaning that an LSTM of this size might have enough capacity to process and interpret human motions as parameterized in AMASS. Stacking a second LSTM layer also brings no clear improvement while noticeably slowing training; this might come from the fact that joint angles are not very abstract data (opposed to images or text, for example) and that predicting short-term future motion relates to the most recent actions taken by the human. As a result, a single layer seems to be enough.

The output of the LSTM layer (sometimes called *context* or *latent representation*) undergoes a 20 % dropout, to avoid overfitting (SRIVASTAVA et al., 2014). Dropout is not applied directly to the pose inputs, as the selection scheme already handles removing some information. The resulting representation feeds the prediction part of the model, together with the selection input and both time inputs (elapsed and future horizon). The structure of the prediction layers will be explained in greater depth afterwards.

Summarizing what has been presented so far, the model has a LSTM layer to interpret the sequence of poses, and a prediction layer to build the most probable future poses. This sequential structure could be the model's final shape, however it can be greatly improved by adding a residual connection. Residual networks have proven themselves useful for enhancing information flow in deeper networks, with reduced gradient degradation and more efficient training (HE et al., 2016; HUANG; LIU, et al., 2017). In the present case, the residual connection relates to the fact that a human pose in the near future can be described as a small perturbation around the current pose. Therefore, the inner prediction layer will learn to compute displacements to be added to the pose input - instead of the pose as a whole. Figure 60 shows a diagram that illustrates the model structure so far.

Figure 60 – Block diagram of the HuMAn prediction model.

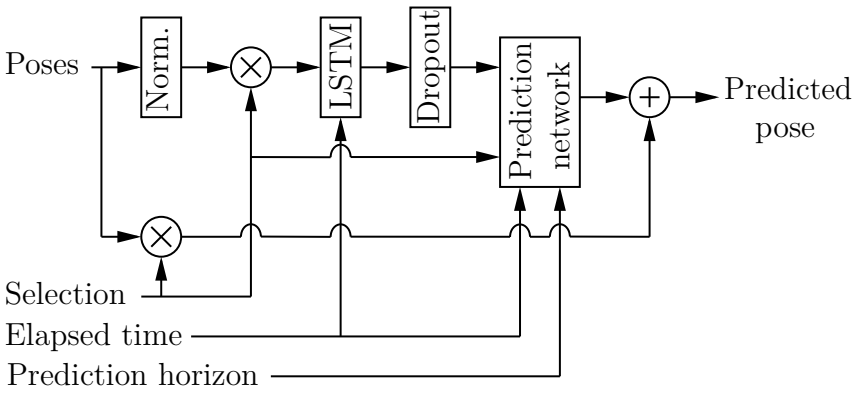

Source: authored

4.4.1 The joint prediction network

Future motion prediction is handled inside the HuMAn network by specialized sub-models. Many previous works use a single structure to predict all joint poses in one go, such as dense layers or decoder structures (FRAGKIADAKI et al., 2015; DU; VASUDEVAN; JOHNSON-ROBERSON, 2019; GHOSH et al., 2017; MARTINEZ; BLACK; ROMERO, 2017; PAVLLO; GRANGIER; AULI, 2018). Following the findings of Aksan, Kaufmann, and Hilliges (2019), this work implements a type of structured prediction layer, known to improve the prediction quality and make more targeted use of the model's total capacity. The original proposal of this network structure is illustrated in Figure 61. Gradient flow during backpropagation is also effective, as it is possible to penalize individual joint predictions. This is one example of how the structure of an artificial neural network - and not only its bulk size - can improve its effectiveness in solving a particular problem.

A structured prediction layer is defined by a set of individual fully connected networks, each one responsible for predicting the three angular displacements of a single body joint. They are connected in such a way that each subnetwork receives the prediction

Figure 61 – Structured prediction layer (SPL). h_t represents the context of past observations, generated by the recurrent layer. The SPL contains a number of subnetworks, each one responsible for predicting future poses of a single joint, $\hat{x}_t^{(k)}$. These subnetworks are connected following the kinematic chain of the human skeleton.

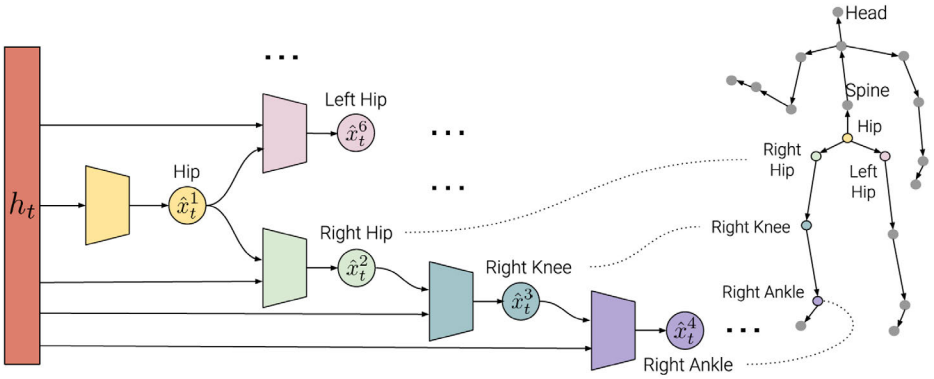

Source: Aksan, Kaufmann, and Hilliges (2019)

of their parents as input. The parents of a given joint are the ones that lie in the path connecting it to the root joint (hip bone). Aksan, Kaufmann, and Hilliges (2019) define two types of structured connection: *dense* - where each prediction subnetwork receives the predictions for *all* parent joints as inputs - and *sparse* - where only the prediction of the *immediate* parent is shared. Figure 62 clarifies both connection types.

Figure 62 – Illustrations of the two modalities of structured connection for motion prediction, according to Aksan, Kaufmann, and Hilliges (2019).

(a) Dense connections. (b) Sparse connections.

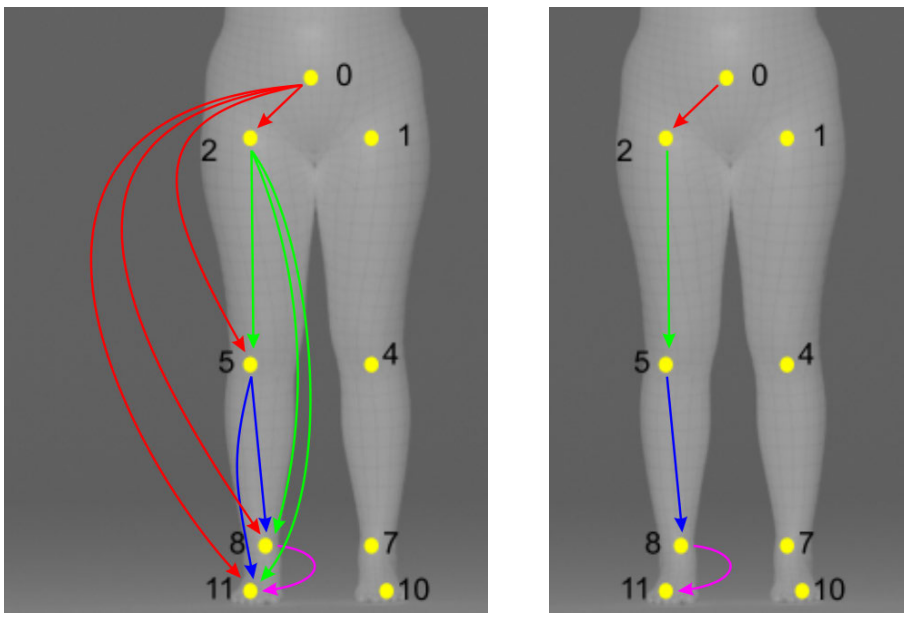

Source: adapted from Osman, Bolkart, and Black (2020).

As the present work aims at creating an algorithm capable of being used in a series of different exoskeleton designs, a dense structured prediction was chosen. This enables not losing important data if, for some reason, a specific design chooses not to assist a joint (or multiple joints) in the middle of some of the skeleton branches. Dense connections were also superior than sparse on the RNN-SPL model (AKSAN; KAUFMANN; HILLIGES, 2019).

According to the AMASS skeleton (Figure 59), the HuMAn network has a total of 24 prediction subnetworks, one for the root orientation (joint #0) and 23 for the anatomical joints. They all have a common structure, the only difference being the number of inputs from previous predictions. The root joint, for example, has no parents, while the knees have two parents each (hip and root). Hands have a total of eight parents. Thus, the subnetworks differ in the number of input neurons. The complete input of each network is given by a concatenation of the LSTM output after dropout (1024 units), the part of the selection vector corresponding to that particular joint (3 units), the elapsed time input (1 unit), the time horizon input (1 unit), and the predictions from parent joints (variable number of units: 0, 3, 6, . . . , 24).

The input layer of each prediction network is connected to a dense layer with 128 units, followed by a 20 % dropout. Seeking to enhance nonlinearity, a second dense layer, now with 64 neurons, is added sequentially, also followed by a 20 % dropout. The interleaved dropout layers are again intended to avoid overfitting (SRIVASTAVA et al., 2014), discouraging the model to memorize predictions. After the second dropout, a linear (dense with no activation function) layer with three outputs is added, matching the required dimensions for a single joint.

All prediction subnetworks inside the HuMAn model are chosen to have dense layers with Mish (MISRA, 2019) as the activation function. See Appendix B for a comparison between this recent alternative and the other widespread functions. So far, the prediction network for each joint is summarized by the diagram shown in Figure 63. However, there still are improvements to be made. The first modification involves forcing unused angles (as defined by the selection input) to always output zero as the predicted displacement. This ensures that child joints do not receive spurious parent predictions on the outputs of their subnetworks, and that the full predicted pose does not contain misleading values on unused entries. This is easily obtained by making an element-wise product between the output of the linear layer and the corresponding components of the selection input.

The second improvement concerns the variable prediction horizon: with the present structure, this parameter is fed as input to the subnetwork. Thus, the two hidden layers have to interpret this single input as a type of scaling factor, outputting small displacements for short time horizons and progressively large differences as longer times are requested. Seeking to exacerbate this scaling effect, a scalar product between the output of the linear

Figure 63 – Block diagram of a single prediction subnetwork. The dashed red rectangle highlights the discussed structure. The "Gather" block represents picking only the three components of the selection input related to each specific joint.

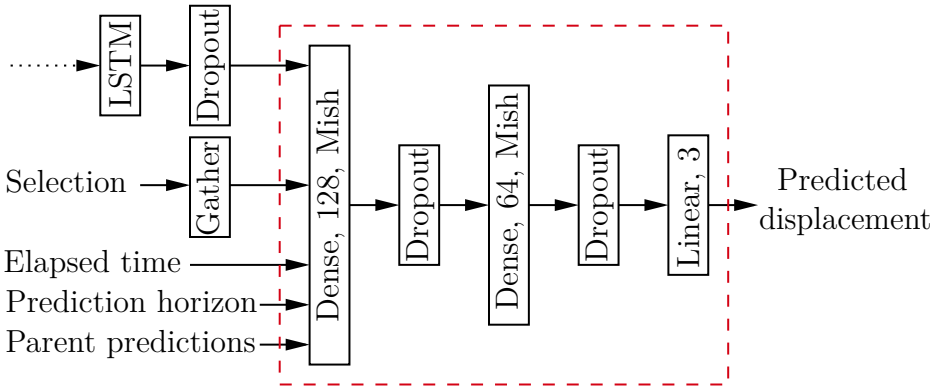

Source: authored

layer and the prediction horizon is added. Without this explicit product, the model had a strong likelihood of giving the actual pose as output: in other words, the predicted displacements were always very close to zero. This is understandable, as a horizon of a couple of milliseconds makes actual and future poses quite similar. This fact implies that the subnetworks would certainly need more capacity, becoming possibly wider or deeper (SZEGEDY; LIU, et al., 2015), to correctly interpret and handle the prediction horizon. Adding the scalar product helps to appreciably reduce the prediction error.

Figure 64 – Block diagram of a single prediction subnetwork, after adding products with the corresponding selection input and the prediction horizon.

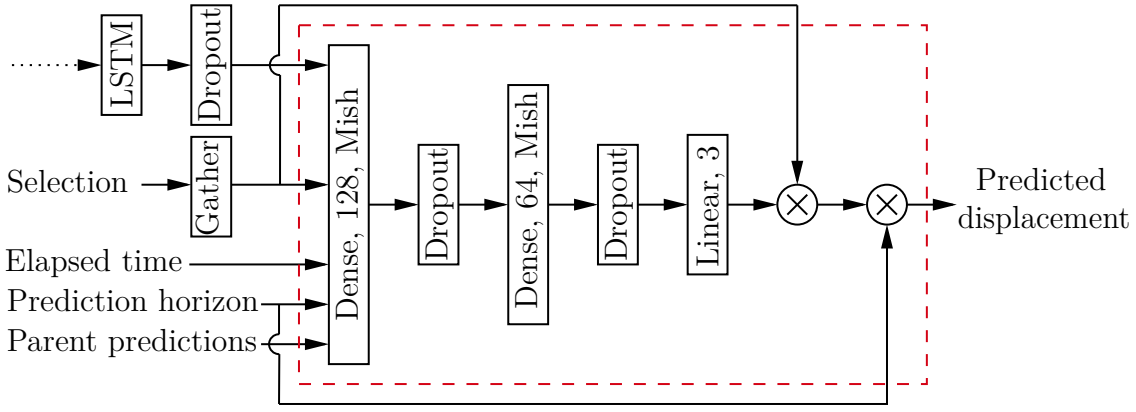

Source: authored

After adding the two aforementioned improvements, the diagram for a single subnetwork is shown in Figure 64. The model as a whole contains 24 individual instances of this prediction subnetwork, and their outputs are concatenated into a vector with 72 angular displacements, to be finally summed with the pose input according to the residual connection (see Figure 60).

4.5 Data preprocessing

> Data scientists spend 80 % of their time preparing and cleaning their data. They spend the other 20 % of their time complaining about preparing and cleaning their data.
>
> *Kirk Borne*

The AMASS dataset, available for download at the project website[2] upon registration, free of charge, already has all data converted into a common structure. Each one of the 18 sub-datasets is presented as a directory, with sub-directories representing different subjects. Inside, there are multiple NumPy files (*.npz* extension[3]), one for each recording. This brings great ease to navigate through all datasets and their respective recordings, with straightforward loading provided by NumPy routines[4]. Each *.npz* file contains the following data:

- *poses*: $m \times n$ array, with m being the number of available joint angles and n, the total number of frames. It contains joint angles (in radians), with the first 3 representing root orientation, and the next 69 body joints shown in Figure 59. Some recordings may contain additional pose data, representing articulated hands.
- *trans*: $3 \times n$ array, with n being the total number of frames. It contains Cartesian translations of the root joint.
- *mocap_framerate*: floating point number, representing the motion capture frame rate in hertz. The original recordings vary between 60, 100, 120, and 250 Hz.
- *gender*: string, enabling to choose the most appropriate gender of the body model (SMPL, SMPL-H, STAR, ...) for visualization. Can be *male*, *female*, or *neutral*.
- *betas*: 1D array, containing the blend shape components for visualization purposes. These components are constant for the whole motion sequence. The first 10 components are sufficient to provide a visually accurate 3D body.
- *dmpls*: $m \times n$ array, with m being the number of additive blend shapes and n, the total number of frames. These are the dynamic pose components introduced by Loper et al. (2015) that, differently from *betas*, vary throughout the motion. They

[2] Available from: https://amass.is.tue.mpg.de/
[3] See more at: https://numpy.org/doc/stable/reference/generated/numpy.lib.format.html
[4] Available from: https://numpy.org/doc/stable/reference/generated/numpy.load.html

provide more accurate skin deformation for the SMPL model and are not used by the more recent STAR model.

Regarding this work, the most important data from each AMASS recording are the *poses* array (its first 72 lines) and the *mocap_framerate*. Body translation is not used for prediction purposes, while *gender* and *betas* may be used for visualization. The choice of the STAR model, and the greater focus on skeletal motions, makes *dmpls* not necessary. Therefore, one of the objectives of data preprocessing is keeping only necessary information, optimizing the input pipeline.

4.5.1 Offline preprocessing

To allow efficient usage of AMASS data, this work focuses at performing all possible preprocessing in advance while also converting data from NumPy *.npz* files to TFRecords[5]. This is the most efficient way to store datasets when working with *TensorFlow* (ABADI et al., 2015), which is the framework of choice for the implementation of HuMAn. The offline preprocessing pipeline focuses on the following main tasks:

- *Discarding unneeded data.*
  As already mentioned, the model needs just the first 72 pose components (joint angles) and the motion capture frame rate (converted to sample or elapsed time, in seconds) for training. For visualization purposes, gender and blend shapes (the first 10 *betas*) are also kept. Additional data from the *.npz* files do not need to be loaded into TFRecords.

- *Performing data augmentation through frame rate dropping.*
  As one of the goals of this model is to work with any input sample rate (for diverse embedded sensory systems), it is important to feed it with data recorded at multiple rates. However, the AMASS dataset contains only four different rates. This is easily solved by dropping the frame rate, picking only specific data points from the poses array. For example, keeping every two columns represents halving the input frame rate. It is chosen to drop frame rates to three different extents which, together with the original recordings, delivers a total of 13 unique rates. See Table 6 for details.

- *Generating sets of fixed-length sequences.*
  LSTMs are capable of processing sequences of any length, as they consume one step at a time, keeping their internal state between iterations. However, training can operate more efficiently if sequences have the same size, enabling them to be batched together and also not demanding dynamic reshaping of kernels inside the graphics

[5] Available from: https://www.tensorflow.org/tutorials/load_data/tfrecord

processing unit (GPU). Thus, subsequences are extracted from all sub-datasets, with target lengths of 256, 512 and 1024 steps.

Table 6 – frame rate drop for AMASS data augmentation.

Drop	**Original frame rate [Hz]**			
factor	60	100	120	250
2	30	50	60	125
4	15	25	30	62.5
5	12	20	24	50

Offline data preprocessing is handled using multiprocessing, enabling multiple CPU cores to process data in parallel, thus enlarging data throughput. Unnecessary data is simply ignored, and the gender strings are converted into an integer representation: *male* is stored as -1, *female* as 1, and *neutral* is matched with 0. After that, frame rate dropping is performed by discarding slices of the original *poses* array. Generation of fixed-length sequences is a rather more involved process, as the processed recordings must contain the target number of data points plus the maximum expected prediction horizon (set as 0.5 s), which represents a variable number of frames according to the sample rate. The total length of a data window is given by the following expression:

$$len_{window} = integer\left(len_{sequence} + \frac{hor_{max}}{dt}\right) \tag{4.2}$$

In which:

- len_{window}: total length of the data window;
- $len_{sequence}$: target sequence length (user-defined);
- hor_{max}: maximum prediction horizon (set as 0.5 s);
- dt: sample time between two consecutive inputs.

Aiming to take the most out of the original recordings, a stride percentage is defined based on the computed window length. A stride of 100 % means creating windows that are exactly adjacent, without any overlapping. The extreme opposite is shifting a single frame, thus repeating all data points except the first and last ones. It becomes clear that small strides create more sequences, at the cost of information redundancy. Large strides, on the other hand, reduce the total number of sequences, however these have more dissimilar pose data. This work uses a 25 % stride as a default, seeking a balance between data quantity and diversity.

Next, it may seem obvious to place the first window at the beginning of the original pose sequence, and then shift it according to the computed stride length, up to the end of the original recording. However, many AMASS recordings begin and end with a particular calibration pose: the subject standing up, with legs slightly apart and arms open, similarly to Figure 59. Thus, the most useful poses are located in the middle of the time series, which is where the windows are extracted from. The procedure involves computing the maximum number of windows that fit inside the sequence, respecting the stride percentage, and leaving out the same (plus or minus one) number of frames from beginning and end.

4.5.2 Online preprocessing

As mentioned in Section 4.1, the proposed model architecture is aimed at some specific use cases. Firstly, any trained model should respond adequately to any input sample rate, any desired prediction time horizon, and any combination of anatomical joints. As all these three parameters are controllable through model inputs, it is important to assure that the model receives a rich combination of these different situations during training. Various sample rates (13 total) were already created in offline preprocessing, as explained in Section 4.5, starting as low as 12 Hz and going up to 250 Hz.

Considering multiple prediction horizons, offline preprocessing also cares about storing an additional number of time steps to the selected sequence length, allowing predicting up to 0.5 s in the future. This enables a step of *online* preprocessing, consisting of randomizing this future time, then selecting two slices of data to be fed as input and

Figure 65 – Fictitious example of online preprocessing, considering a 10 frames sequence length and a 10 Hz frame rate. Offline preprocessing stores a sequence with 10 initial frames added with 5 more frames, to allow predictions up to 0.5 s in the future. While loading the data, a random future time is selected: in this case, 0.2 s is used as example. The input sequence always corresponds to the first l frames, being l the sequence length. The target sequence (training labels) is shifted to the right a number of frames corresponding to the randomized future horizon.

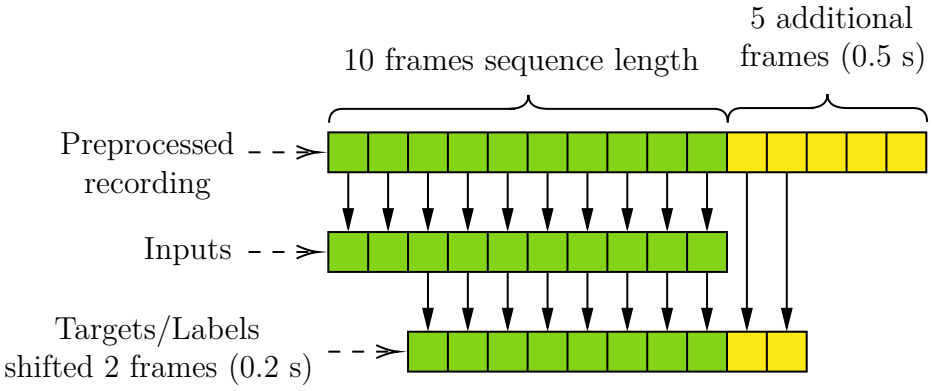

Source: authored

target during training. Figure 65 shows a simple example for better understanding. This procedure enables further enriching the dataset, as a single preprocessed sequence can be used to train predicting poses at different future time steps.

Learning how to handle different sets of anatomical joints is also a task for online preprocessing. As the model has an input meant to be filled with 72 zeros or ones, according to a specific set of joints, this step involves randomly selecting the values of this input. This is done by using two uniform distributions: one ranging from -0.5 to 0.5 (the same value throughout all 72 inputs) and other from 0 to 1 (one for each input). They are both summed and rounded towards the nearest integer. The first distribution, from -0.5 to 0.5, controls the likelihood of outputting zeros (closer to -0.5) or ones (closer to 0.5). Otherwise, using a single normal distribution to directly fill the 72 zeros would always result in a roughly 50/50 balance between zeros and ones.

4.6 AMASS dataset splits

After establishing the preprocessing procedure, AMASS sub-datasets must be grouped together in splits with specific objectives. As in any machine learning application, it is important to have a set of *training* data, and another set of unseen examples, called *validation* data (HAYKIN, 2009). This work adapts the recommended splits (MAHMOOD et al., 2019) as follows:

- *Training:* ACCAD, BMLmovi, BMLrub, CMU, DFaust-67, EKUT, Eyes-Japan, KIT, MPI-Limits, TotalCapture, and Transitions.
- *Validation:* HumanEva, MPI-mosh, SFU, and SSM-synced.

The previous splits refer to the *general-purpose* or *universal* model, that learns a variety of motion types from multiple subjects. But, as mentioned in the beginning of this chapter, this work also aims at assessing the effectiveness of this prediction algorithm in modeling a specific motion task, or adapting itself to a particular subject. For these additional objectives, two sub-datasets were selected, respectively: BMLhandball and MPI-HDM05.

The first specific sub-dataset is the most recent incorporation of AMASS, containing, as the name suggests, handball motions. It contains a total of 10 subjects, with half of them labeled as *novice* and the other half, *expert*. This dataset will be used to illustrate learning a specific motion pattern, either by refining the general algorithm - a *transfer learning* approach (BOZINOVSKI, 2020) - or by training the network from scratch. The 10 available subjects enable performing a 10-fold cross-validation (HAYKIN, 2009) study.

The second selected dataset, MPI-HDM05 (MÜLLER et al., 2007), has only four subjects, but they performed a set of varied - and labeled - types of motion, according to

the project website[6]. Here, the complete set of motions for a single subject is split between test and validation, with the first 90 % of each motion type selected for training, and the last 10 % set aside for validation. This results in a total of eight files, two for each subject. The aim of MPI-HDM05 in the present work is learning subject-specific motions, utilizing also both transfer learning and training from scratch.

4.7 Training

After establishing the whole preprocessing pipeline, with offline and online steps, the model can be trained using standard TensorFlow routines. The first model to be trained is the general one, using the training and validation datasets listed on the previous section. Weight initialization uses standard values for the LSTM layer[7], while dense layers use the He uniform variance scaling initializer (HE et al., 2015) for weights and a constant value of 0.1 for biases.

As already mentioned, preprocessing extracted three different sequence lengths: 256, 512, and 1024 frames. Training starts with the shortest, as long sequences can be affected by vanishing gradients. The chosen optimizer is *Adam* (KINGMA; BA, 2014), with learning rate set to 0.001. This work does not use learning rate decay or annealing, as proposed by (SMITH et al., 2018). Instead, training is stopped after one epoch with no improvement in validation loss, and batch size is doubled. Only when the maximum allowed batch size is reached, due to GPU memory (VRAM) limitation, learning rate decay is activated, being reduced to 20 % of the actual value every epoch without improvement in validation loss. If, even after decaying the learning rate, the validation loss does not decrease, the sequence length is increased.

After going over all sequence lengths and all admissible batch sizes, the model is fitted again, using the shortest sequence of 256 frames and batch size 32, but using the Stochastic Gradient Descent (SGD) optimizer with Nesterov momentum (SUTSKEVER; MARTENS, et al., 2013). This aims at converging the model weights to a limit cycle (CHAUDHARI; SOATTO, 2018) around a relatively flat minimum within the multi-dimensional loss surface. Weights are averaged after each epoch, following Stochastic Weight Averaging (SWA) (IZMAILOV et al., 2018), which provides better generalization. The same procedure of 20 % learning rate decay is applied until the validation loss does not improve. After all these procedures, the universal prediction model is ready to be saved. The training scheme is illustrated in Figure 66 and implemented using TensorFlow callbacks.

Training on the other selected sub-datasets follows a similar procedure, regarding the procedure shown in Figure 66, the main difference being training and validation data

[6] Available from: http://resources.mpi-inf.mpg.de/HDM05/
[7] See details at: https://www.tensorflow.org/api_docs/python/tf/keras/layers/LSTM

itself. The BMLhandball dataset aims at evaluating the model's capacity of adapting to a specific motion pattern, while MPI-HDM05 assesses how the model can adapt itself to a specific subject. Training, on both cases, starts either from the previously trained general model or from scratch. In the first case, there is a slight adaptation in the training loop, as it uses only the maximum batch size for each sequence length.

Figure 66 – Flowchart representing the model training procedure.

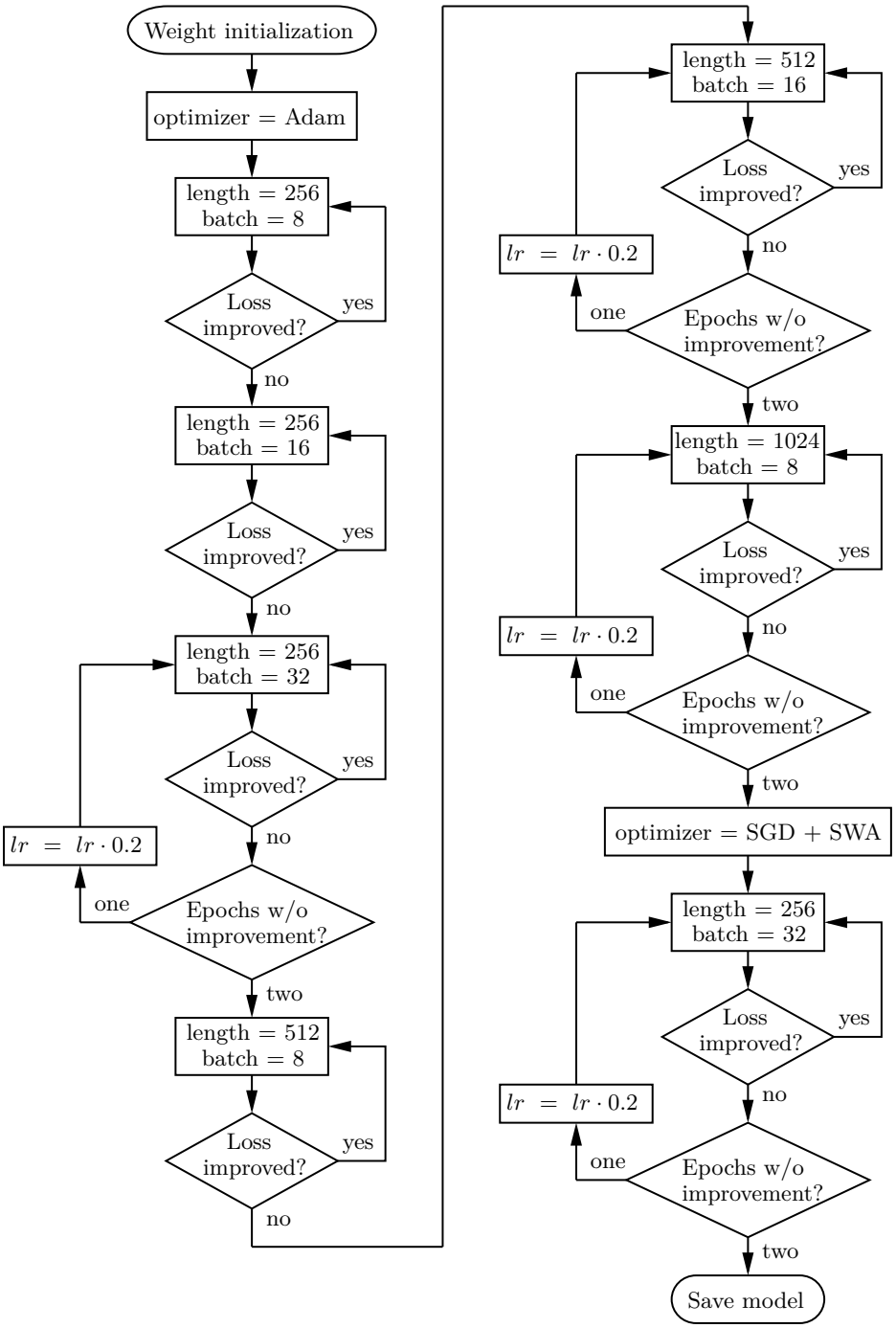

Source: authored

4.7.1 Hardware and software used

As already mentioned, the HuMAn neural network was implemented using TensorFlow, version 2.4.1, Python 3.8.5, and CUDA 11.0, under Windows 10 Pro 64-bits. The source code is available as a pip[8] compatible repository on GitHub[9]. It runs on very modest hardware, as the present work was developed using an Intel Core i5-4440 CPU, 16 GB of DDR3 RAM and an NVIDIA GeForce GTX 970 (4 GB GDDR5). When using more capable GPUs, it is possible to use larger batch sizes to speed up training, remembering to adjust (increase) the learning rate (SHEN, 2018). NVIDIA RTX GPUs also benefit from using mixed-precision computation[10].

4.8 Results and discussion

This section aims at assessing the performance of the HuMAn motion prediction algorithm from a number of different perspectives. As this is a markedly multidimensional problem, it is important to revisit some of the most important variables to be explored during this evaluation, listed below. The multiple evaluation procedures will focus on one of the main aspects or a combination of them.

- The input sample rate (see Table 6);
- The prediction horizon (up to 0.5 seconds in the future);
- The skeleton structure, represented by the combination of enabled joints, chosen using the selection input (see beginning of Section 4.4);
- The motion sequence length;
- The different validation datasets (see Section 4.6), called *universal*, *BMLhandball* and *MPI-HDM05* from this point onwards.

The metric of choice for performance assessment is absolute error, as it translates directly to the disparity between prediction and ground truth. Contrarily, the loss function used for training was the mean squared error, due to its smoothness and ability to decrease low errors while giving greater significance to errors of higher magnitude. Evaluation also incorporates standard deviation to indicate the dispersion of results. Both the mean absolute error and the standard deviation are computed for each recording, over all joint angles and time steps. To avoid storing large amounts of data when results are computed across many recordings, a procedure to continuously update values of mean and standard deviation was apllied when necessary. This procedure is described in detail in Appendix C.

[8] Available from: https://pip.pypa.io/en/stable/
[9] Available from: https://github.com/Vtn21/HuMAn
[10] Refer to https://www.tensorflow.org/guide/mixed_precision.

The first step in evaluation will comprise the effect of sample rate and prediction horizon on the quality of model outputs. At the same time, four different skeleton structures are analyzed: the whole body (root orientation and 23 anatomical joints), arms and legs combined (discarding motions such as root orientation, spine shape, and head and neck motion), legs only (representing a lower-limb exoskeleton), and arms in isolation. Figures 67 to 70 show the results, all using the *universal* model trained with the *training* split described in Section 4.6, and the *validation* dataset with 256-frame sequence length.

Figure 67 – Mean absolute error and standard deviation for predictions using all 72 angles of the AMASS skeleton.

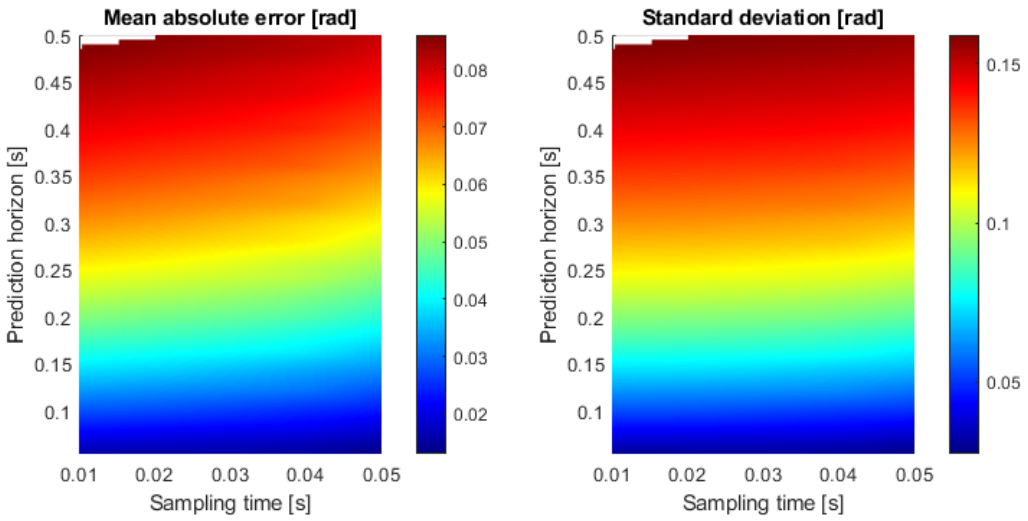

Source: authored

Figure 68 – Mean absolute error and standard deviation for predictions using the arms and legs (16 total joints) of the AMASS skeleton.

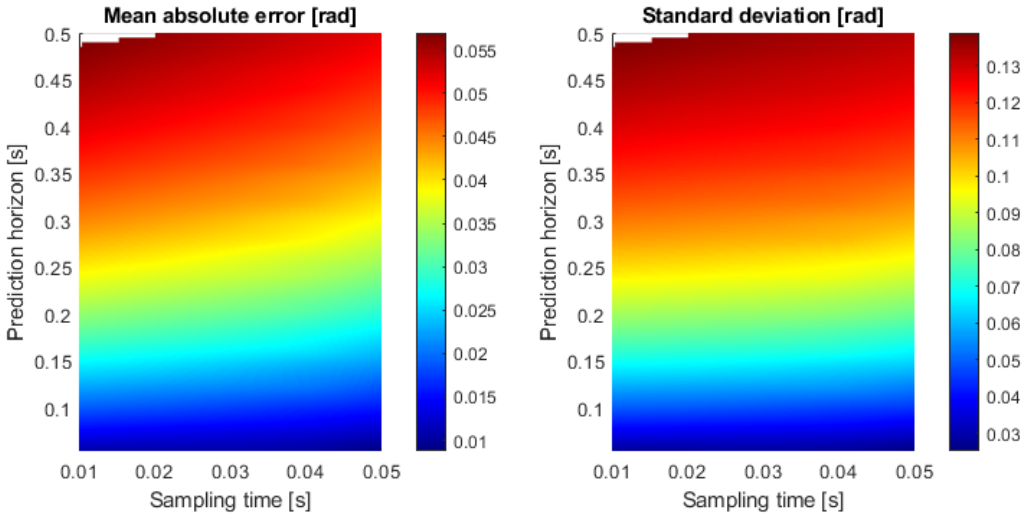

Source: authored

Figure 69 – Mean absolute error and standard deviation for predictions using only the legs (8 joints) of the AMASS skeleton.

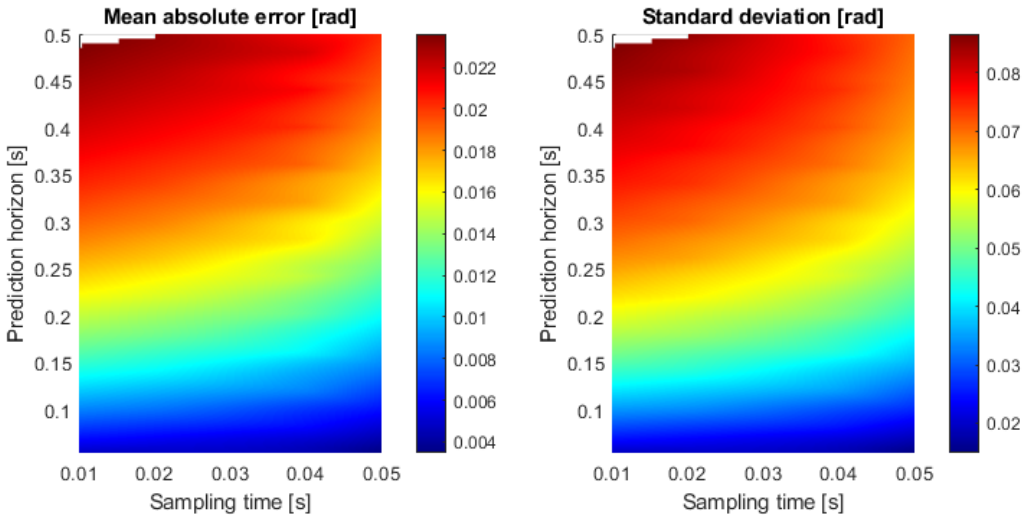

Source: authored

Figure 70 – Mean absolute error and standard deviation for predictions using only the arms (8 joints) of the AMASS skeleton.

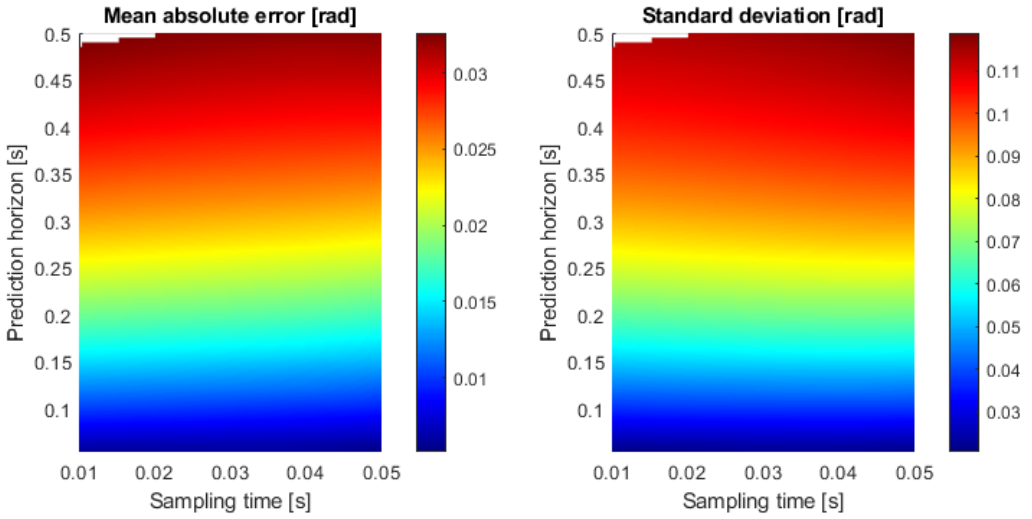

Source: authored

The generated plots enable a series of analyses. As expected, the best results are obtained with high sample rates (low sample times) and short-term predictions. While long prediction horizons are a challenge for the model, being the region where the highest errors are always located, it has adequate robustness to low sample rates. Thus, it does not require sophisticated sensory systems with large bandwidths. The predictions also exhibit a high quantitative precision, with the worst-case average error (Figure 67) below 0.1 radians. The model also shows greater ease in predicting a lower number of joint angles, despite having one subnetwork for each joint (three angles). This most probably relates to the recurrent section of the neural network, that may work more efficiently when focusing on just a small subset of the complete set of joints.

The comparison between different sets of joints brings an interesting question to be answered: can the prediction algorithm perform better for a given set of output joints if additional joints are observed? In other words, is it worthwhile to install motion sensors on regions of the user body that are not assisted by the exoskeleton's actuators? To answer this question, the prediction errors are compared for a fixed set of output joints and variable combinations of inputs in Figures 71 to 73.

Figure 71 – Mean absolute error (μ) and standard deviation (σ) obtained while predicting movements of legs and arms using two different combinations of input joints. Notice that the surfaces do not intercept one another.

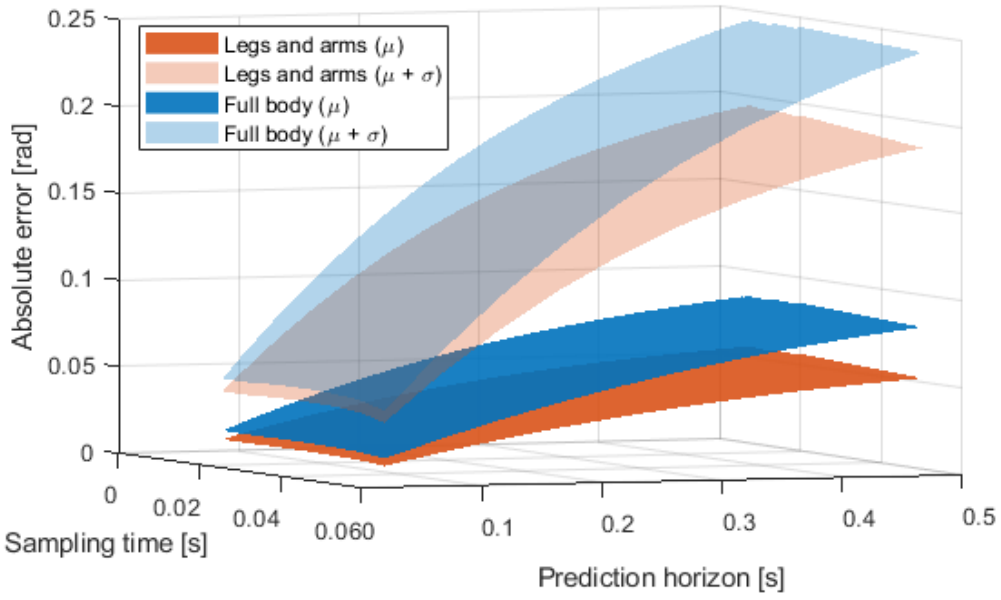

Source: authored

Results are comparable to the plots in Figures 67 to 70, where the model showed better performance for lower joint counts. Here, adding more input joints while predicting the same set of joints not only did not increase performance, but instead resulted in larger mean absolute errors, possibly due to the added variability of input data. This means

Figure 72 – Mean absolute error (μ) and standard deviation (σ) obtained while predicting movements of legs using three different combinations of input joints. Notice that the surfaces do not intercept one another.

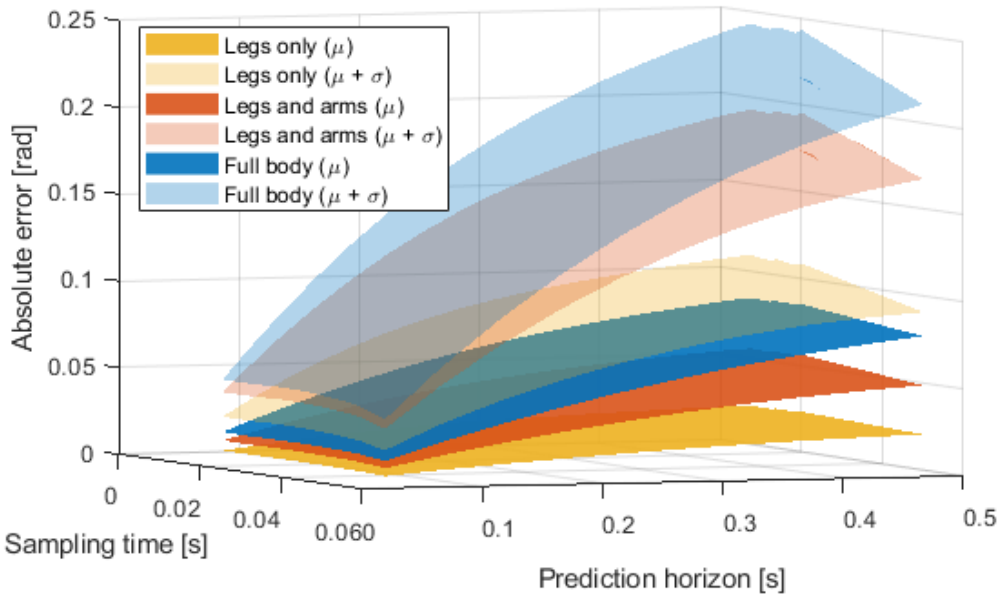

Source: authored

Figure 73 – Mean absolute error (μ) and standard deviation (σ) obtained while predicting movements of arms using three different combinations of input joints. Notice that the surfaces do not intercept one another.

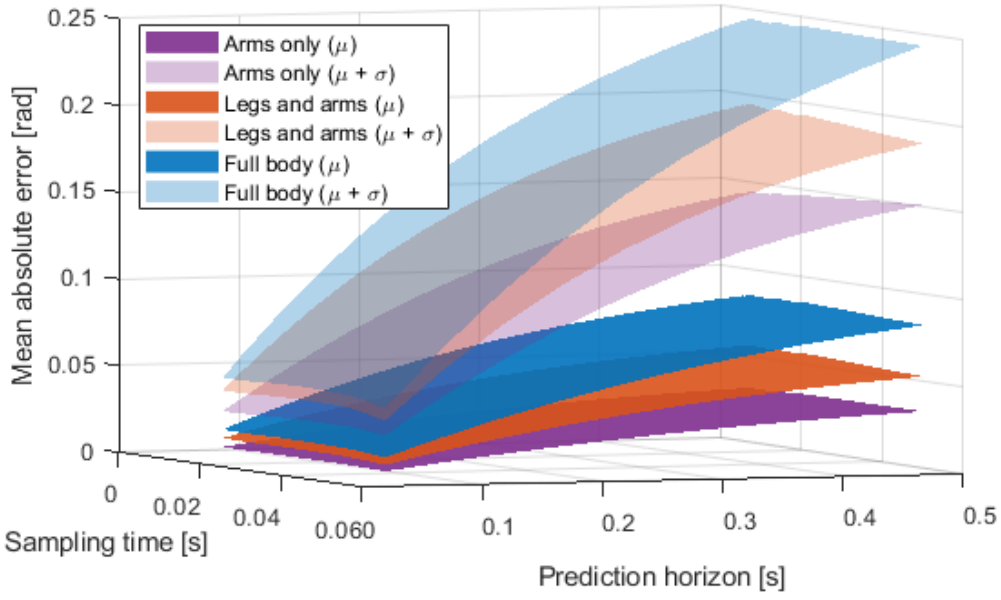

Source: authored

that it is not necessary to instrument an exoskeleton with sensors in non-actuated joints, which is positive in terms of reducing the system complexity. This result also means that the structure of the network itself can be adapted to the exoskeleton on which it will be implemented, creating a variation of the complete model by discarding the unused subnetworks.

The next step involves evaluating how the model performs in adapting to specific tasks, or specific subjects. For that, as explained in Section 4.6, two AMASS sub-datasets are chosen, respectively: BMLhandball and MPI-HDM05. First things first, BMLhandball is used to determine the model's ability to learn a particular class of motion. This is important, for instance, when an exoskeleton is used as assistance during laborious work, such as carrying loads or heavy tools. The universal model, trained on the big *training* dataset (11 sub-datasets), is used as reference. Evaluation runs using all body joints, and a range of 1 up to 10 future frames, computing the mean absolute error and its standard deviation. Thus, it is possible to quantify the overall performance of the model using these two numbers.

The aforementioned procedure is repeated on both the *universal* validation dataset (4 sub-datasets), that contains no specific motion type, and on the whole BMLhandball dataset. This same evaluation is repeated on the models trained on the BMLhandball dataset, with the difference that they follow a 10-fold cross-validation process (HAYKIN, 2009). This implies a total of 10 models, each one trained on 9 of the 10 total subjects, in such a way that each model must be evaluated only on the subject it has not been trained on (unknown data). Results are averaged across all 10 runs. Both model categories - learning from scratch and transfer learning - are also evaluated on the universal validation dataset for comparison purposes. Results are summarized in Table 7.

Table 7 – Mean absolute error and standard deviation (in radians) for different evaluation runs. The BMLhandball dataset illustrates a scenario of predicting a specific type of motion.

Model	**Validation dataset**	
	Universal	BMLhandball
Universal	0.0289 ± 0.0693	0.0186 ± 0.0412
Training from scratch on BMLhandball	0.0318 ± 0.0689	0.0123 ± 0.0243
Transfer learning on BMLhandball	0.0324 ± 0.0713	0.0173 ± 0.0359

The results on Table 7 allow a series of conclusions. First of all, the universal model has the best performance for general purpose tasks (universal validation dataset), and shows satisfactory performance on the particular handball motions of the BML dataset. This proves that the model is suitable for generalization, as it used its previous knowledge of the underlying operation of the human motor system to predict a class of motions it has never seen before. In contrast, both models that were presented with handball motions performed better on the BML dataset, as expected. The transfer learning procedure is

Figure 74 – Example motion from BMLhandball: one fake shot immediately succeeded by the actual shot. Five different subjects are considered, all right-handed. Mean absolute errors (μ) for the corresponding shoulder and elbow joints are shown, evaluated on all three models: the universal, the model trained from scratch and the other obtained via transfer learning. The motion of each subject is predicted by the model it has not been trained on. It uses the full body, a framerate of 120 Hz and a prediction horizon of 50 ms.

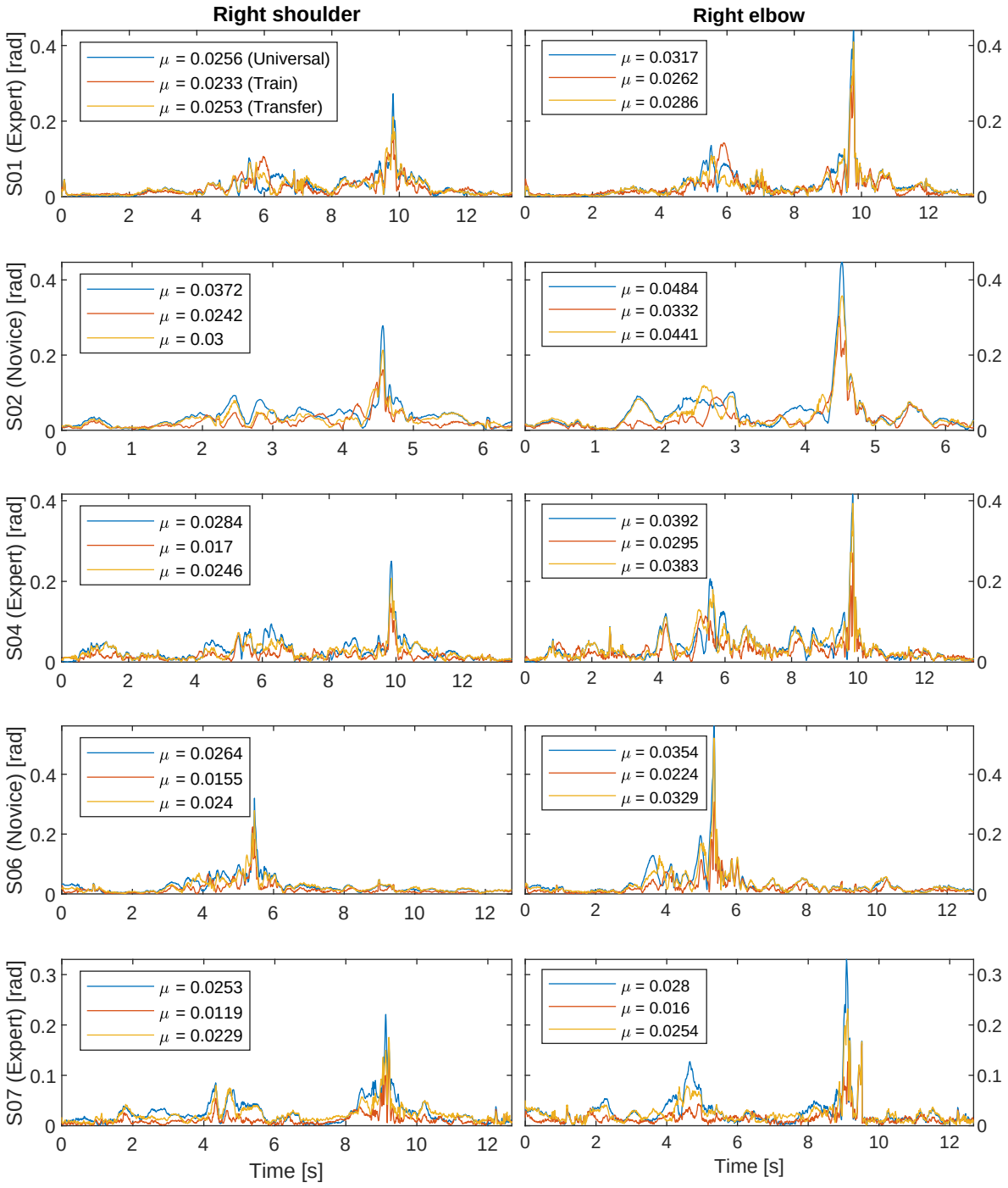

Source: authored

effective for fine-tuning the universal prediction model, at the cost of worse performance on general-purpose motions, with the hyperparameters utilized in the present work. This balance can be tailored to specific scenarios by selecting different learning rates or batch sizes, for example.

Now focusing on the model trained from scratch, it unsurprisingly obtained the best performance on BMLhandball. This might indicate a slight overfit, as the only type of movement it has ever seen are handball motions. What is surprising, besides, is the decent performance on the universal validation dataset, enforcing the generalization capacity of the model with the selected training procedure. It was not able to beat the universal model, however performance is not too different, recalling that the BMLhandball training dataset is much smaller than the universal one, that joins together 11 complete AMASS sub-datasets.

To illustrate these results, Figure 74 shows an example motion of BMLhandball, where one fake shot is immediately succeeded by an actual one, always performed with the right arm. Results are comparable to the statistics shown in Table 7, with the model trained from scratch performing the best, while the transfer learning one performs slightly better than the universal baseline.

Moving on to another type of model specialization, the MPI-HDM05 (MÜLLER et al., 2007) dataset is used to illustrate learning the particular motion patterns of a specific individual. It is of common sense that different persons have varied motion characteristics, influenced by factors such as body structure, gender, and even personality. This use case represents, for instance, a scenario where an exoskeleton is owned and used by a single person, which is becoming increasingly common regarding assistive wearable robots. Like on the previous case, the universal model and its corresponding validation dataset are used as reference, with the MPI-HDM05 recordings containing varied tasks of four subjects. For each procedure - training from scratch and transfer learning - a total of four models are obtained, one for each individual. Results are averaged for comparison and summarized in Table 8.

Table 8 – Mean absolute error and standard deviation (in radians) for different evaluation runs. The MPI-HDM05 dataset illustrates a scenario of predicting motions for a specific subject.

Model	**Validation dataset**	
	Universal	MPI-HDM05
Universal	0.0289 ± 0.0693	0.0314 ± 0.0697
Training from scratch on MPI-HDM05	0.0322 ± 0.0659	0.0269 ± 0.0537
Transfer learning on MPI-HDM05	0.0298 ± 0.0676	0.0311 ± 0.0671

The obtained results follow the trend already observed when using the BMLhandball dataset. Training from scratch on a specific subject always gives the best results, followed

Figure 75 – Example walking motion from MPI-HDM05, from the validation splits. All four subjects from the dataset are considered. Mean absolute errors (μ) for left and right legs (hip, knee and ankle joints) are shown, evaluated on all three models: the universal, the model trained from scratch and the other obtained via transfer learning. It uses the full body, a framerate of 120 Hz and a prediction horizon of 50 ms. Results are shown up to 15 seconds for a clearer visualization, but the mean values comprise each complete recording (around 50 seconds).

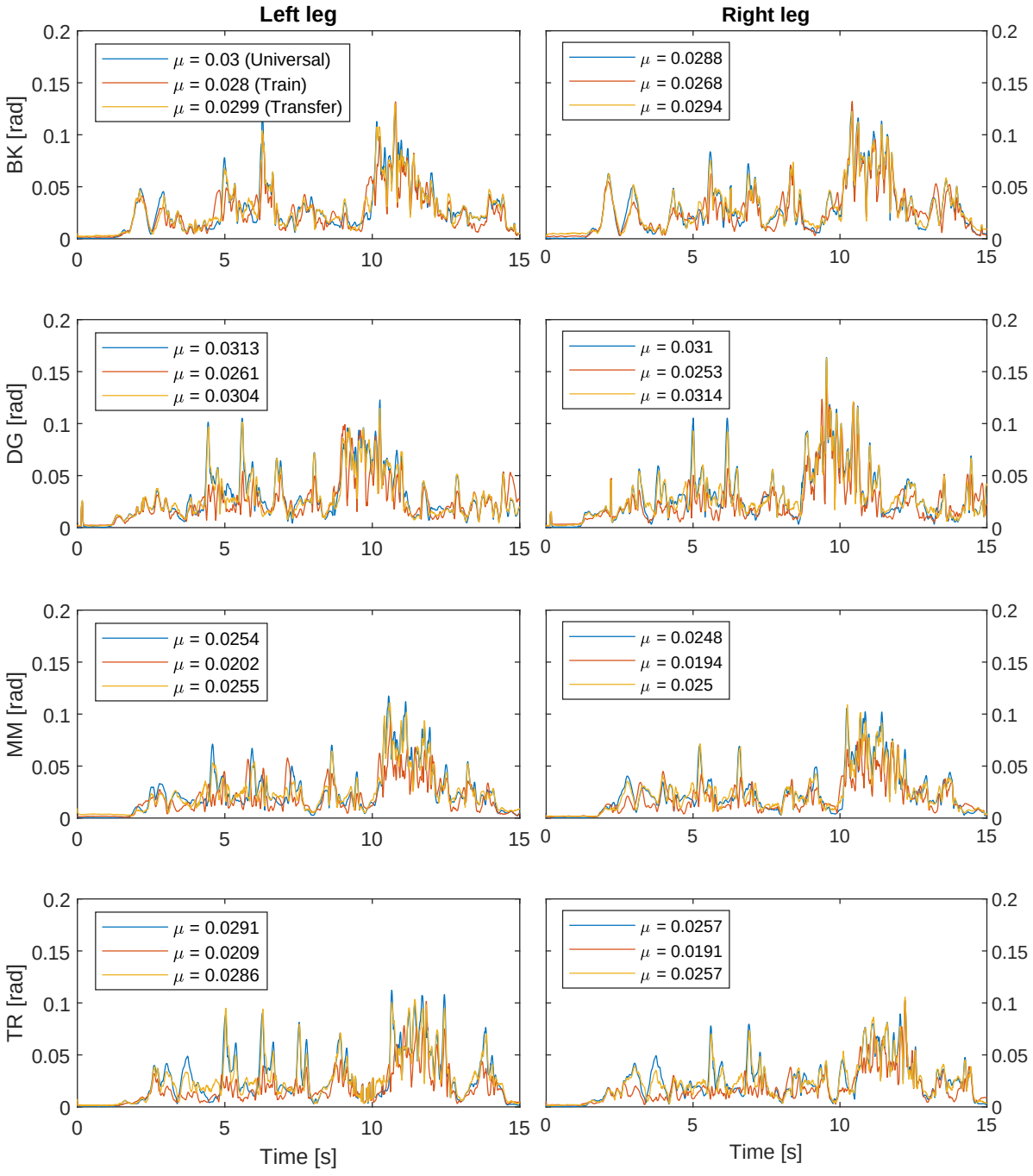

Source: authored

by transfer learning. However, it is not possible to train the model from scratch while the user wears a functional exoskeleton, as the random weight initialization will result in unpredictable behavior, which may injure the user. This is what makes transfer learning particularly useful: an exoskeleton may be factory loaded with a general-purpose model as the one obtained here, which already gives adequate results due to its generalization properties, and it is continuously fine-tuned for its user during normal operation. This type of *online* learning has great potential in achieving high levels of transparency for a single user, which in turn may not be desirable for a wearable robot that is shared between multiple individuals. As before, the example data is shown in Figure 75. The model trained from scratch has again the best performance, while the other two exhibit similar results.

Apart from showing how the HuMAn model is flexible in adapting its predictions to specific motion types or subjects, the last two evaluations were also important to point out that the model generalizes well, even when having only small sets of training data. This situation refers to the competitive performance of the models trained from scratch on the specialized datasets when evaluated on the general validation dataset. Apart from the model structure itself, this can also be attributed to the SWA (IZMAILOV et al., 2018) procedure applied on the last training steps.

Next, it is fundamental to check how fast the model converges to a steady state, achieving a satisfactory interpretation of the actual motion pattern to be predicted. As its recurrent part is initialized with its states filled with zeros, it might take some steps to

Figure 76 – Mean absolute error (μ) isolated and added to its standard deviation (σ) for the universal model. Results are summarized for each time step. The plot clearly shows that the model has no noticeable delays before reaching steady state operation.

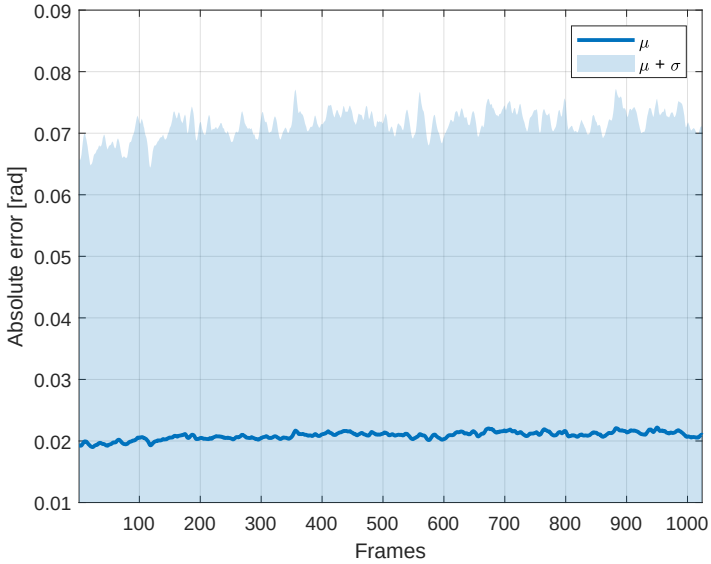

Source: authored

establish these states with meaningful values. This analysis is conducted using the universal model and its corresponding validation dataset, but now with 1024-frames sequences. No distinction is made between different sample rates, thus the temporal axis is represented in number of frames rather than physical time (seconds). The model is evaluated using a range of 1 up to 10 future frames. Results are shown in Figure 76.

The previous results show that the model does not need any warmup time to analyze the motion performed by the subject and start making adequate predictions. In real world conditions, this exact situation happens only when the exoskeleton is first turned on. However, a similar scenario happens when the user suddenly changes its motion pattern, such as alternating between running and walking. This apparent absence of a settling phase makes this prediction algorithm attractive in such situations. To illustrate HuMAn working on a scenario of sudden motions, Figure 77 shows the average absolute

Figure 77 – Example dodging motion from Eyes Japan Dataset. Notice that Eyes Japan is part of the *training* dataset, thus these results are for illustration purposes only, as the model has previously seen these motions during training. The mean absolute error and its corresponding standard deviation are vertically aligned with the average absolute angular displacement, computed with simple finite differences. This example considers the whole skeleton, a framerate of 120 Hz, and a 50 ms horizon. The plot shows that the error spikes right when the sudden motion starts, but adequately drops afterwards.

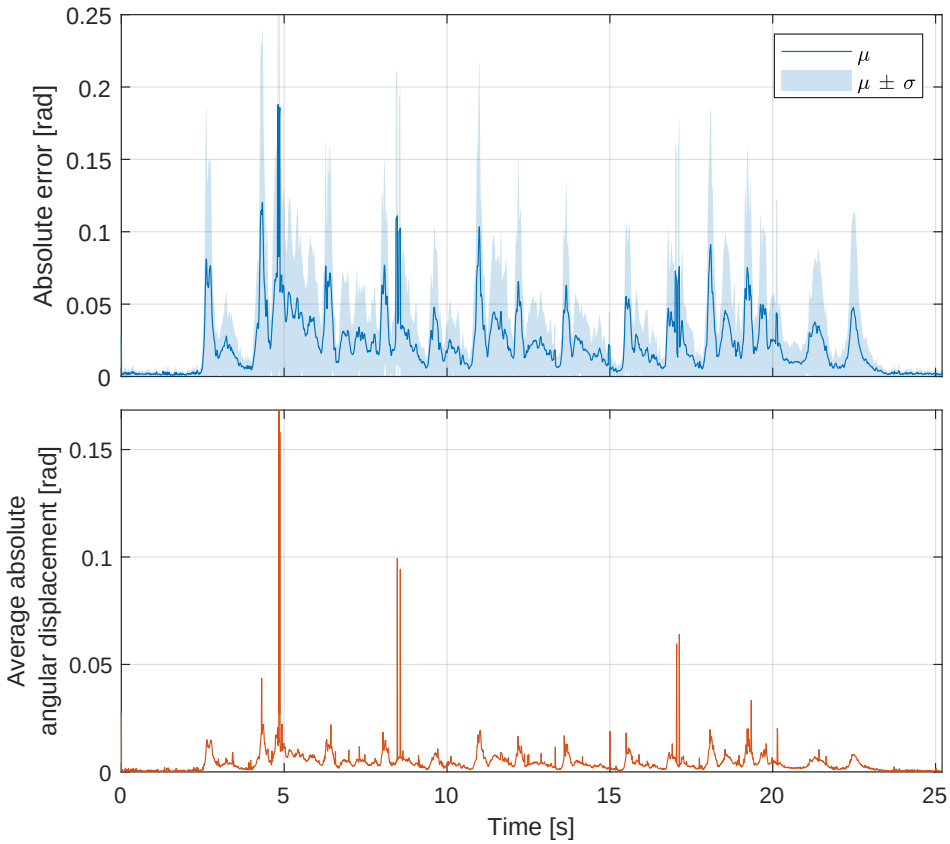

Source: authored

error for a whole body prediction of a recording containing a sequence of dodging motions.

The next analysis will show the distribution of prediction errors under a different perspective, using percent highs and lows. For that, the universal model and validation dataset are used, and the joint set is the complete body. Running predictions for a series of future time horizons ranging up to 0.5 seconds, these are grouped into three bins according to the future horizon, due to the fact that this parameter influences the overall prediction performance, as already discussed. Inside each one of these bins, the computed absolute errors are sorted across all axes (recordings, joints, and time) and split between four sets: 90 % smallest errors, 95 % smallest, 10 % largest and 5 % largest. The average across the whole set is also included as reference. Results are shown in Figure 78.

Figure 78 – Mean absolute errors split into percentage groups for three bins of future prediction horizons. The values on the horizontal axis show the maximum time of each bin.

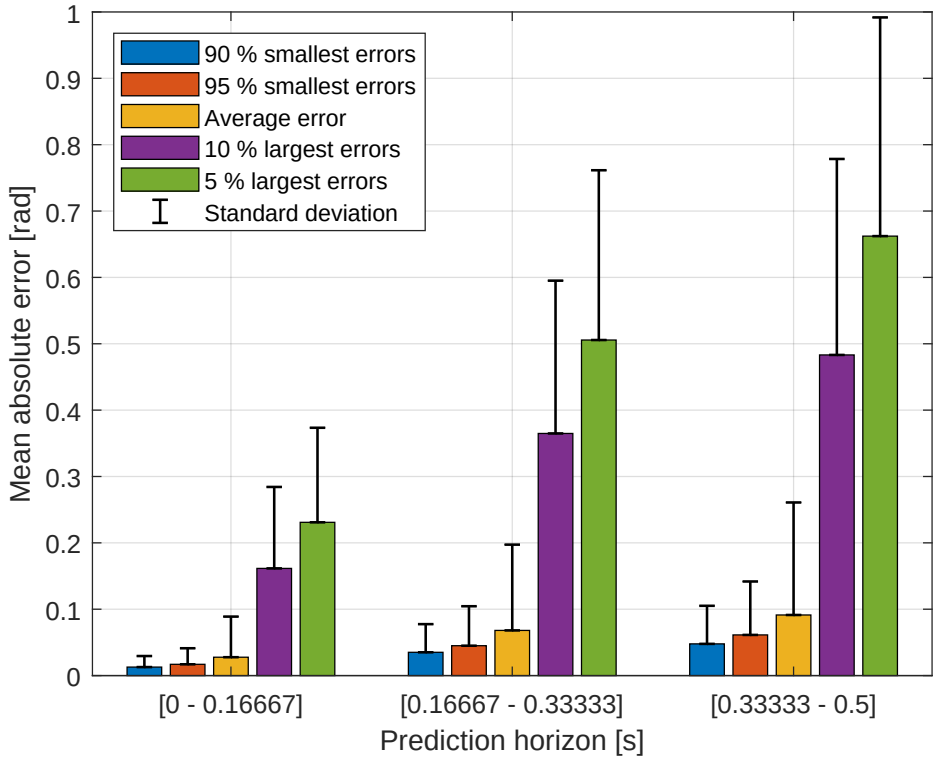

Source: authored

The previous bar graph shows that the vast majority of predictions are generated with very low errors, and just a small fraction yields larger mean absolute errors. As already expected, the overall performance degrades as the prediction horizon is increased. However, these statistics do not show which joints are bringing the greatest challenge to the model. Therefore, this is the object for the next analysis. Starting by generating predictions using the same hyperparameters as before, but continuously averaging the results for each joint, the plot in Figure 79 is created.

The ordered bar plot in Figure 79 comparatively shows how well the model performed, on average, for each anatomical joint. The absence of a particular group of joints (legs or arms, for example) concentrating error values too far from the average shows that there are no clear issues with the proposed model structure (see Subsection 4.4.1).

Figure 79 – Mean absolute error for each body joint, using the validation dataset. The 24 joints refer to the kinematic tree presented in Figure 59.

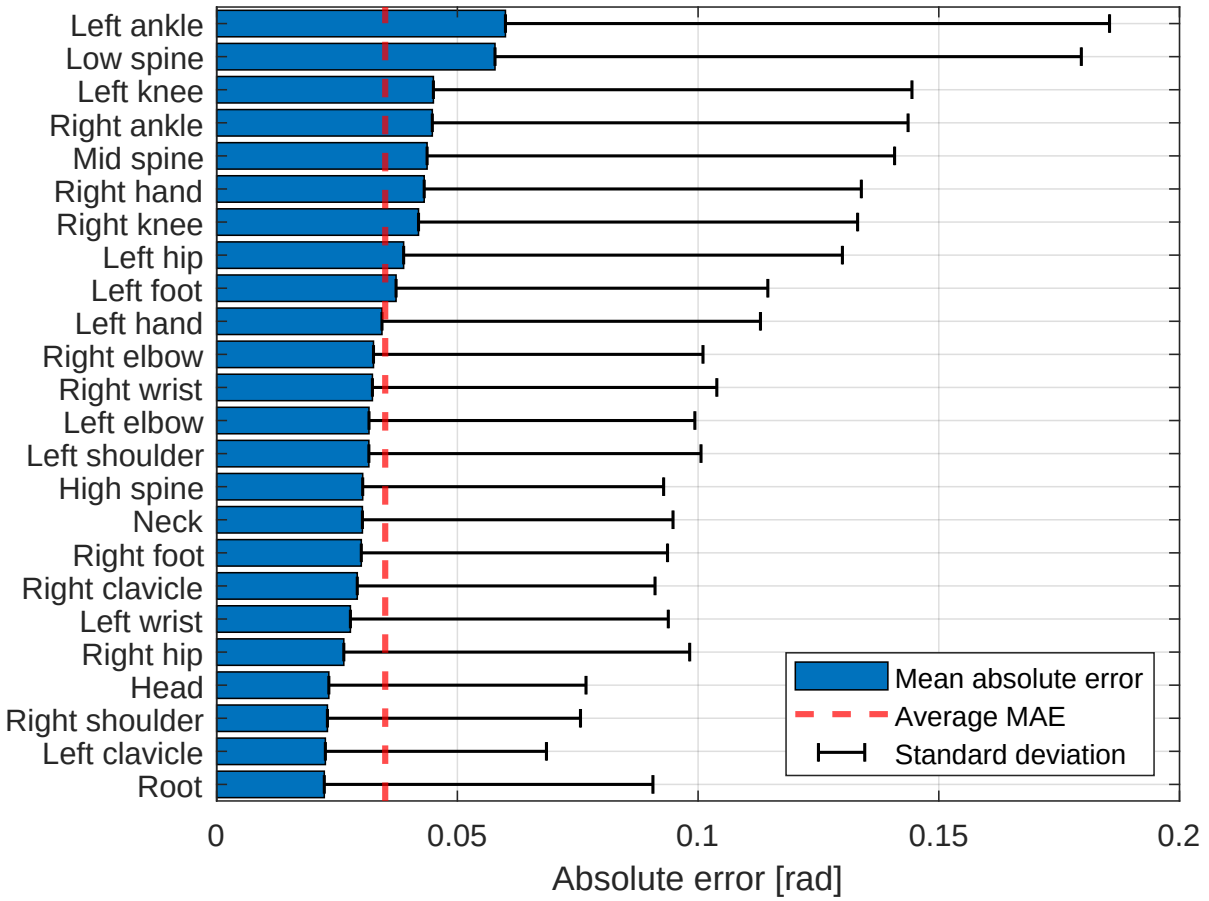

Source: authored

4.9 Closing remarks

This chapter has the objective of changing the *reactive* paradigm present in many control algorithms to an *anticipatory* behavior, aiming at investigating the feasibility of creating an algorithm capable of predicting human body poses in the near future. Moreover, such an algorithm needs to be flexible to a number of extents, enabling it to be used in any type of exoskeleton, with its particular sensory system, and meeting the needs of a varied range of users and their particular motion patterns.

Considering the obtained results, the objectives were successfully achieved. Analyses proved some expected outcomes, such as outputting better predictions for shorter future

time horizons. As mentioned before, human motion is a voluntary process, with anticipatory data available only through monitoring the nervous system (see Section 2.2). In contrast, the proposed prediction strategy, which uses only poses as input, has the clear advantage of being minimally invasive.

Results regarding improved performance when receiving a subset of the whole body as input (refer to page 136) imply that specialized versions of this whole-body model can be straightforwardly created by simply removing the inputs and corresponding joint prediction networks that are not used, together with the whole selection input. This leads to derived models with less parameters, demanding thus less memory and being more easily trainable. Another consequence of this finding is that there is no need to place sensors on areas of the user's body that are not assisted by the exoskeleton[11], reducing overall system complexity. This is a rather counterintuitive result, as human motion is a highly coordinated task; as an example, consider the arm swing motion during walking or running, always in phase with the opposite leg. Measuring such movements could, in theory, benefit related predictions. However, as mentioned before, the algorithm may enhance its predictions by utilizing its recurrent section in a more focused way and with less variability, when given the chance to work with a smaller number of joints.

The proposed algorithm also showed adequate generalization capacity, even in unexpected scenarios such as the ones regarding the BMLhandball (Table 7) and MPI-HDM05 (Table 8) datasets. This result is also due in part to the way training was implemented, specially regarding the SWA (IZMAILOV et al., 2018) procedure. As a result, the model is not prone to memorizing training data, leaving room for performance improvements through added model capacity, provided that suitable hardware is available for training.

It is also worth noting that the AMASS dataset assumes that all anatomical body joints are spherical, with three DoFs each. However, several human joints can be precisely parameterized with a fewer DoF count (see Section 2.3 for examples). As structured prediction algorithms are agnostic to the choice of joint angle representation (AKSAN; KAUFMANN; HILLIGES, 2019), the model can be further simplified by considering a specialized representation for each individual body joint. Principal Components Analysis (SMITH, 2002) is another tool capable of reducing the dimensionality of anatomical motion representation (MATRONE; CIPRIANI; SECCO, et al., 2010; MATRONE; CIPRIANI; CARROZZA, et al., 2012).

Last but not least, all the code used for this study is freely available from https://github.com/Vtn21/HuMAn, under the MIT license.

[11] From the perspective of this prediction algorithm in isolation. Other systems that compose the overall operation of an exoskeleton may greatly benefit from whole-body data, such as the postural stability methods described in Section 2.7.

5 CONCLUSION AND FUTURE WORKS

Exoskeleton robots already are a tangible reality, still limited to specific use cases or as an academic research subject, while being an area under active development and with great potential of positively influencing the lives of many human beings. Such robots always have the same central objective: to assist humans in activities that involve physical motion. However, the manner in which such assistance is provided may vary; rehabilitation patients, for example, have the exoskeleton delivering most of the motion power, while imposing healthy motion patterns to empower recovery. People with disabilities or paralysis rely on the exoskeleton to turn their motion intent - usually obtained from neural activity monitoring - into mechanical power. Other than that, subjects with sufficient muscular authority are responsible for providing the robot with the desired motion patterns, which must be replicated in a synchronized manner, minimizing spurious interaction forces, achieving thus a *transparent* behavior.

This work contributes to the topic of transparent exoskeletons by first proposing mechanical design principles capable of respecting the natural anatomy of the human body, and allowing the user to cover the complete workspace of each body joint while wearing the exoskeleton. Instead of just using rotational joints on the sagittal plane, it is possible to experiment with many types of geometries and actuation systems that better interact with the human body. For that, human biomechanics must be considered at the design phase, and optimization methods are great tools to orient sensible design choices.

After designing any wearable robot, stably attaching it to its user is not a trivial task. Exoskeletons are mainly attached on top of the skin, which is an uneven surface composed by soft tissues, lacking features that would allow for extremely precise positioning of attachment points. In addition to that, each person has a particular body shape and stiffness. This work also proposes a novel solution, based upon a rigid attachment with a ratcheting fixture, that makes the transmission of forces more efficient, while also being extremely easy to wear, adjust, and remove.

Future works regarding the mechanical design topic involve further enhancing the body fixture, by exploring personalized fixtures through 3D scanning and printing or molding techniques, integrated with the ratcheting fixture. This is an important step towards user friendliness and comfort, while also mitigating undesirable events such as attachment slippage. Next, the proposed external joint designs can be upgraded to actuated versions, and receive sensors to monitor important variables such as interaction forces between the user and the attachment. The proposed design principles, as well as the optimization procedures, are also capable of being used for creating external joints that assist other areas of the human body.

User-centered mechanical exoskeleton design is an essential foundation for achieving transparency, but certainly is not enough. Such a robot must be equipped with specialized control algorithms capable of closely following the motion trajectories voluntarily generated by the human user. Regarding this topic, the present work proposes a universal and flexible motion prediction algorithm, *HuMAn*, capable of predicting motion at short future time horizons. Such anticipatory data can be used as inputs for trajectory-tracking controllers such as model-based feedforward, enabling the robot to achieve greater synchronism with the motion of its user.

The *HuMAn* algorithm also proved itself effective in adapting to specific motion patterns via a transfer learning approach, which is positive in terms of, e.g., continuously enhancing the transparency perceived by a specific user. Next, evaluation results showed that it is possible to create compact versions of the algorithm, for specific exoskeleton structures. This enables obtaining simpler and more compact algorithms, which are more resource-efficient at both training and deployment stages.

Future steps for enhancing the applicability of motion prediction in exoskeleton transparency include effectively creating a fork of *HuMAn*, removing the selection input and using only the joint angle inputs and prediction subnetworks corresponding to a specific exoskeleton structure. The input dimensionality can be further reduced by exploiting the individual mechanical workspace characteristics of each anatomical joint and using PCA on the input data. Then, the algorithm can be integrated with several types of transparency-oriented controllers, enabling tuning of specific parameters such as the prediction horizon, directly related to the optimal anticipation required by the actuation systems.

The joint pose data demanded by the prediction algorithm, in real-world usage scenarios, comes from a variety of embedded sensory systems. A promising algorithm to treat such data is the Unscented Kalman Filter (JULIER; UHLMANN, 1997; WAN; VAN DER MERWE, 2000), that improves accuracy for nonlinear systems while maintaining the computational complexity of its predecessor, the Extended Kalman Filter. This state estimation algorithm can be integrated with the RNN-based prediction (LI; ZHOU; LIU, 2021), seeking further enhancements in prediction capability and sensor data interpretation.

Of course, transparent behavior is an attractive feature for assistive exoskeletons, but it has to be used wisely. It makes no sense to have a robot that behaves strictly transparently when the user is losing dynamic balance, as this can lead to a fall and consequent safety issues. As such, a wearable robot, especially the ones aimed at assisting locomotion, must continuously monitor the stability of the coupled bipedal system and use such information to modulate its own behavior. As soon as a situation of poor stability occurs, the exoskeleton must trigger a more active operation, helping its user to regain balance and, once the indicators are adequate again, return to a more transparent mode. In other words, postural stability must govern the high-level objective of the control system,

continuously ranging between transparency and active balance recovery.

To sum up, ergonomic and transparent exoskeletons are achieved through combination of many diverse aspects and design choices. The present work aimed at addressing topics related to mechanical design and human motion prediction, that are some of the key components of this type of robotic system. The advancement of such technologies is a clear step towards greater use of assistive robotics on behalf of people's lives, health, and work.

REFERENCES

ABADI, Martín et al. **TensorFlow: Large-Scale Machine Learning on Heterogeneous Systems**. 2015. Software available from tensorflow.org. Available from: https://www.tensorflow.org/.

ABU-TAIEH, E. An Algorithm for Human Modeling in Information Technology Multimedia Using Human Biometrics Found in Golden Ratio, Vitruvian Man and Neufert. In: 2015 Fifth International Conference on e-Learning (econf). 2015. P. 65–73.

ACCOTO, Dino; CARPINO, Giorgio, et al. Design and characterization of a novel high-power series elastic actuator for a lower limb robotic orthosis. **International Journal of Advanced Robotic Systems**, SAGE Publications Sage UK: London, England, v. 10, n. 10, p. 359, 2013.

ACCOTO, Dino; SERGI, Fabrizio, et al. Robomorphism: A Nonanthropomorphic Wearable Robot. **IEEE Robotics Automation Magazine**, v. 21, n. 4, p. 45–55, 2014. DOI: 10.1109/MRA.2014.2360276.

ACKERMANN, Marko; VAN DEN BOGERT, Antonie J. Optimality principles for model-based prediction of human gait. **Journal of biomechanics**, Elsevier, v. 43, n. 6, p. 1055–1060, 2010.

AEYELS, B. et al. An EMG-based finite state approach for a microcomputer-controlled above-knee prosthesis. In: PROCEEDINGS of 17th International Conference of the Engineering in Medicine and Biology Society. Sept. 1995. v. 2, p. 1315–1316. DOI: 10.1109/IEMBS.1995.579704.

AGUIRRE-OLLINGER, Gabriel et al. Inertia compensation control of a one-degree-of-freedom exoskeleton for lower-limb assistance: Initial experiments. **IEEE Transactions on Neural Systems and Rehabilitation Engineering**, IEEE, v. 20, n. 1, p. 68–77, 2012.

AKHTER, Ijaz; BLACK, Michael J. Pose-Conditioned Joint Angle Limits for 3D Human Pose Reconstruction. In: IEEE Conf. on Computer Vision and Pattern Recognition (CVPR) 2015. June 2015.

AKSAN, Emre; KAUFMANN, Manuel; HILLIGES, Otmar. Structured Prediction Helps 3D Human Motion Modelling. In: THE IEEE International Conference on Computer Vision (ICCV). Oct. 2019. First two authors contributed equally.

ALAMI, R. et al. Safe and dependable physical human-robot interaction in anthropic domains: State of the art and challenges. In: 2006 IEEE/RSJ International Conference on Intelligent Robots and Systems. Oct. 2006. P. 1–16. DOI: 10.1109/IROS.2006.6936985.

ALPINESTARS. **Bionic-7 Knee Brace Set**. 2021. https://www.alpinestars.com/collections/mx-protection/products/bionic-7-knee-brace-set. [Online; accessed 17-May-2021].

ATALAY, Asli et al. Batch fabrication of customizable silicone-textile composite capacitive strain sensors for human motion tracking. **Advanced Materials Technologies**, Wiley Online Library, v. 2, n. 9, p. 1700136, 2017.

BAKER, L. et al. Ankle optimization with a soft exosuit reduces metabolic cost of loaded walking. In: 2017 International Symposium on Wearable Robotics and Rehabilitation (WeRob). Nov. 2017. P. 1–1. DOI: 10.1109/WEROB.2017.8383857.

BALANCE. **Extended Stability Index**. 2015. European Union's Seventh Programme for research, technological development and demonstration. Available from: https://arquivo.pt/wayback/20170603133719mp_/http://www.balance-fp7.eu/private_area/archivo.php?archivo=17.

_____. **Report "Stability Index"**. 2014. European Union's Seventh Programme for research, technological development and demonstration. Available from: https://arquivo.pt/wayback/20170603134040mp_/http://www.balance-fp7.eu/private_area/archivo.php?archivo=15.

BANALA, Sai K. et al. Robot assisted gait training with active leg exoskeleton (ALEX). **IEEE transactions on neural systems and rehabilitation engineering**, IEEE, v. 17, n. 1, p. 2–8, 2008.

BAPAT, Ganesh M.; SUJATHA, S. A Method for Optimal Synthesis of a Biomimetic Four-Bar Linkage Knee Joint for a Knee-Ankle-Foot Orthosis. **Journal of Biomimetics, Biomaterials and Biomedical Engineering**, v. 32, p. 20–28, July 2017. DOI: 10.4028/www.scientific.net/JBBBE.32.20.

BARIN, K. Dynamic posturography: analysis of error in force plate measurement of postural sway. **IEEE Engineering in Medicine and Biology Magazine**, v. 11, n. 4, p. 52–56, Dec. 1992. ISSN 1937-4186. DOI: 10.1109/51.256960.

BARNETT-COWAN, Michael; HARRIS, Laurence R. Perceived timing of vestibular stimulation relative to touch, light and sound. **Experimental Brain Research**, v. 198, n. 2, p. 221–231, 1 Sept. 2009. ISSN 1432-1106. DOI: 10.1007/s00221-009-1779-4.

BEJARANO, Noelia Chia et al. A novel adaptive, real-time algorithm to detect gait events from wearable sensors. **IEEE transactions on neural systems and rehabilitation engineering**, IEEE, v. 23, n. 3, p. 413–422, 2014.

BERNER, Christopher et al. Dota 2 with large scale deep reinforcement learning. **arXiv preprint arXiv:1912.06680**, 2019.

BERTOMEU, José María Baydal et al. Development of a hinge compatible with the kinematics of the knee joint. **Prosthetics and Orthotics International**, v. 31, n. 4, p. 371–383, 2007. PMID: 18050008. DOI: 10.1080/03093640601095842. eprint: https://doi.org/10.1080/03093640601095842.

BERTRAM, John E. A.; RUINA, Andy. Multiple walking speed–frequency relations are predicted by constrained optimization. **Journal of theoretical Biology**, Elsevier, v. 209, n. 4, p. 445–453, 2001.

BIEWENER, A. A.; PATEK, S. N. **Animal Locomotion**. Oxford University Press, 2018. ISBN 9780198743156. Available from: https://books.google.com.br/books?id=nLNSDwAAQBAJ.

BILRO, Lúcia et al. Optical sensors based on plastic fibers. **Sensors**, Molecular Diversity Preservation International, v. 12, n. 9, p. 12184–12207, 2012.

BLAYA, J. A.; HERR, H. Adaptive control of a variable-impedance ankle-foot orthosis to assist drop-foot gait. **IEEE Transactions on Neural Systems and Rehabilitation Engineering**, v. 12, n. 1, p. 24–31, Mar. 2004. ISSN 1558-0210. DOI: 10.1109/TNSRE.2003.823266.

BLICKHAN, Reinhard. The spring-mass model for running and hopping. **Journal of biomechanics**, Elsevier Science, v. 22, n. 11-12, p. 1217–1227, 1989.

BOAVENTURA, Thiago. **Hydraulic compliance control of the quadruped robot HyQ**. 2013. PhD thesis – University of Genoa and Istituto Italiano di Tecnologia.

BOAVENTURA, Thiago; BUCHLI, Jonas. Acceleration-based transparency control framework for wearable robots. In: IEEE. 2016 IEEE/RSJ International Conference on Intelligent Robots and Systems (IROS). 2016. P. 5683–5688.

BOAVENTURA, Thiago; HAMMER, Lisa; BUCHLI, Jonas. Interaction force estimation for transparency control on wearable robots using a kalman filter. In: CONVERGING clinical and engineering research on neurorehabilitation II. Springer, 2017. P. 489–493.

BOHNE, Michael. **The effects of hiking downhill using two trekking poles while carrying different external loads in a backpack**. 2005. PhD thesis – University of Northern Colorado.

BORN, Dennis-Peter; SPERLICH, Billy; HOLMBERG, Hans-Christer. Bringing Light into the Dark: Effects of Compression Clothing on Performance and Recovery. **International Journal of Sports Physiology and Performance**, Human Kinetics, Inc., Champaign IL, USA, v. 8, n. 1, p. 4–18, 2013. Available from: https://journals.humankinetics.com/view/journals/ijspp/8/1/article-p4.xml.

BOZINOVSKI, Stevo. Reminder of the First Paper on Transfer Learning in Neural Networks, 1976. **Informatica**, v. 44, n. 3, 2020.

BREG. **Wee ROM Post-Op**. 2019. https://www.breg.com/products/pediatric/knee/wee-rom-post-op/. [Online; accessed 17-May-2021].

BRUIJN, Sjoerd et al. Assessing the stability of human locomotion: a review of current measures. **Journal of the Royal Society Interface**, The Royal Society, v. 10, n. 83, p. 20120999, 2013.

_____. The effects of arm swing on human gait stability. **Journal of Experimental Biology**, The Company of Biologists Ltd, v. 213, n. 23, p. 3945–3952, 2010. ISSN 0022-0949. DOI: 10.1242/jeb.045112. eprint: https://jeb.biologists.org/content/213/23/3945.full.pdf. Available from: https://jeb.biologists.org/content/213/23/3945.

CAI, Viet Anh Dung et al. Self-adjustment mechanisms and their application for orthosis design. **Meccanica**, Springer, v. 52, n. 3, p. 713–728, 2017.

CALDAS, Rafael et al. A systematic review of gait analysis methods based on inertial sensors and adaptive algorithms. **Gait & posture**, Elsevier, v. 57, p. 204–210, 2017.

CARON, Robert R. et al. Musculoskeletal stiffness changes linearly in response to increasing load during walking gait. **Journal of biomechanics**, Elsevier, v. 48, n. 6, p. 1165–1171, 2015.

CHAICHAOWARAT, Ronnapee; GRANADOS, Diego Felipe Paez, et al. Passive knee exoskeleton using torsion spring for cycling assistance. In: IEEE. 2017 IEEE/RSJ International Conference on Intelligent Robots and Systems (IROS). 2017. P. 3069–3074.

CHAICHAOWARAT, Ronnapee; KINUGAWA, Jun; KOSUGE, Kazuhiro. Cycling-enhanced knee exoskeleton using planar spiral spring. In: IEEE. 2018 40th Annual International Conference of the IEEE Engineering in Medicine and Biology Society (EMBC). 2018. P. 1–6.

CHAUDHARI, Pratik; SOATTO, Stefano. Stochastic gradient descent performs variational inference, converges to limit cycles for deep networks. In: IEEE. 2018 Information Theory and Applications Workshop (ITA). 2018. P. 1–10.

CHO, Kyunghyun et al. Learning phrase representations using RNN encoder-decoder for statistical machine translation. **arXiv preprint arXiv:1406.1078**, 2014.

CHU, A.; KAZEROONI, H.; ZOSS, A. On the Biomimetic Design of the Berkeley Lower Extremity Exoskeleton (BLEEX). In: PROCEEDINGS of the 2005 IEEE International Conference on Robotics and Automation. Apr. 2005. P. 4345–4352. DOI: 10.1109/ROBOT.2005.1570789.

CHUNG, Junyoung et al. Empirical evaluation of gated recurrent neural networks on sequence modeling. **arXiv preprint arXiv:1412.3555**, 2014.

CLEVERT, Djork-Arné; UNTERTHINER, Thomas; HOCHREITER, Sepp. Fast and accurate deep network learning by exponential linear units (elus). **arXiv preprint arXiv:1511.07289**, 2015.

CMU. **CMU Graphics Lab Motion Capture Database**. 2000. Online. Available from: http://mocap.cs.cmu.edu/.

COLOMBO, Gery et al. Treadmill training of paraplegic patients using a robotic orthosis. **Journal of rehabilitation research and development**, Citeseer, v. 37, n. 6, p. 693–700, 2000.

COROS, Stelian; BEAUDOIN, Philippe; PANNE, Michiel van de. Generalized Biped Walking Control. In: ACM SIGGRAPH 2010 Papers. Los Angeles, California: Association for Computing Machinery, 2010. (SIGGRAPH). ISBN 9781450302104. DOI: 10.1145/1833349.1781156.

CSÁJI, Balázs Csanád et al. Approximation with artificial neural networks. **Faculty of Sciences, Etvs Lornd University, Hungary**, Citeseer, v. 24, n. 48, p. 7, 2001.

DARWIN, C. **On the Origin of Species by Means of Natural Selection; Or, The Preservation of Favoured Races in the Struggle for Life**. D. Appleton and Company, 1864. Available from: https://books.google.com.br/books?id=HIo5AAAAcAAJ.

DIJK, W. van; KOOIJ, H. van der, et al. Improving the transparency of a rehabilitation robot by exploiting the cyclic behaviour of walking. In: 2013 IEEE 13th International Conference on Rehabilitation Robotics (ICORR). 2013. P. 1–8. DOI: 10.1109/ICORR.2013.6650393.

DIJK, Wietse van; KOOIJ, Herman van der. Optimization of human walking for exoskeletal support. In: 2013 IEEE 13th International Conference on Rehabilitation Robotics (ICORR). 2013. P. 1–6. DOI: 10.1109/ICORR.2013.6650394.

DINGWELL, Jonathan B.; CUSUMANO, Joseph P. Nonlinear time series analysis of normal and pathological human walking. **Chaos: An Interdisciplinary Journal of Nonlinear Science**, American Institute of Physics, v. 10, n. 4, p. 848–863, 2000.

DU, X.; VASUDEVAN, R.; JOHNSON-ROBERSON, M. Bio-LSTM: A Biomechanically Inspired Recurrent Neural Network for 3-D Pedestrian Pose and Gait Prediction. **IEEE Robotics and Automation Letters**, v. 4, n. 2, p. 1501–1508, 2019. DOI: 10.1109/LRA.2019.2895266.

DUDANI, Sahibsingh A. The distance-weighted k-nearest-neighbor rule. **IEEE Transactions on Systems, Man, and Cybernetics**, IEEE, n. 4, p. 325–327, 1976.

DUYSENS, Jacques; FORNER-CORDERO, Arturo. Walking with perturbations: a guide for biped humans and robots. **Bioinspiration & biomimetics**, IOP Publishing, v. 13, n. 6, p. 061001, 2018.

ENGLSBERGER, Johannes et al. Bipedal walking control based on capture point dynamics. In: IEEE. 2011 IEEE/RSJ International Conference on Intelligent Robots and Systems. 2011. P. 4420–4427.

EVANS, E. Burke et al. Experimental immobilization and remobilization of rat knee joints. **JBJS**, LWW, v. 42, n. 5, p. 737–758, 1960.

FAN, Y.; YIN, Y. Mechanism design and motion control of a parallel ankle joint for rehabilitation robotic exoskeleton. In: 2009 IEEE International Conference on Robotics and Biomimetics (ROBIO). Dec. 2009. P. 2527–2532. DOI: 10.1109/ROBIO.2009.5420488.

FERRIS, Daniel P.; SAWICKI, Gregory S.; DALEY, Monica A. A physiologist's perspective on robotic exoskeletons for human locomotion. **International Journal of Humanoid Robotics**, World Scientific, v. 4, n. 03, p. 507–528, 2007.

FLEISCHER, C.; HOMMEL, G. A Human–Exoskeleton Interface Utilizing Electromyography. **IEEE Transactions on Robotics**, v. 24, n. 4, p. 872–882, Aug. 2008. ISSN 1941-0468. DOI: 10.1109/TRO.2008.926860.

FORNARIS, Emile; AUBERT, Marc. Le légionnaire romain, cet athlète méconnu. **Histoire des sciences médicales**, v. 32, p. 161–168, 1998.

FORNER-CORDERO, A.; KOOPMAN, H. J. F. M.; HELM, Frans C. T. van der. Mechanical model of the recovery from stumbling. **Biological Cybernetics**, Springer, v. 91, n. 4, p. 212–220, 2004.

FORNER-CORDERO, A.; KOOPMAN, H. J. F. M.; VAN DER HELM, F. C. T. Describing gait as a sequence of states. **Journal of biomechanics**, Elsevier, v. 39, n. 5, p. 948–957, 2006.

FORNER-CORDERO, A.; KOOPMAN, Hubertus F. J. M.; VAN DER HELM, F. C. T. Mechanical model of the recovery reaction from stumbling: effect of step length on trunk control. **Journal of the Brazilian Society of Mechanical Sciences and Engineering**, Springer, v. 36, n. 3, p. 491–500, 2014.

FORTH, Katharine E.; FIEDLER, Matthew J.; PALOSKI, William H. Estimating functional stability boundaries for bipedal stance. **Gait & posture**, Elsevier, v. 33, n. 4, p. 715–717, 2011.

FRAGKIADAKI, Katerina et al. Recurrent network models for human dynamics. In: PROCEEDINGS of the IEEE International Conference on Computer Vision. 2015. P. 4346–4354.

FRANKLIN, G.F.; POWELL, J.D.; EMAMI-NAEINI, A. **Feedback Control of Dynamic Systems**. Pearson, 2015. (Always Learning). ISBN 9781292068909. Available from: https://books.google.com.br/books?id=yO2hoAEACAAJ.

GALLE, Samuel et al. Adaptation to walking with an exoskeleton that assists ankle extension. **Gait & posture**, Elsevier, v. 38, n. 3, p. 495–499, 2013.

_____. Enhancing performance during inclined loaded walking with a powered ankle–foot exoskeleton. **European journal of applied physiology**, Springer, v. 114, n. 11, p. 2341–2351, 2014.

GALLEGO, J. A. et al. Detection of gait perturbations based on proprioceptive information. Application to Limit Cycle Walkers. **Applied Bionics and Biomechanics**, IOS Press, v. 9, n. 2, p. 205–220, 2012.

GAMS, Andrej et al. On-line learning and modulation of periodic movements with nonlinear dynamical systems. **Autonomous robots**, Springer, v. 27, n. 1, p. 3–23, 2009.

GEORGOPOULOS, A. P.; KALASKA, J. F., et al. On the relations between the direction of two-dimensional arm movements and cell discharge in primate motor cortex. **Journal of Neuroscience**, Society for Neuroscience, v. 2, n. 11, p. 1527–1537, 1982. ISSN 0270-6474. DOI: 10.1523/JNEUROSCI.02-11-01527.1982. eprint: https://www.jneurosci.org/content/2/11/1527.full.pdf. Available from: https://www.jneurosci.org/content/2/11/1527.

GEORGOPOULOS, A. P.; SCHWARTZ, A. B.; KETTNER, R. E. Neuronal population coding of movement direction. **Science**, American Association for the Advancement of Science, v. 233, n. 4771, p. 1416–1419, 1986. ISSN 0036-8075. DOI: 10.1126/science.3749885. eprint: https://science.sciencemag.org/content/233/4771/1416.full.pdf. Available from: https://science.sciencemag.org/content/233/4771/1416.

GEURTSEN, J. B. et al. A model for the description of the standing man and his dynamic behaviour. **Agressologie**, v. 17, p. 63–69, 1975.

GEYER, Hartmut; HERR, Hugh. A muscle-reflex model that encodes principles of legged mechanics produces human walking dynamics and muscle activities. **IEEE Transactions on neural systems and rehabilitation engineering**, IEEE, v. 18, n. 3, p. 263–273, 2010.

GHOSH, Partha et al. Learning human motion models for long-term predictions. In: IEEE. 2017 International Conference on 3D Vision (3DV). 2017. P. 458–466.

GLACKIN, Cornelius et al. Gait trajectory prediction using Gaussian process ensembles. In: IEEE. 2014 IEEE-RAS International Conference on Humanoid Robots. 2014. P. 628–633.

GOUGH, V. E. Contribution to discussion of papers on research in automobile stability, control and tyre performance. **Proc. of Auto Div. Inst. Mech. Eng.**, v. 171, p. 392–395, 1957. Available from: https://ci.nii.ac.jp/naid/10030209099/en/.

_____. Universal tyre test machine. **Proc. FISITA 9th Int. Technical Congr., London, 1962**, p. 117–137, 1962. Available from: https://ci.nii.ac.jp/naid/10025775762/en/.

GRIMMER, Martin et al. Comparison of Ankle Moment Inspired and Ankle Positive Power Inspired Controllers for a Multi-Articular Soft Exosuit for Walking Assistance. In: WEARABLE Robotics: Challenges and Trends. Springer, 2017. P. 337–341.

HASSON, Christopher J.; VAN EMMERIK, Richard E. A.; CALDWELL, Graham E. Predicting dynamic postural instability using center of mass time-to-contact information. **Journal of biomechanics**, Elsevier, v. 41, n. 10, p. 2121–2129, 2008.

HAUSDORFF, Jeffrey M. et al. Is walking a random walk? Evidence for long-range correlations in stride interval of human gait. **Journal of applied physiology**, v. 78, n. 1, p. 349–358, 1995.

HAYES, M. H. **Statistical Digital Signal Processing and Modeling**. Wiley India Pvt. Limited, 2009. ISBN 9788126516100. Available from: https://books.google.com.br/books?id=z0GqhOe9GNQC.

HAYKIN, S. S. **Neural Networks and Learning Machines**. Prentice Hall, 2009. (Neural networks and learning machines, v. 10). ISBN 9780131471399. Available from: https://books.google.com.br/books?id=K7P36lKzI%5C_%7BQ%7D%7BC%7D.

HE, Kaiming et al. Deep residual learning for image recognition. In: PROCEEDINGS of the IEEE conference on computer vision and pattern recognition. 2016. P. 770–778.

_____. Delving deep into rectifiers: Surpassing human-level performance on imagenet classification. In: PROCEEDINGS of the IEEE international conference on computer vision. 2015. P. 1026–1034.

HENDRYCKS, Dan; GIMPEL, Kevin. Gaussian error linear units (gelus). **arXiv preprint arXiv:1606.08415**, 2016.

HIDLER, Joseph M.; WALL, Anji E. Alterations in muscle activation patterns during robotic-assisted walking. **Clinical Biomechanics**, Elsevier, v. 20, n. 2, p. 184–193, 2005.

HOBBELEN, Daan G. E.; WISSE, Martijn. A Disturbance Rejection Measure for Limit Cycle Walkers: The Gait Sensitivity Norm. **IEEE Transactions on Robotics**, v. 23, n. 6, p. 1213–1224, 2007. DOI: 10.1109/TRO.2007.904908.

HOCHREITER, Sepp; SCHMIDHUBER, Jürgen. LSTM can solve hard long time lag problems. In: ADVANCES in neural information processing systems. 1997. P. 473–479.

HOF, A. L.; GAZENDAM, M. G. J.; SINKE, W. E. The condition for dynamic stability. **Journal of biomechanics**, Elsevier, v. 38, n. 1, p. 1–8, 2005.

HOF, At L. The extrapolated center of mass concept suggests a simple control of balance in walking. **Human movement science**, Elsevier, v. 27, n. 1, p. 112–125, 2008.

HOF, At L.; BOCKEL, Renske M. van, et al. Control of lateral balance in walking: experimental findings in normal subjects and above-knee amputees. **Gait & posture**, Elsevier, v. 25, n. 2, p. 250–258, 2007.

HORAK, Fay B.; NASHNER, Lewis M. Central programming of postural movements: adaptation to altered support-surface configurations. **Journal of neurophysiology**, v. 55, n. 6, p. 1369–1381, 1986.

HOYET, Ludovic et al. Sleight of hand: perception of finger motion from reduced marker sets. In: PROCEEDINGS of the ACM SIGGRAPH symposium on interactive 3D graphics and games. 2012. P. 79–86.

HOYLE, F. **The Black Cloud**. Penguin, 1961. Available from: https://books.google.com.br/books?id=18qyxAEACAAJ.

HSIEH, Hwa-Hsin; WALKER, P. S. Stabilizing mechanisms of the loaded and unloaded knee joint. **The Journal of bone and joint surgery. American volume**, v. 58, n. 1, p. 87–93, 1976.

HUANG, Gao; LIU, Zhuang, et al. Densely connected convolutional networks. In: PROCEEDINGS of the IEEE conference on computer vision and pattern recognition. 2017. P. 4700–4708.

HUANG, Yinghao; KAUFMANN, Manuel, et al. Deep Inertial Poser Learning to Reconstruct Human Pose from SparseInertial Measurements in Real Time. **ACM Transactions on Graphics, (Proc. SIGGRAPH Asia)**, v. 37, n. 6, p. 1–15, Nov. 2018.

HURMUZLU, Yildirim; BASDOGAN, Cagatay. On the measurement of dynamic stability of human locomotion. **Journal of biomechanical engineering**, American Society of Mechanical Engineers, v. 116, n. 1, p. 30–36, 1994.

IBARRA, Juan C. Pérez et al. Adaptive impedance control for robot-aided rehabilitation of ankle movements. In: IEEE. 5TH IEEE RAS/EMBS International Conference on Biomedical Robotics and Biomechatronics. 2014. P. 664–669.

IQBAL, Kamran; PAI, Yi-Chung. Predicted region of stability for balance recovery:: motion at the knee joint can improve termination of forward movement. **Journal of biomechanics**, Elsevier, v. 33, n. 12, p. 1619–1627, 2000.

ISHII, Mineo; YAMAMOTO, Keijiro; HYODO, Kazuhito. Stand-alone wearable power assist suit -Development and availability-. **Journal of robotics and mechatronics**, Fuji Technology Press Ltd., v. 17, n. 5, p. 575–583, 2005.

ISHIKAWA, Masaki et al. Muscle-tendon interaction and elastic energy usage in human walking. **Journal of applied physiology**, American Physiological Society, v. 99, n. 2, p. 603–608, 2005.

IZMAILOV, Pavel et al. Averaging weights leads to wider optima and better generalization. **arXiv preprint arXiv:1803.05407**, 2018.

JARDIM, Bruno; SIQUEIRA, Adriano Almeida Gonçalves. Development of series elastic actuators for impedance control of an active ankle foot orthosis. In: 20TH International Congress of Mechanical Engineering. 2009. P. 15–20.

JARRASSÉ, Nathanaël et al. How can human motion prediction increase transparency? In: IEEE. 2008 IEEE International Conference on Robotics and Automation. 2008. P. 2134–2139.

JULIER, Simon J.; UHLMANN, Jeffrey K. New extension of the Kalman filter to nonlinear systems. In: INTERNATIONAL SOCIETY FOR OPTICS and PHOTONICS. SIGNAL processing, sensor fusion, and target recognition VI. 1997. v. 3068, p. 182–193.

KAJITA, Shuuji; KANEHIRO, Fumio, et al. The 3D linear inverted pendulum mode: A simple modeling for a biped walking pattern generation. In: IEEE. PROCEEDINGS 2001 IEEE/RSJ International Conference on Intelligent Robots and Systems. Expanding the Societal Role of Robotics in the the Next Millennium (Cat. No. 01CH37180). 2001. v. 1, p. 239–246.

KAJITA, Shuuji; TANI, Kazuo. Study of dynamic biped locomotion on rugged terrain-derivation and application of the linear inverted pendulum mode. In: IEEE COMPUTER SOCIETY. PROCEEDINGS. 1991 IEEE International Conference on Robotics and Automation. 1991. P. 1405–1406.

KALMAN, R. E. A New Approach to Linear Filtering and Prediction Problems. **Journal of Basic Engineering**, v. 82, n. 1, p. 35–45, Mar. 1960. ISSN 0021-9223. DOI: 10.1115/1.3662552. eprint: https://asmedigitalcollection.asme.org/fluidsengineering/article-pdf/82/1/35/5518977/35_1.pdf.

KAO, Pei-Chun; LEWIS, Cara L.; FERRIS, Daniel P. Invariant ankle moment patterns when walking with and without a robotic ankle exoskeleton. **Journal of biomechanics**, Elsevier, v. 43, n. 2, p. 203–209, 2010.

KARPATHY, Andrej. The Unreasonable Effectiveness of Recurrent Neural Networks. [Online; accessed 26-Mar-2021], May 2015. Available from: https://karpathy.github.io/2015/05/21/rnn-effectiveness/.

KARSSEN, J.G. Daniël; WISSE, Martijn. Fall detection in walking robots by multi-way principal component analysis. **Robotica**, Cambridge University Press, v. 27, n. 2, p. 249–257, 2009.

KAWAMOTO, Hiroaki; SANKAI, Yoshiyuki. Power assist method based on phase sequence and muscle force condition for HAL. **Advanced Robotics**, Taylor & Francis, v. 19, n. 7, p. 717–734, 2005.

KAZEROONI, Hami et al. On the control of the berkeley lower extremity exoskeleton (BLEEX). In: IEEE. PROCEEDINGS of the 2005 IEEE international conference on robotics and automation. 2005. P. 4353–4360.

KIGUCHI, K. et al. An exoskeletal robot for human shoulder joint motion assist. **IEEE/ASME Transactions on Mechatronics**, v. 8, n. 1, p. 125–135, Mar. 2003. ISSN 1941-014X. DOI: 10.1109/TMECH.2003.809168.

KIM, Daehyon. Normalization methods for input and output vectors in backpropagation neural networks. **International journal of computer mathematics**, Taylor & Francis, v. 71, n. 2, p. 161–171, 1999.

KIM, Jeong Yong; DURFEE, William. The Application of Series Elastic Actuators in the Hydraulic Ankle-Foot Orthosis. In: AMERICAN SOCIETY OF MECHANICAL ENGINEERS. 2018 Design of Medical Devices Conference. 2018. v001t10a003–v001t10a003.

KIM, K.; KANG, M.; CHOI, Y.; HAN, J., et al. Conceptualization of an exoskeleton Continuous Passive Motion (CPM) device using a link structure. In: 2011 IEEE International Conference on Rehabilitation Robotics. June 2011. P. 1–6. DOI: 10.1109/ICORR.2011.5975494.

KIM, Kyu Jung; KANG, Min Sung; CHOI, Younsung; JANG, Hye Youn, et al. Development of the exoskeleton knee rehabilitation robot using the linear actuator. **International Journal of Precision Engineering and Manufacturing**, Springer, v. 13, n. 10, p. 1889–1895, 2012.

KINGMA, Diederik P.; BA, Jimmy. **Adam: A Method for Stochastic Optimization**. 2014. arXiv: 1412.6980 [cs.LG].

KLAMBAUER, Günter et al. Self-normalizing neural networks. **arXiv preprint arXiv:1706.02515**, 2017.

KOOLEN, Twan et al. Capturability-based analysis and control of legged locomotion, Part 1: Theory and application to three simple gait models. **The international journal of robotics research**, SAGE Publications Sage UK: London, England, v. 31, n. 9, p. 1094–1113, 2012.

KOOPMAN, Bart. **The three-dimensional analysis and prediction of human walking**. 1989. PhD thesis – University of Twente, Enschede, The Netherlands.

KRAEMER, William J. et al. Influence of a compression garment on repetitive power output production before and after different types of muscle fatigue. **Sports Medicine, Training and Rehabilitation**, Taylor & Francis, v. 8, n. 2, p. 163–184, 1998. DOI: 10.1080/15438629809512525. eprint: https://doi.org/10.1080/15438629809512525.

KRIZHEVSKY, Alex; SUTSKEVER, Ilya; HINTON, Geoffrey E. Imagenet classification with deep convolutional neural networks. In: ADVANCES in neural information processing systems. 2012. P. 1097–1105.

KUO, Arthur D.; ZAJAC, Felix E. Human standing posture: multi-joint movement strategies based on biomechanical constraints. In: PROGRESS in brain research. Elsevier, 1993. v. 97. P. 349–358.

KUROSAWA, H. et al. Geometry and motion of the knee for implant and orthotic design. **Journal of biomechanics**, Elsevier, v. 18, n. 7, p. 487–499, 1985.

LANDIS, Eugene M. Micro-injection studies of capillary blood pressure in human skin. **Heart**, v. 15, p. 209–228, 1930.

LE, Quoc V. et al. Learning hierarchical invariant spatio-temporal features for action recognition with independent subspace analysis. In: IEEE. CVPR 2011. 2011. P. 3361–3368.

LEAL-JUNIOR, Arnaldo; AVELLAR, Letícia; JAIMES, Jonathan, et al. Polymer Optical Fiber-Based Integrated Instrumentation in a Robot-Assisted Rehabilitation Smart Environment: A Proof of Concept. **Sensors**, Multidisciplinary Digital Publishing Institute, v. 20, n. 11, p. 3199, 2020.

LEAL-JUNIOR, Arnaldo G.; AVELLAR, Letícia M.; DÍAZ, Camilo A. R., et al. Polymer Optical Fiber Sensor System for Multi Plane Bending Angle Assessment. **IEEE Sensors Journal**, IEEE, v. 20, n. 5, p. 2518–2525, 2019.

LEAL-JUNIOR, Arnaldo G.; DIAZ, Camilo R., et al. Multiplexing technique for quasi-distributed sensors arrays in polymer optical fiber intensity variation-based sensors. **Optics & Laser Technology**, Elsevier, v. 111, p. 81–88, 2019.

LEAL-JUNIOR, Arnaldo G.; DÍAZ, Camilo R., et al. 3D-printed POF insole: Development and applications of a low-cost, highly customizable device for plantar pressure and ground reaction forces monitoring. **Optics & Laser Technology**, Elsevier, v. 116, p. 256–264, 2019.

LEAL-JUNIOR, Arnaldo G.; FRIZERA, Anselmo; MARQUES, Carlos, et al. Polymer optical fiber strain gauge for human-robot interaction forces assessment on an active knee orthosis. **Optical Fiber Technology**, Elsevier, v. 41, p. 205–211, 2018.

LEAL-JUNIOR, Arnaldo Gomes; FRIZERA, Anselmo; PONTES, Maria José, et al. Hysteresis compensation technique applied to polymer optical fiber curvature sensor for lower limb exoskeletons. **Measurement Science and Technology**, IOP Publishing, v. 28, n. 12, p. 125103, 2017.

LECUN, Yann et al. Gradient-based learning applied to document recognition. **Proceedings of the IEEE**, Ieee, v. 86, n. 11, p. 2278–2324, 1998.

LEE, David N. A theory of visual control of braking based on information about time-to-collision. **Perception**, SAGE Publications Sage UK: London, England, v. 5, n. 4, p. 437–459, 1976.

LEE, David N.; YOUNG, David S. Visual timing of interceptive action. In: BRAIN mechanisms and spatial vision. Springer, 1985. P. 1–30.

LEE, David N.; YOUNG, David S.; REWT, Dennis. How do somersaulters land on their feet? **Journal of Experimental Psychology: Human Perception and Performance**, American Psychological Association, v. 18, n. 4, p. 1195, 1992.

LEE, Dawit; KANG, Inseung, et al. Real-Time User-Independent Slope Prediction Using Deep Learning for Modulation of Robotic Knee Exoskeleton Assistance. **IEEE Robotics and Automation Letters**, IEEE, v. 6, n. 2, p. 3995–4000, 2021.

LEE, S.; SANKAI, Y. Power assist control for leg with hal-3 based on virtual torque and impedance adjustment. In: IEEE. IEEE International Conference on Systems, Man and Cybernetics. 2002. v. 4, 6–pp.

LEW, William D. et al. A comparison of pistoning forces in orthotic knee joints. **Orthotics Prosthet**, v. 36, n. 2, p. 85–95, 1982.

LI, Dinghua; ZHOU, Jun; LIU, Yingying. Recurrent-neural-network-based unscented Kalman filter for estimating and compensating the random drift of MEMS gyroscopes in real time. **Mechanical Systems and Signal Processing**, Elsevier, v. 147, p. 107057, 2021.

LIU, Du-Xin et al. Deep rehabilitation gait learning for modeling knee joints of lower-limb exoskeleton. In: IEEE. 2016 IEEE International Conference on Robotics and Biomimetics (ROBIO). 2016. P. 1058–1063.

LOPER, Matthew et al. SMPL: A Skinned Multi-Person Linear Model. **ACM Trans. Graphics (Proc. SIGGRAPH Asia)**, ACM, v. 34, n. 6, p. 1–16, Oct. 2015.

LUU, Trieu Phat et al. An individual-specific gait pattern prediction model based on generalized regression neural networks. **Gait & posture**, Elsevier, v. 39, n. 1, p. 443–448, 2014.

LYU, Mingxing et al. Knee exoskeleton enhanced with artificial intelligence to provide assistance-as-needed. **Review of Scientific Instruments**, AIP Publishing LLC, v. 90, n. 9, p. 094101, 2019.

MAAS, Andrew L.; HANNUN, Awni Y.; NG, Andrew Y. Rectifier nonlinearities improve neural network acoustic models. In: CITESEER, 1. PROC. icml. 2013. v. 30, p. 3.

MAHMOOD, Naureen et al. AMASS: Archive of Motion Capture as Surface Shapes. In: INTERNATIONAL Conference on Computer Vision. Oct. 2019. P. 5442–5451.

MALCOLM, Philippe; DERAVE, Wim, et al. A simple exoskeleton that assists plantarflexion can reduce the metabolic cost of human walking. **PloS one**, Public Library of Science, v. 8, n. 2, 2013.

MALCOLM, Philippe; LEE, Sangjun, et al. Varying negative work assistance at the ankle with a soft exosuit during loaded walking. **Journal of neuroengineering and rehabilitation**, BioMed Central, v. 14, n. 1, p. 62, 2017.

MANDERY, Christian et al. The KIT whole-body human motion database. In: IEEE. 2015 International Conference on Advanced Robotics (ICAR). 2015. P. 329–336.

_____. Unifying Representations and Large-Scale Whole-Body Motion Databases for Studying Human Motion. **IEEE Transactions on Robotics**, v. 32, n. 4, p. 796–809, 2016.

MARKOLF, Keith L.; GRAFF-RADFORD, Adrian; AMSTUTZ, H. C. In vivo knee stability. A quantitative assessment using an instrumented clinical testing apparatus. **The Journal of bone and joint surgery. American volume**, v. 60, n. 5, p. 664–674, 1978.

MARKOLF, Keith L.; MENSCH, Joseph S.; AMSTUTZ, Harlan C. Stiffness and laxity of the knee–the contributions of the supporting structures. A quantitative in vitro study. **JBJS**, Citeseer, v. 58, n. 5, p. 583–594, 1976.

MARTINEZ, Julieta; BLACK, Michael J.; ROMERO, Javier. On human motion prediction using recurrent neural networks. In: PROCEEDINGS of the IEEE Conference on Computer Vision and Pattern Recognition. 2017. P. 2891–2900.

MARTINEZ-HERNANDEZ, Uriel et al. Prediction of gait events in walking activities with a Bayesian perception system. In: IEEE. 2017 International Conference on Rehabilitation Robotics (ICORR). 2017. P. 13–18.

MASSEN, C. H.; KODDE, L. Model for the description of left-right stabilograms. **Agressologie**, MASSON EDITEUR 120 BLVD SAINT-GERMAIN, 75280 PARIS 06, FRANCE, v. 20, p. 107–108, 1979.

MATRONE, Giulia C.; CIPRIANI, Christian; CARROZZA, Maria Chiara, et al. Real-time myoelectric control of a multi-fingered hand prosthesis using principal components analysis. **Journal of neuroengineering and rehabilitation**, BioMed Central, v. 9, n. 1, p. 1–13, 2012.

MATRONE, Giulia C.; CIPRIANI, Christian; SECCO, Emanuele L., et al. Principal components analysis based control of a multi-dof underactuated prosthetic hand. **Journal of neuroengineering and rehabilitation**, BioMed Central, v. 7, n. 1, p. 1–13, 2010.

MAUREL, Walter. **3D modeling of the human upper limb including the biomechanics of joints, muscles and soft tissues**. 1999. PhD thesis – EPFL.

MCCULLOCH, Warren S.; PITTS, Walter. A logical calculus of the ideas immanent in nervous activity. **The bulletin of mathematical biophysics**, Springer, v. 5, n. 4, p. 115–133, 1943.

MCDAVID. **Knee Brace with Polycentric Hinges**. 2020. https://www.mcdavidusa.com/products/knee-brace-w-polycentric-hinges?variant=19352873107552. [Online; accessed 21-Feb-2020].

MCGEER, Tad et al. Passive dynamic walking. **International Journal of Robotics Research**, v. 9, n. 2, p. 62–82, 1990.

MCINTOSH, Scott E et al. Medical incidents and evacuations on wilderness expeditions. **Wilderness & environmental medicine**, Elsevier, v. 18, n. 4, p. 298–304, 2007.

MENGÜÇ, Yiğit et al. Wearable soft sensing suit for human gait measurement. **The International Journal of Robotics Research**, SAGE Publications Sage UK: London, England, v. 33, n. 14, p. 1748–1764, 2014.

MISRA, Diganta. Mish: A self regularized non-monotonic neural activation function. **arXiv preprint arXiv:1908.08681**, CoRR, v. 4, 2019.

MISTRY, M.; BUCHLI, J.; SCHAAL, S. Inverse dynamics control of floating base systems using orthogonal decomposition. In: 2010 IEEE International Conference on Robotics and Automation. May 2010. P. 3406–3412. DOI: 10.1109/ROBOT.2010.5509646.

MITCHELL, M. **An Introduction to Genetic Algorithms**. Bradford Books, 1998. (A Bradford book). ISBN 9780262631853. Available from: https://books.google.com.br/books?id=0eznlz0TF-IC.

MNIH, Volodymyr et al. Human-level control through deep reinforcement learning. **nature**, Nature Publishing Group, v. 518, n. 7540, p. 529–533, 2015.

MOONEY, Luke M.; ROUSE, Elliott J.; HERR, Hugh M. Autonomous exoskeleton reduces metabolic cost of human walking during load carriage. **Journal of neuroengineering and rehabilitation**, BioMed Central, v. 11, n. 1, p. 80, 2014.

MOORE, K. L.; AGUR, A. M. R.; DALLEY, A. F. **Clinically Oriented Anatomy**. Wolters Kluwer, 2018. (Clinically Oriented Anatomy). ISBN 9781496347213. Available from: https://books.google.com.br/books?id=MA%5C_%7BR%7D%7Bj%7D%7Bw%7DEACAAJ.

MORENO, Juan C. et al. Analysis of the human interaction with a wearable lower-limb exoskeleton. **Applied Bionics and Biomechanics**, IOS Press, v. 6, n. 2, p. 245–256, 2009.

MÜLLER, M. et al. **Documentation Mocap Database HDM05**. June 2007.

NAIR, Vinod; HINTON, Geoffrey E. Rectified linear units improve restricted boltzmann machines. In: ICML. 2010.

NICOLELIS, M. A.; BACCALA, L. A., et al. Sensorimotor encoding by synchronous neural ensemble activity at multiple levels of the somatosensory system. **Science**, American Association for the Advancement of Science, v. 268, n. 5215, p. 1353–1358, 1995. ISSN 0036-8075. DOI: 10.1126/science.7761855. eprint: https://science.sciencemag.org/content/268/5215/1353.full.pdf. Available from: https://science.sciencemag.org/content/268/5215/1353.

NICOLELIS, Miguel A. L.; CHAPIN, John K. Controlling robots with the mind. **Scientific American**, Scientific American, a division of Nature America, Inc., v. 287, n. 4, p. 46–53, 2002.

NOGUEIRA, Samuel et al. Markov jump linear systems-based position estimation for lower limb exoskeletons. **Sensors**, Multidisciplinary Digital Publishing Institute, v. 14, n. 1, p. 1835–1849, 2014.

NORRIS, James A. et al. Effect of augmented plantarflexion power on preferred walking speed and economy in young and older adults. **Gait & posture**, Elsevier, v. 25, n. 4, p. 620–627, 2007.

OKLE, Jan. **Certification of Controllers for Wearable Robots**. June 2016. MA thesis – Swiss Federal Institute of Technology Zurich.

OLINSKI, M. et al. Design and characterization of a novel knee articulation mechanism. **International Journal of Applied Mechanics and Engineering**, De Gruyter Open, v. 21, n. 3, p. 611–622, 2016.

OORD, Aaron van den; DIELEMAN, Sander; SCHRAUWEN, Benjamin. Deep content-based music recommendation. In: BURGES, C. J. C. et al. (Eds.). **Advances in Neural Information Processing Systems 26**. Curran Associates, Inc., 2013. P. 2643–2651. Available from: http://papers.nips.cc/paper/5004-deep-content-based-music-recommendation.pdf.

OSMAN, Ahmed A. A.; BOLKART, Timo; BLACK, Michael J. STAR: Sparse Trained Articulated Human Body Regressor. **arXiv preprint arXiv:2008.08535**, 2020.

OSU. **Advanced Computing Center for the Arts and Design**. 2021. Online. [Online; accessed 26-Mar-2021]. Available from: https://accad.osu.edu/research/motion-lab/mocap-system-and-data.

PAI, Yi-Chung; PATTON, James. Center of mass velocity-position predictions for balance control. **Journal of biomechanics**, Elsevier, v. 30, n. 4, p. 347–354, 1997.

PANDYA, Ashish; KHIMA, Dangar; TULSHI, Singel. Study of a Trochanteric Length of Femur. **Journal of Medical Science and Clinical Research**, v. 4, n. 4, p. 5, Apr. 2016. ISSN 2347-176x.

PANIZZOLO, Fausto A. et al. A biologically-inspired multi-joint soft exosuit that can reduce the energy cost of loaded walking. **Journal of neuroengineering and rehabilitation**, BioMed Central, v. 13, n. 1, p. 1–14, 2016.

PAVLAKOS, Georgios et al. Expressive Body Capture: 3D Hands, Face, and Body from a Single Image. In: PROCEEDINGS IEEE Conf. on Computer Vision and Pattern Recognition (CVPR). 2019. P. 10975–10985.

PAVLLO, Dario; GRANGIER, David; AULI, Michael. Quaternet: A quaternion-based recurrent model for human motion. **arXiv preprint arXiv:1805.06485**, 2018.

PONS, José L. **Wearable robots: biomechatronic exoskeletons**. John Wiley & Sons, 2008.

PRATT, Jerry; CARFF, John, et al. Capture point: A step toward humanoid push recovery. In: IEEE. 2006 6th IEEE-RAS international conference on humanoid robots. 2006. P. 200–207.

PRATT, Jerry; KOOLEN, Twan, et al. Capturability-based analysis and control of legged locomotion, Part 2: Application to M2V2, a lower-body humanoid. **The international journal of robotics research**, SAGE Publications Sage UK: London, England, v. 31, n. 10, p. 1117–1133, 2012.

PRATT, Jerry; KRUPP, Benjamin, et al. The RoboKnee: an exoskeleton for enhancing strength and endurance during walking. In: IEEE. IEEE International Conference on Robotics and Automation, 2004. Proceedings. ICRA'04. 2004. 2004. v. 3, p. 2430–2435.

PRATT, Jerry E.; TEDRAKE, Russ. Velocity-based stability margins for fast bipedal walking. In: FAST motions in biomechanics and robotics. Springer, 2006. P. 299–324.

RAKSHIT, Ritwik. **Kinematic design of an anatomically-accurate exoskeleton knee joint**. 2017. MA thesis – Texas Tech University.

RALSTON, Henry J. Energy-speed relation and optimal speed during level walking. **Internationale Zeitschrift für Angewandte Physiologie Einschliesslich Arbeitsphysiologie**, Springer, v. 17, n. 4, p. 277–283, 1958.

RAMACHANDRAN, Prajit; ZOPH, Barret; LE, Quoc V. Searching for activation functions. **arXiv preprint arXiv:1710.05941**, 2017.

RIGHETTI, Ludovic et al. Inverse dynamics control of floating-base robots with external constraints: A unified view. In: IEEE. 2011 IEEE international conference on robotics and automation. 2011. P. 1085–1090.

ROCON, E.; RUIZ, A. F., et al. Rehabilitation Robotics: a Wearable Exo-Skeleton for Tremor Assessment and Suppression. In: PROCEEDINGS of the 2005 IEEE International Conference on Robotics and Automation. Apr. 2005. P. 2271–2276. DOI: 10.1109/ROBOT.2005.1570451.

ROCON, Eduardo; MANTO, Mario, et al. Mechanical suppression of essential tremor. **The Cerebellum**, Springer, v. 6, n. 1, p. 73–78, 2007.

ROMERO, Javier; TZIONAS, Dimitrios; BLACK, Michael J. Embodied Hands: Modeling and Capturing Hands and Bodies Together. **ACM Transactions on Graphics, (Proc. SIGGRAPH Asia)**, v. 36, n. 6, Nov. 2017.

RONSSE, Renaud et al. Oscillator-based assistance of cyclical movements: model-based and model-free approaches. **Medical & biological engineering & computing**, Springer, v. 49, n. 10, p. 1173–1185, 2011.

ROSE, Lowell. **A Lower-Body Exoskeleton Simulation and Control Framework based on Deep Reinforcement Learning**. 2020. MA thesis – University of Toronto.

ROSE, Lowell; BAZZOCCHI, Michael CF; NEJAT, Goldie. End-to-End Deep Reinforcement Learning for Exoskeleton Control. In: IEEE. 2020 IEEE International Conference on Systems, Man, and Cybernetics (SMC). 2020. P. 4294–4301.

ROSEN, Jacob; PERRY, Joel C. Upper limb powered exoskeleton. **International Journal of Humanoid Robotics**, World Scientific, v. 4, n. 03, p. 529–548, 2007.

ROSENBLATT, Frank. The perceptron: a probabilistic model for information storage and organization in the brain. **Psychological review**, American Psychological Association, v. 65, n. 6, p. 386, 1958.

ROY, Anindo et al. Measurement of human ankle stiffness using the anklebot. In: IEEE. 2007 IEEE 10th International Conference on Rehabilitation Robotics. 2007. P. 356–363.

SANKAI, Yoshiyuki. Leading edge of cybernics: Robot suit HAL. In: IEEE. 2006 SICE-ICASE International Joint Conference. 2006. p–1.

SANTOS, Wilian M. dos et al. Design and evaluation of a modular lower limb exoskeleton for rehabilitation. In: IEEE. 2017 International Conference on Rehabilitation Robotics (ICORR). 2017. P. 447–451.

SAUNDERS, J. B.; INMAN, Verne T.; EBERHART, Howard D. The major determinants in normal and pathological gait. **JBJS**, LWW, v. 35, n. 3, p. 543–558, 1953.

SAWICKI, Gregory S.; DOMINGO, Antoinette; FERRIS, Daniel P. The effects of powered ankle-foot orthoses on joint kinematics and muscle activation during walking in individuals with incomplete spinal cord injury. **Journal of neuroengineering and rehabilitation**, Springer, v. 3, n. 1, p. 3, 2006.

SAWICKI, Gregory S.; FERRIS, Daniel P. Mechanics and energetics of incline walking with robotic ankle exoskeletons. **Journal of Experimental Biology**, The Company of Biologists Ltd, v. 212, n. 1, p. 32–41, 2009.

_____. Mechanics and energetics of level walking with powered ankle exoskeletons. **Journal of Experimental Biology**, The Company of Biologists Ltd, v. 211, n. 9, p. 1402–1413, 2008.

_____. Powered ankle exoskeletons reveal the metabolic cost of plantar flexor mechanical work during walking with longer steps at constant step frequency. **Journal of Experimental Biology**, The Company of Biologists Ltd, v. 212, n. 1, p. 21–31, 2009.

SCHIELE, A.; HELM, F. C. T. van der. Kinematic Design to Improve Ergonomics in Human Machine Interaction. **IEEE Transactions on Neural Systems and Rehabilitation Engineering**, v. 14, n. 4, p. 456–469, Dec. 2006. ISSN 1558-0210. DOI: 10.1109/TNSRE.2006.881565.

SCHIELE, André; VISENTIN, Gianfranco. The ESA human arm exoskeleton for space robotics telepresence. In: 7TH International Symposium on Artificial Intelligence, Robotics and Automation in Space. 2003. P. 19–23.

SEEL, Thomas; RAISCH, Jörg; SCHAUER, Thomas. IMU-based joint angle measurement for gait analysis. **Sensors**, Multidisciplinary Digital Publishing Institute, v. 14, n. 4, p. 6891–6909, 2014.

SHEN, Kevin. Effect of batch size o training dynamics. [Online; accessed 25-Mar-2021], June 2018. Available from: https://medium.com/mini-distill/effect-of-batch-size-on-training-dynamics-21c14f7a716e.

SHUMWAY-COOK, A.; WOOLLACOTT, M. H. **Motor Control: Theory and Practical Applications**. Williams & Wilkins, 1995. ISBN 9780683077575. Available from: https://books.google.com.br/books?id=2QFtAAAAMAAJ.

SIEGELMANN, Hava T. Computation beyond the Turing limit. **Science**, American Association for the Advancement of Science, v. 268, n. 5210, p. 545–548, 1995.

SILBERNAGL, S.; DESPOPOULOS, A. **Color Atlas of Physiology**. Thieme, 2011. (Flexibook Color atlas of physiology). ISBN 9783131495211. Available from: https://books.google.com.br/books?id=WyuCGhv4kvwC.

SILVER, David; HUANG, Aja, et al. Mastering the game of Go with deep neural networks and tree search. **nature**, Nature Publishing Group, v. 529, n. 7587, p. 484–489, 2016.

SILVER, David; HUBERT, Thomas, et al. AlphaZero: Shedding new light on the grand games of chess, shogi and Go. **DeepMind blog**, 2018.

SIMPSON, Katrina M.; MUNRO, Bridget J.; STEELE, Julie R. Backpack load affects lower limb muscle activity patterns of female hikers during prolonged load carriage. **Journal of Electromyography and Kinesiology**, Elsevier, v. 21, n. 5, p. 782–788, 2011.

SLOBOUNOV, Semyon M.; SLOBOUNOVA, Elena S.; NEWELL, Karl M. Virtual time-to-collision and human postural control. **Journal of motor Behavior**, Taylor & Francis, v. 29, n. 3, p. 263–281, 1997.

SMITH, Lindsay I. **A tutorial on Principal Components Analysis**. 26 Feb. 2002. Available from: https://ourarchive.otago.ac.nz/bitstream/handle/10523/7534/OUCS-2002-12.pdf.

SMITH, Samuel L. et al. **Don't Decay the Learning Rate, Increase the Batch Size**. 2018. arXiv: 1711.00489 [cs.LG].

SOLA, Jorge; SEVILLA, Joaquin. Importance of input data normalization for the application of neural networks to complex industrial problems. **IEEE Transactions on nuclear science**, IEEE, v. 44, n. 3, p. 1464–1468, 1997.

SRIVASTAVA, Nitish et al. Dropout: a simple way to prevent neural networks from overfitting. **The journal of machine learning research**, JMLR. org, v. 15, n. 1, p. 1929–1958, 2014.

STEWART, Doug. A platform with six degrees of freedom. **Proceedings of the institution of mechanical engineers**, SAGE Publications Sage UK: London, England, v. 180, n. 1, p. 371–386, 1965.

SUH, C. H.; RADCLIFFE, C. W. **Kinematics and mechanisms design**. R.E. Krieger Pub. Co., 1978. ISBN 9780898746877. Available from: https://books.google.com.br/books?id=Xe5SAAAAMAAJ.

SUN, Jian et al. Design of the force-sensors system of WPAL. In: 2007 IEEE International Conference on Robotics and Biomimetics (ROBIO). Dec. 2007. P. 1321–1326. DOI: 10.1109/ROBIO.2007.4522355.

SUTSKEVER, Ilya; MARTENS, James, et al. On the importance of initialization and momentum in deep learning. In: PMLR. INTERNATIONAL conference on machine learning. 2013. P. 1139–1147.

SUTSKEVER, Ilya; VINYALS, Oriol; LE, Quoc V. Sequence to sequence learning with neural networks. In: ADVANCES in neural information processing systems. 2014. P. 3104–3112.

SUTTON, R. S.; BARTO, A. G. **Reinforcement Learning: An Introduction**. MIT Press, 2018. (Adaptive Computation and Machine Learning series). ISBN 9780262039246. Available from: https://books.google.com.br/books?id=sWV0DwAAQBAJ.

SZEGEDY, Christian; IOFFE, Sergey, et al. Inception-v4, inception-resnet and the impact of residual connections on learning. In: 1. PROCEEDINGS of the AAAI Conference on Artificial Intelligence. 2017. v. 31.

SZEGEDY, Christian; LIU, Wei, et al. Going deeper with convolutions. In: PROCEEDINGS of the IEEE conference on computer vision and pattern recognition. 2015. P. 1–9.

SZEGEDY, Christian; VANHOUCKE, Vincent, et al. Rethinking the inception architecture for computer vision. In: PROCEEDINGS of the IEEE conference on computer vision and pattern recognition. 2016. P. 2818–2826.

TERLEMEZ, Ömer et al. Master Motor Map (MMM)—Framework and toolkit for capturing, representing, and reproducing human motion on humanoid robots. In: IEEE. 2014 IEEE-RAS International Conference on Humanoid Robots. 2014. P. 894–901.

THANGAL, Sayed Naseel Mohamed; TALATY, Mukul; BALASUBRAMANIAN, Sriram. Assessment of gait sensitivity norm as a predictor of risk of falling during walking in a neuromusculoskeletal model. **Medical Engineering & Physics**, Elsevier, v. 35, n. 10, p. 1483–1489, 2013.

TOWNSEND, Miles A. Biped gait stabilization via foot placement. **Journal of biomechanics**, Elsevier, v. 18, n. 1, p. 21–38, 1985.

TRENT, Peter S.; WALKER, Peter S.; WOLF, Barry. Ligament length patterns, strength, and rotational axes of the knee joint. **Clinical orthopaedics and related research**, n. 117, p. 263–270, 1976.

TROJE, Nikolaus F. Decomposing biological motion: A framework for analysis and synthesis of human gait patterns. **Journal of vision**, The Association for Research in Vision and Ophthalmology, v. 2, n. 5, p. 2–2, 2002.

TUCKER, Michael R. et al. Design of a wearable perturbator for human knee impedance estimation during gait. In: IEEE. 2013 IEEE 13th International Conference on Rehabilitation Robotics (ICORR). 2013. P. 1–6.

TURING, Alan Mathison. **Intelligent machinery**. NPL. Mathematics Division, 1948.

UPTON, G.; COOK, I. **A Dictionary of Statistics**. 3. ed.: OUP Oxford, 2014. (Oxford Paperback Reference). ISBN 9780199679188. Available from: https://books.google.com.br/books?id=4WygAwAAQBAJ.

VALLERY, Heike; BÖGEL, Alexander; RIENER, Robert, et al. Cooperative control design for robot-assisted balance during gait. **at-Automatisierungstechnik Methoden und Anwendungen der Steuerungs-, Regelungs-und Informationstechnik**, Oldenbourg Wissenschaftsverlag GmbH, v. 60, n. 11, p. 715–720, 2012.

VALLERY, Heike; DUSCHAU-WICKE, Alexander; RIENER, Robert. Optimized passive dynamics improve transparency of haptic devices. In: IEEE. 2009 IEEE international conference on robotics and automation. 2009. P. 301–306.

VENEMAN, Jan F. et al. A series elastic-and bowden-cable-based actuation system for use as torque actuator in exoskeleton-type robots. **The international journal of robotics research**, SAGE Publications, v. 25, n. 3, p. 261–281, 2006.

VINYALS, Oriol et al. Grandmaster level in StarCraft II using multi-agent reinforcement learning. **Nature**, Nature Publishing Group, v. 575, n. 7782, p. 350–354, 2019.

VON MARCARD, Timo et al. Sparse inertial poser: Automatic 3d human pose estimation from sparse imus. In: WILEY ONLINE LIBRARY, 2. COMPUTER Graphics Forum. 2017. v. 36, p. 349–360.

WALKER, P. S.; KUROSAWA, H., et al. External knee joint design based on normal motion. **J Rehabil Res Dev**, v. 22, n. 1, p. 9–22, 1985.

WALKER, P. S.; ROVICK, J. S.; ROBERTSON, D. D. The effects of knee brace hinge design and placement on joint mechanics. **Journal of biomechanics**, Elsevier, v. 21, n. 11, p. 965–974, 1988.

WAN, Eric A.; VAN DER MERWE, Rudolph. The unscented Kalman filter for nonlinear estimation. In: IEEE. PROCEEDINGS of the IEEE 2000 Adaptive Systems for Signal Processing, Communications, and Control Symposium (Cat. No. 00EX373). 2000. P. 153–158.

WANG, Can; WU, Xinyu, et al. A flexible lower extremity exoskeleton robot with deep locomotion mode identification. **Complexity**, Hindawi, v. 2018, 2018.

WANG, Ching-Jen; WALKER, Peter S. Rotatory laxity of the human knee joint. **JBJS**, LWW, v. 56, n. 1, p. 161–170, 1974.

WESSBERG, Johan et al. Real-time prediction of hand trajectory by ensembles of cortical neurons in primates. **Nature**, Nature Publishing Group, v. 408, n. 6810, p. 361, 2000.

WEST, Bruce J.; GRIFFIN, Lori. Allometric control, inverse power laws and human gait. **Chaos, Solitons & Fractals**, Elsevier, v. 10, n. 9, p. 1519–1527, 1999.

WIEBER, Pierre-Brice. On the stability of walking systems. In: PROCEEDINGS of the international workshop on humanoid and human friendly robotics. 2002.

WIGGIN, M. Bruce; SAWICKI, Gregory S.; COLLINS, Steven H. An exoskeleton using controlled energy storage and release to aid ankle propulsion. In: IEEE. 2011 IEEE International Conference on Rehabilitation Robotics. 2011. P. 1–5.

WILLIAMS, R. L.; REINHOLTZ, C. F. Proof of Grashof's Law Using Polynomial Discriminants. **Journal of Mechanisms, Transmissions, and Automation in Design**, v. 108, n. 4, p. 562–564, Dec. 1986. ISSN 0738-0666. DOI: 10.1115/1.3258770.

WINFREE, K. N.; STEGALL, P.; AGRAWAL, S. K. Design of a minimally constraining, passively supported gait training exoskeleton: ALEX II. In: 2011 IEEE International Conference on Rehabilitation Robotics. June 2011. P. 1–6. DOI: 10.1109/ICORR.2011.5975499.

WINTER, D. A.; YACK, H. J. EMG profiles during normal human walking: stride-to-stride and inter-subject variability. **Electroencephalography and clinical neurophysiology**, Elsevier, v. 67, n. 5, p. 402–411, 1987.

WINTER, David A. **A.B.C. (anatomy, Biomechanics and Control) of Balance During Standing and Walking**. Waterloo Biomechanics, 1995. ISBN 9780969942009. Available from: https://books.google.com.br/books?id=0lSqQgAACAAJ.

_____. **Biomechanics and Motor Control of Human Movement**. Wiley, 2009. ISBN 9780470398180. Available from: https://books.google.com.br/books?id=%5C_%7Bb%7D%7BF%7D%7BH%7DL08IWfwC.

_____. Energy generation and absorption at the ankle and knee during fast, natural, and slow cadences. **Clinical orthopaedics and related research**, n. 175, p. 147–154, 1983.

XSENS. **MVN Analyze**. 26 Apr. 2021. Available from: https://www.xsens.com/products/mvn-analyze.

_____. **MVN Hardware Overview**. 21 Apr. 2020. Available from: https://base.xsens.com/knowledgebase/s/article/MVN-Hardware-Overview.

YU, Yong; LIANG, Wenyuan. Design optimization for parallel mechanism using on human hip joint power assisting based on manipulability inclusive principle. In: IEEE. 2012 IEEE International Conference on Robotics and Automation. 2012. P. 2306–2312.

YUN, Youngmok et al. Statistical method for prediction of gait kinematics with Gaussian process regression. **Journal of Biomechanics**, Elsevier, v. 47, n. 1, p. 186–192, 2014.

ZANOTTO, Damiano et al. Improving transparency of powered exoskeletons using force/torque sensors on the supporting cuffs. In: IEEE. 2013 IEEE 13th International Conference on Rehabilitation Robotics (ICORR). 2013. P. 1–6.

ZEILER, Matthew D.; FERGUS, Rob. Visualizing and understanding convolutional networks. In: SPRINGER. EUROPEAN conference on computer vision. 2014. P. 818–833.

ZHENG, Yi et al. Research on motion pattern recognition of exoskeleton robot based on multimodal machine learning model. **Neural Computing and Applications**, Springer, p. 1–9, 2019.

ZHOU, Shi et al. Electromechanical delay in isometric muscle contractions evoked by voluntary, reflex and electrical stimulation. **European Journal of Applied Physiology and Occupational Physiology**, v. 70, n. 2, p. 138–145, 1 Mar. 1995. ISSN 1439-6327. DOI: 10.1007/BF00361541.

ZIEMANN, O. et al. **POF Handbook: Optical Short Range Transmission Systems**. Springer Berlin Heidelberg, 2008. ISBN 9783540766292. Available from: https://books.google.com.br/books?id=CBG9aGlgZYAC.

APPENDIX

APPENDIX A – GENETIC ALGORITHM DETAILS

The genetic algorithm (GA) (MITCHELL, 1998) is a derivative-free optimization technique inspired on biological evolution (DARWIN, 1864). In the present work, it was used to optimize the geometries of the proposed ankle (Section 3.1) and knee (Section 3.2) exoskeleton joints. Both problems aim at optimizing continuous-valued parameters. This appendix describes, in further detail, all steps involved in this optimization algorithm. It starts with a short textual description in general terms, with additional sections describing the maths behind each GA operator: *selection*, *crossover*, and *mutation*.

In a genetic algorithm, each individual represents the set of parameters to be optimized. With that, the first step involves initializing a population with a given number of individuals, each one receiving random values (inside a predetermined range) for each parameter. Then, a first step of fitness evaluation is performed: here, a target cost function must be evaluated for each individual. This can mean running a simulation and gathering output data, or simply evaluating a mathematical expression, for instance. The cost function must output a single real number, to be minimized. The minimum value for the cost function must be continuously tracked, as well as the corresponding individual.

The randomly initialized population, after fitness evaluation, composes the main population. From there, the offsprings population is generated, which can be of arbitrary size (a common choice is to make it the same size as the main population). Each offspring is created by crossing over two individuals from the main population, picked randomly or based on some criterion. Section A.1 describes a selection technique called *Roulette Wheel Selection*, and Section A.2 explains the crossover of real-valued individuals. Next, to enhance solution space exploration, the offsprings can also suffer mutation (Section A.3). After that, they must also undergo fitness evaluation, checking if any individual has a lower cost than the previous best solution.

Next comes the survival of the fittest: both populations (main and offsprings) are merged and sorted according to the fitness of each individual. The ones with the lowest fitness (highest cost values) are eliminated, so that the size of the new population matches the initial size of the main population. Next, this selected population replaces the previous main one and restarts the loop. The optimization can stop as soon as a certain criterion is met: a maximum number of iterations, the best value of the cost function lower than some predefined value, or the difference of best fitness between two consecutive iterations below a certain threshold. The individual with the lowest cost is then chosen as the optimal solution.

Refer to the following sections for details on the aforementioned operators. Figure

80 summarizes the optimization loop as a flowchart.

Figure 80 – Flowchart representing the genetic algorithm optimization loop.

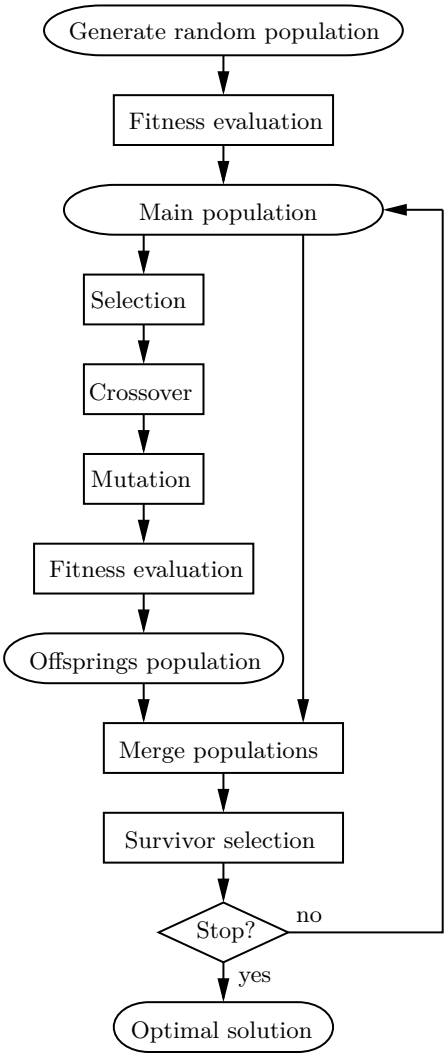

Source: authored

A.1 Roulette Wheel Selection

Roulette wheel is a way of randomly picking an item inside a set (an individual, in this case), but with a different probability of picking each individual item. The name of the method relates to its visual representation, shown in Figure 81. For a genetic algorithm, it is preferred to increase the probability of choosing fitter individuals. This is achieved by using a negative exponential as follows:

$$p_i = e^{-\beta c_i/\bar{c}} \tag{A.1}$$

$$\bar{c} = \frac{1}{n}\sum_{i=1}^{n} c_i \tag{A.2}$$

In which:

- p_i: probability of choosing individual i;
- β: bias factor; $\beta = 0$ makes all selection probabilities equal, while $\beta \to \infty$ means strongly biasing the probability towards the best individual;
- c_i: cost of individual i;
- $\bar{c}$: average cost;
- n: total number of individuals.

Figure 81 – Example of a roulette wheel with four items. If one would rotate this wheel and pick the item selected by the black triangle, the choice is random, however distributed unevenly across all items.

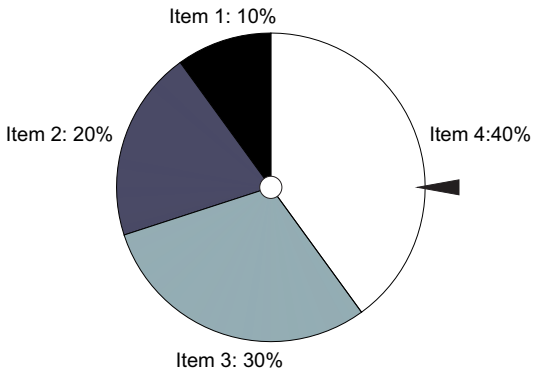

Source: authored

At last, roulette wheel selection is completed by randomly picking a number r inside the range of the cumulative sum array of p_i, and finding the first index where r is less than or equal to the cumulative sum.

A.2 Uniform crossover

Crossing over real-valued individuals mean generating two offspring individuals by taking a randomly weighted sum of each parameter from the parents. Consider two parent individuals, x_1 and x_2, and two offsprings, y_1 and y_2, each one with its parameter set, as follows:

$$x_1 = (x_{11}, x_{12}, \ldots, x_{1m}) \tag{A.3}$$

$$x_2 = (x_{21}, x_{22}, \ldots, x_{2m}) \tag{A.4}$$

$$y_1 = (y_{11}, y_{12}, \ldots, y_{1m}) \tag{A.5}$$

$$y_2 = (y_{21}, y_{22}, \ldots, y_{2m}) \tag{A.6}$$

To compute the weighted sum, a new array, α, with the same length as the individuals, is randomly filled with real values between 0 and 1:

$$\alpha = (\alpha_1, \alpha_2, \ldots, \alpha_m), \alpha_i \in [0, 1] \tag{A.7}$$

The offspring individuals are thus defined as:

$$y_{1i} = \alpha_i x_{1i} + (1 - \alpha_i) x_{2i} \tag{A.8}$$

$$y_{21} = (1 - \alpha_i) x_{1i} + \alpha_i x_{2i} \tag{A.9}$$

A.3 Mutation

Mutating an individual means adding random noise to its parameter values. This noise is usually sampled from a normal distribution, with zero mean and arbitrary standard deviation. Mutations are as expressive as the amplitude of this deviation, called *mutation step size*. It is also interesting to make mutations happen by chance, by generating a random number r and selecting a threshold μ, so that the mutation happens if $r < \mu$. In math terms, this is described as:

$$x_i' = \begin{cases} x_i + \delta, & \text{if } r < \mu \\ x_i, & \text{otherwise} \end{cases} \tag{A.10}$$

$$\delta \sim N(0, \sigma^2) \tag{A.11}$$

In which:

- x_i': mutated value for parameter i of individual x;
- x_i: original value for parameter i of individual x;
- δ: random value sampled from the normal distribution $N(0, \sigma^2)$;
- σ: mutation step size;
- r: random number (usually sampled from a uniform distribution between 0 and 1);
- μ: probability threshold for a mutation to occur (again, between 0 and 1).

APPENDIX B – ACTIVATION FUNCTIONS

An important parameter for any layer of a neural network is the activation function, being responsible for making them nonlinear, thus enabling the well-known broad application scope of such algorithms. The Rectified Linear Unit (ReLU) (NAIR; HINTON, 2010) has been recently used as the standard activation function for nearly all applications, due to its consistent performance associated with a very simple computation. It allows individual neurons to express strong activation due to being unbounded above, which also helps gradient flow in very deep networks, common problems with earlier activations such as *sigmoid* or *tanh* (hyperbolic tangent). A visual comparison is provided in Figure 82. ReLU is also less sensitive to initialization values than the other two.

Figure 82 – Shape of the ReLU (NAIR; HINTON, 2010) activation function compared to the earlier sigmoid and hyperbolic tangent functions.

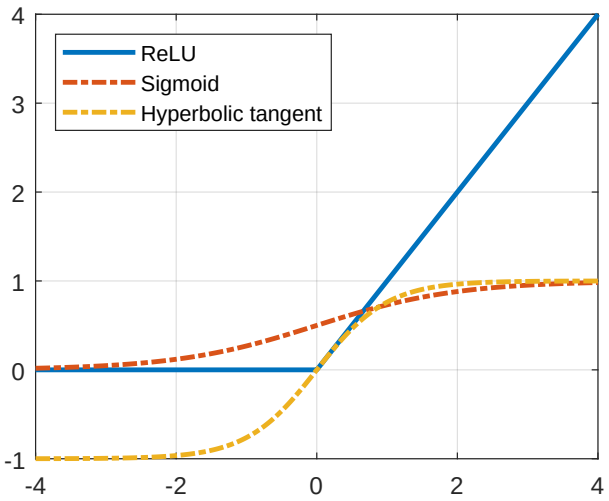

Source: authored

However, ReLU also has its drawbacks, such as creating dead neurons (when inputs get consistently negative, keeping the output stuck at zero) and the strong gradient discontinuity at the origin. Many ReLU variants were proposed, such as Leaky ReLU (MAAS; HANNUN; NG, 2013), Parametric ReLU (HE et al., 2015), Exponential Linear Unit (ELU) (CLEVERT; UNTERTHINER; HOCHREITER, 2015), Scaled Exponential Linear Unit (SELU) (KLAMBAUER et al., 2017), and Gaussian Error Linear Unit (GELU) (HENDRYCKS; GIMPEL, 2016). However, their performance gains are mostly inconsistent across different applications, with some of them adding considerable computational complexity.

More recently, some studies presented alternatives that consistently outperform ReLU while having reasonable computational complexity. The Swish activation function

was introduced by Ramachandran, Zoph, and Le (2017), being smooth and non-monotonic. Replacing ReLU with Swish on Inception-ResNet-V2 (SZEGEDY; IOFFE, et al., 2017) yielded 0.6 % accuracy improvement on ImageNet. This is quite significant, as boosting accuracy by 1.3 % required one year of architectural tuning and enlarging, going from Inception V3 (SZEGEDY; VANHOUCKE, et al., 2016) to Inception-ResNet-V2 (SZEGEDY; IOFFE, et al., 2017). The Swish activation function is defined as follows:

$$f_{Swish}(x) = x \cdot \sigma(\beta x) \tag{B.1}$$

In which β is a constant or learnable parameter, usually kept equal to 1, and $\sigma(x)$ is the sigmoid function, $\sigma(x) = (1 + \exp(-x))^{-1}$. After that, another activation, called Mish (MISRA, 2019), was proposed, with the following definition:

$$f_{Mish}(x) = x \cdot \tanh(\varsigma(x)) \tag{B.2}$$

In which $\varsigma(x)$ is the softplus activation function, $\varsigma(x) = \ln(1 + \exp(x))$. Mish exhibits consistent improvement when compared to both Swish and ReLU. Figure 83 compares the shape of these three functions.

Figure 83 – Shape of the standard ReLU (NAIR; HINTON, 2010) activation function and its most recent alternatives, Swish (RAMACHANDRAN; ZOPH; LE, 2017) and Mish (MISRA, 2019).

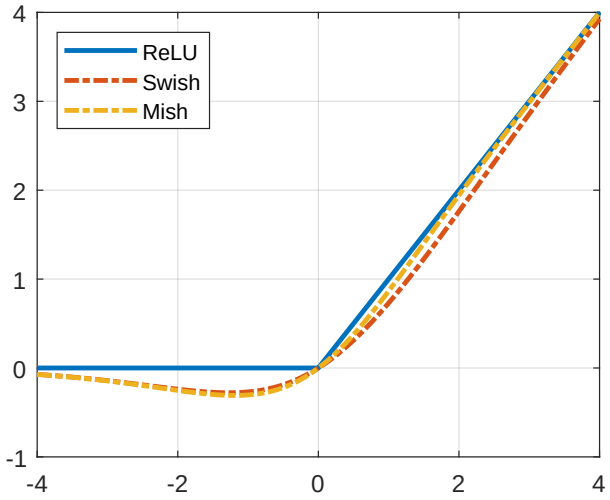

Source: authored

APPENDIX C – AVERAGE AND STANDARD DEVIATION OF TWO DATA SETS

This short appendix details a statistical procedure of updating the mean and standard deviation values when two data sets are joined together to create a third, larger set. Such a method is useful when computing those metrics over a set of data points that exceeds the memory capacity of a computer or embedded device, or data that is continuously generated over time. It is not necessary to know every single value of each data set; instead, just three numbers are required: mean, standard deviation, and number of data points. Table 9 summarizes the notation that will be used to derive the expressions for the updated values of the mean and standard deviation.

Table 9 – Notations for mean, standard deviation and number of data points for the two original data sets (0 and 1) and the new data set (2), obtained from combining the first two.

Variable	**Data set #0**	**Data set #1**	**Combined data set (#2)**
Mean	μ_0	μ_1	μ_2
Standard deviation	σ_0	σ_1	σ_2
Number of data points	n_0	n_1	$n_2 = n_0 + n_1$

C.1 Updated mean

Starting from the definition of mean and using x to represent a single data point, the following expressions define the mean of data set #0 (analogous for #1) and the combined data set:

$$\mu_0 = \frac{1}{n_0} \sum_{i=1}^{n_0} x_0^i \tag{C.1}$$

$$\mu_2 = \frac{1}{n_2} \left(\sum_{i=1}^{n_0} x_0^i + \sum_{i=1}^{n_1} x_1^i \right) \tag{C.2}$$

Multiplying both sides of Equation (C.1) by n_0 and substituting into Equation (C.2), and doing the same for data set #1, the computation of the updated mean is complete.

$$\mu_2 = \frac{n_0\mu_0 + n_1\mu_1}{n_2} \tag{C.3}$$

C.2 Updated standard deviation

The computation of the standard deviation is a bit more involved, but starts from the definitions, as in the previous section. Here, the population standard deviation is used, but the derivation procedure is analogous for the sample-corrected standard deviation, at which 1 is subtracted from the number of data points (UPTON; COOK, 2014).

$$\sigma_0 = \sqrt{\frac{1}{n_0}\sum_{i=1}^{n_0}(x_0 - \mu_0)^2} \tag{C.4}$$

$$\sigma_2 = \sqrt{\frac{1}{n_2}\left(\sum_{i=1}^{n_0}(x_0 - \mu_2)^2 + \sum_{i=1}^{n_1}(x_1 - \mu_2)^2\right)} \tag{C.5}$$

The next step involves expanding the squares of differences inside the combined standard deviation (Equation (C.5)), after adding and subtracting the standard deviation of the original sets. Computations are shown for index #0 and are analogous for #1.

$$\begin{aligned}(x_0 - \mu_2)^2 &= (x_0 - \mu_0 + \mu_0 - \mu_2)^2 \\ &= (x_0 - \mu_0)^2 + 2(x_0 - \mu_0)(\mu_0 - \mu_2) + (\mu_0 - \mu_2)^2\end{aligned} \tag{C.6}$$

$$\therefore \sum_{i=1}^{n_0}(x_0 - \mu_2)^2 = \sum_{i=1}^{n_0}(x_0 - \mu_0)^2 + 2(x_0 - \mu_0)\sum_{i=1}^{n_0}(\mu_0 - \mu_2) + n_0(\mu_0 - \mu_2)^2 \tag{C.7}$$

Squaring both sides of the definition of σ_0 (Equation (C.4)), an alternative form for the first term of Equation (C.7) is computed as follows:

$$\sigma_0^2 = \frac{1}{n_0}\sum_{i=1}^{n_0}(x_0 - \mu_0)^2 \Rightarrow \sum_{i=1}^{n_0}(x_0 - \mu_0)^2 = n_0\sigma_0^2 \tag{C.8}$$

Substituting the last expression into Equation (C.7) and knowing that its second term equals zero, the sum of the squares of differences is summarized as follows:

$$\sum_{i=1}^{n_0}(x_0 - \mu_2)^2 = n_0\sigma_0^2 + n_0(\mu_0 - \mu_2)^2 \tag{C.9}$$

Substituting Equation (C.9) and its analogous for set #1 into Equation (C.5), a formula for σ_2 is obtained, demanding previous computation of μ_2 (Equation (C.3)).

$$\sigma_2 = \sqrt{\frac{1}{n_2}\left(n_0\sigma_0^2 + n_0(\mu_0 - \mu_2)^2 + n_1\sigma_1^2 + n_1(\mu_1 - \mu_2)^2\right)} \tag{C.10}$$

To not depend on computing μ_2 before σ_2, it is possible to further manipulate the sum of terms that contain μ_2.

$$n_0(\mu_0 - \mu_2)^2 + n_1(\mu_1 - \mu_2)^2 = \tag{C.11}$$

$$= n_0\mu_0^2 - 2n_0\mu_0\mu_2 + n_0\mu_2^2 + n_1\mu_1^2 - 2n_1\mu_1\mu_2 + n_1\mu_2^2 \tag{C.12}$$

$$= n_0\mu_0^2 + n_1\mu_1^2 + (n_0 + n_1)\mu_2^2 - 2(n_0\mu_0 + n_1\mu_1)\mu_2 \tag{C.13}$$

$$= n_0\mu_0^2 + n_1\mu_1^2 + (n_0 + n_1)\frac{(n_0\mu_0 + n_1\mu_1)^2}{(n_0 + n_1)^2} - 2(n_0\mu_0 + n_1\mu_1)\frac{n_0\mu_0 + n_1\mu_1}{n_0 + n_1} \tag{C.14}$$

$$= n_0\mu_0^2 + n_1\mu_1^2 + \frac{(n_0\mu_0 + n_1\mu_1)^2}{n_0 + n_1} - 2\frac{(n_0\mu_0 + n_1\mu_1)^2}{n_0 + n_1} \tag{C.15}$$

$$= n_0\mu_0^2 + n_1\mu_1^2 - \frac{(n_0\mu_0 + n_1\mu_1)^2}{n_0 + n_1} \tag{C.16}$$

$$= \frac{n_0^2\mu_0^2 + n_0n_1\mu_0^2 + n_0n_1\mu_1^2 + n_1^2\mu_1^2 - (n_0^2\mu_0^2 + 2n_0n_1\mu_0\mu_1 + n_1^2\mu_1^2)}{n_0 + n_1} \tag{C.17}$$

$$= \frac{n_0n_1\mu_0^2 - 2n_9n_1\mu_0\mu_1 + n_0n_1\mu_1^2}{n_2} \tag{C.18}$$

$$= \frac{n_0n_1(\mu_0 - \mu_1)^2}{n_2} \tag{C.19}$$

Returning to Equation (C.10), the final form is obtained without dependence on μ_2.

$$\sigma_2 = \sqrt{\frac{1}{n_2}\left(n_0\sigma_0^2 + n_1\sigma_1^2 + \frac{n_0n_1(\mu_0 - \mu_1)^2}{n_2}\right)} \tag{C.20}$$